



National Library
of Canada

Acquisitions and
Bibliographic Services Branch

395 Wellington Street
Ottawa, Ontario
K1A 0N4

Bibliothèque nationale
du Canada

Direction des acquisitions et
des services bibliographiques

395, rue Wellington
Ottawa (Ontario)
K1A 0N4

1980-1981

1980-1981

NOTICE

The quality of this microform is heavily dependent upon the quality of the original thesis submitted for microfilming. Every effort has been made to ensure the highest quality of reproduction possible.

If pages are missing, contact the university which granted the degree.

Some pages may have indistinct print especially if the original pages were typed with a poor typewriter ribbon or if the university sent us an inferior photocopy.

Reproduction in full or in part of this microform is governed by the Canadian Copyright Act, R.S.C. 1970, c. C-30, and subsequent amendments.

AVIS

La qualité de cette microforme dépend grandement de la qualité de la thèse soumise au microfilmage. Nous avons tout fait pour assurer une qualité supérieure de reproduction.

S'il manque des pages, veuillez communiquer avec l'université qui a conféré le grade.

La qualité d'impression de certaines pages peut laisser à désirer, surtout si les pages originales ont été dactylographiées à l'aide d'un ruban usé ou si l'université nous a fait parvenir une photocopie de qualité inférieure.

La reproduction, même partielle, de cette microforme est soumise à la Loi canadienne sur le droit d'auteur, SRC 1970, c. C-30, et ses amendements subséquents.

Canada

**A NUMERICAL STUDY OF
DEFORMATION OF THE IRANIAN PLATEAU**

by
Farhad Sobouti

**A thesis submitted to the Faculty of Graduate Studies and Research in partial
fulfilment of the requirements for the degree of Master of Science in the
Department of Earth and Planetary Sciences**

**Geophysics Laboratory
Department of Earth and Planetary Sciences
McGill University
Montreal, Quebec
Canada
March 1994**

© Farhad Sobouti



National Library
of Canada

Bibliothèque nationale
du Canada

Acquisitions and
Bibliographic Services Branch

Direction des acquisitions et
des services bibliographiques

395 Wellington Street
Ottawa, Ontario
K1A 0N4

395, rue Wellington
Ottawa (Ontario)
K1A 0N4

Your file / Votre référence

Our file / Notre référence

The author has granted an irrevocable non-exclusive licence allowing the National Library of Canada to reproduce, loan, distribute or sell copies of his/her thesis by any means and in any form or format, making this thesis available to interested persons.

L'auteur a accordé une licence irrévocable et non exclusive permettant à la Bibliothèque nationale du Canada de reproduire, prêter, distribuer ou vendre des copies de sa thèse de quelque manière et sous quelque forme que ce soit pour mettre des exemplaires de cette thèse à la disposition des personnes intéressées.

The author retains ownership of the copyright in his/her thesis. Neither the thesis nor substantial extracts from it may be printed or otherwise reproduced without his/her permission.

L'auteur conserve la propriété du droit d'auteur qui protège sa thèse. Ni la thèse ni des extraits substantiels de celle-ci ne doivent être imprimés ou autrement reproduits sans son autorisation.

ISBN 0-315-94527-3

Canada

Contents

Contents	i
Abstract	iv
Résumé	v
Acknowledgment	vi
List of figures	vii
List of tables	ix
Introduction	1
Chapter 1 Geology and tectonics of Iran	4
1.1 A brief history of geological and tectonic evolution of Iran	4
1.2 Active tectonics and recent seismicity	7
The Zagros mountains	10
Northwestern Iran and the Caucasus	12
The southern Caspian block	13
The Alborz and Kopeh Dagh mountains	14
Central and eastern Iran	15
The Makran region	16
Chapter 2 Modelling the continental deformation	17
2.1 A brief introduction to the continuum approach	17
2.2 The thin viscous sheet model	18
2.2.1 Assumptions	19

2.2.2	Mathematical formulation	21
2.2.3	The results of the model in central Asia	26
Chapter 3	Numerical modelling of deformation in the Iranian plateau	29
3.1	Initial assumptions	29
3.1.1	Geometry of the models	30
3.1.2	Initial and boundary conditions	32
3.1.3	Physical parameters	33
3.2	Results of numerical experiments	34
3.2.1	Homogeneous models	34
3.2.1.1	Models with $Ar = 0$	34
	Velocity field	35
	Strain rate fields	39
	Crustal thickness	44
3.2.1.2	Models with $Ar > 0$	46
	Velocity field	47
	Strain rate fields	47
	Crustal thickness	50
	Stress fields and style of faulting	53
3.3.2	Heterogeneous models	56
	Velocity field	58
	Strain rate fields and crustal thickness	58
	Stress fields and style of faulting	64
Chapter 4	Discussion and conclusions	71
4.1	Comparison of results with tectonic observations in Iran	71

4.1.1	Crustal thickness and topography	72
4.1.2	Strain rates and vertical deformation	78
4.1.3	Tectonic styles and fault plane solutions	82
4.2	Conclusions	87
4.3	Future work	89
Appendix Numerical solutions of the equations		90
A.1	The finite element method, a general background	90
A.1.1	Finite element formulation of the force balance equation	92
A.1.2	Finite element formulation of the continuity equation	94
A.2	Computer programming techniques	94
References		138

Abstract

The deformation of the Iranian plateau subject to the convergence of the Arabian shield and Eurasian plate, is studied by the "thin viscous sheet" numerical model. The lithosphere is approximated by a thin layer having a uniform initial thickness, and the flow of material is assumed to be governed by a power law rheology. The solutions are calculated for velocity fields, crustal thickness distributions, stress and strain rate fields, and topography variations. The effects of the physical parameters (rheology, density etc) are investigated through two non-dimensional parameters: n , the power law exponent in the constitutive relation between stress and strain rate, and Argand number Ar , which is a measure of the relative importance of the buoyancy force to the viscous force. The lack of deformation in central Iran and the southern Caspian block, is considered, by including lateral heterogeneities in the rheology of the lithosphere. The results show that heterogeneous models with non-Newtonian materials for n greater than 3 and $1 < Ar < 10$ can best approximate tectonic features of Iran. The models are successful in providing reasonable agreement between the estimates of crustal thickness and strain rates, obtained from seismic observations, and those predicted from the theory. The topography pattern and the style of faulting in different parts of the plateau, are explained through the effect of boundary conditions and lateral heterogeneities.

Résumé

Les déformations subies par le plateau iranien, soumis à la convergence des plaques arabique et eurasienne, sont étudiées à l'aide d'un modèle numérique de type "plaque fine visqueuse". La lithosphère est modélisée par une plaque fine dont l'épaisseur est initialement uniforme et la rhéologie gouvernée par une loi de puissance. Le modèle permet de déterminer les champs de vitesse, de contrainte et de taux de déformation, ainsi que la distribution des épaisseurs crustales et les variations de topographie. L'effet des paramètres physiques (rhéologie, densité, etc...) est étudié par l'intermédiaire de deux paramètres sans dimension: n , l'exposant de la loi de puissance constitutive reliant contraintes et taux de déformation, et Ar , le nombre d'Argand, qui mesure l'importance relative des forces de flottabilité par rapport aux forces visqueuses. L'absence de déformation dans les blocs d'Iran central et Sud-Caspien est prise en compte par l'adjonction d'hétérogénéités latérales dans la rhéologie de la lithosphère. Les modèles hétérogènes à rhéologie non-newtonienne pour n supérieur à 3 et Ar compris entre 1 et 10 prédisent le mieux les caractères tectoniques de l'Iran. Ces modèles conduisent à un accord raisonnable avec les épaisseurs crustales et les taux de déformation dérivés des observations sismiques. La topographie et le type de failles observés dans les différentes parties du plateau sont expliqués par l'effet des conditions aux limites et d'hétérogénéités latérales.

Acknowledgements

I wish to thank my advisor Prof. J. Arkani-Hamed for offering the subject of this thesis to me, and his continued guidance, encouragement and valuable suggestions and criticism during the course of this study.

I also wish to thank other members of the Geophysics Laboratory, Prof. O. Jensen and Prof. D. Crossley, and my friends Dr. H. Vali, Dr. J. Dymant, Reza, Chengchun and Hui, for their contribution towards a useful and pleasant stay at McGill.

List of figures

Figure

1.1	A map of tectonic regions in Iran	5
1.2	A map of active faults in Iran	8
2.1	A sketch of the vertical structure of the lithosphere	23
2.2	Plots of velocity and crustal thickness for models in central Asia	28
3.1	The geometrical configuration of the finite element grid	31
3.2	Velocity fields for homogeneous models with $Ar = 0$	36
3.3	Velocity profiles for homogeneous models with $Ar = 0$	38
3.4	Time variations of strain rates for homogeneous models with $Ar = 0$	40
3.5	Vertical strain rates for homogeneous models with $Ar = 0$	42
3.6	Shear strain rates for homogeneous models with $Ar = 0$	43
3.7	Crustal thickness variations for homogeneous models with $Ar = 0$	45
3.8	Velocity fields for homogeneous models with $Ar > 0$	48
3.9	Time variations of vertical strain rates for homogeneous models	49
3.10	Shear strain rates for homogeneous models with $Ar > 0$	51
3.11	Crustal thickness distributions for homogeneous models with $Ar > 0$	52
3.12	Principal deviatoric stresses for homogeneous models with $Ar > 0$	54
3.13	Maximum shear stresses for homogeneous models with $Ar > 0$	57

3.14	Velocity fields for heterogeneous models	59
3.15	Vertical strain rates for heterogeneous models	60
3.16	Crustal thickness distributions for heterogeneous models	61
3.17	Crustal thickness in a model with transitional rheology	63
3.18	Profiles of crustal thickness for heterogeneous models	65
3.19	Time variations of maximum shear strain rate in heterogeneous models	66
3.20	Principal horizontal deviatoric stresses in heterogeneous models	68
3.21	Time variations of maximum shear stress in heterogeneous model	70
4.1	surface elevation calculated from the models	76
4.2	Three dimensional image of a topography distribution	77
4.3	Horizontal components of strain rate in the models	81
4.4	Uplift rate and crustal thickening rate in the models	83
4.5	Comparison of topography gradients and orientations of the P-axes	85
A.1	A sketch of a triangular element	95

List of tables

Table

1.1	Rotation poles and rates of relative motions in the Mediterranean	9
4.1	Crustal thicknesses in the Zagros	73
4.2	Strain rates calculated from the moment rate tensors	79

Introduction

This study is concerned with the deformation of continental lithosphere in the Iranian plateau, and makes use of the equations governing the flow of a continuous medium, to investigate the characteristics of such deformation. Plate tectonics describes the structure of the lithosphere as a number of rigid plates in relative motion, interacting only at their edges. With this description, one could predict that all of the deformation must be happening on narrow bands on the common boundaries of the plates. In fact this theory does provide a satisfactory portrait of the processes involved in the deformation of oceanic lithosphere. Almost all of the deformation in the mid-oceanic ridges, takes place on zones of 10 to 20 km width to the sides of the ridge. However deformation of the continents shows a dramatic difference from that predicted by plate tectonics. The collision of continental plates leads to an enormous crustal deformation, distributed over horizontal distances that far exceed the plate thickness. It produces considerable amounts of crustal thickening (e.g. the Tibetan plateau with 70-80 km thickness), and develops large scale positive gravity anomalies and seismic zones of diffuse nature. The distribution of topography and seismicity in two of the largest continental collision zones, India and central Asia, and the Afro-Arabian plate and Eurasia in the Mediterranean region, clearly shows that seismicity and crustal thickening stretch up to 2000 km inland central Asia, and a belt of active deformation with a width of 1000 km develops in western Asia (England & Jackson 1989).

The Iranian plateau as a part of this broad zone of continental deformation, is a highly elevated region (with an average elevation of about 1.5 km), located in the convergence zone between the Arabian continental mass and the Eurasian

plate. It is characterized by intense compressional movements, crustal shortening and active faulting, and is considered as one of the most tectonically and seismically active continental collision zones in the world (Berberian 1976a). It is noticeable that like many other collision zones, most of the deformation in the plateau, is taken up by a large number of reverse faults, rather than a few number of larger faults. These simultaneously active faults are distributed over the entire belt, indicating that the deformation occurs more or less uniformly throughout the region.

In order to explain the nature of the deformation of the continents, several approaches have been made. One way which attempts to keep the discussion in the framework of plate tectonics, considers the deformation as the result of interaction of a number of small rigid plates or "micro-continents". Studies of seismicity and deformation of continental areas show that, although deformation is scattered over some broad zones, this distribution is not homogeneous. There are regions such as the Aegean sea, central Turkey, central Iran and the Tarim basin, which have less seismic activity and lower and flatter topography than their neighbouring regions. One may presume these relatively stable blocks as the rigid microplates, which their function is to take up the strain as they move relative to each other in response to the forces arising at their edges. However this approach has many disadvantages. The boundaries of these blocks are difficult to determine, and as England & Jackson (1989) point out in the case of the Mediterranean and the Middle East, the relative motions of them bear no obvious relation to those of the major plates bounding them, i.e. the Eurasian and Afro-Arabian plates. Furthermore, it is impossible to determine the style of the deformation from relative motions of the microplates (England & Jackson 1989). A good example is the deformation in Iran. The convergence between Arabia and central Iran is accommodated mainly by thrust faulting along the Zagros with northeastward direction. While the convergence between central Iran and Eurasia in the same

direction, is controlled by a combination of thrusting and strike-slip motion. Although the direction of relative velocities predicted from plate tectonics are the same in the Zagros and northeastern Iran, they do not uniquely determine the strain within the deforming zones. Another objection to this approach is that, the aseismic regions may not always remain strong during the period of deformation (England & Jackson 1989). For instance, the southern Aegean sea and the Tibetan plateau in the present day look largely aseismic. Nonetheless in the past few million years, both have experienced a significant amount of deformation. If a region is relatively strong now, it does not necessarily mean it was initially strong, or it will remain strong. Many factors such as temperature variations during the deformation, can affect the strength of a part of the lithosphere.

The observations mentioned above, have pointed to a new way of viewing the deformation in the continental regions. The new approaches assume the strain rate and not the stress, as the basic constituent controlling the motion of the material, and treat the deformation in terms of mechanics of a continuous medium, subject to forces and velocities applied at the boundaries, as well as forces arising within the interior. The investigations carried out in the past 10 to 15 years have demonstrated that, the continuum approaches are capable of providing a satisfactory description for the diffuse nature of continental deformation, and producing acceptable quantitative estimates of the stresses and rates of deformation, involved in the collisional processes.

It is in pursuit of the above discussion that this study has been conducted; to investigate in the context of continuum mechanics, the effects of the forces arising from the convergence of Arabia on the tectonics of Iran, and to assess the role of internal processes such as the development of buoyancy forces and the presence of lateral heterogeneities on the evolution of the deformation within the Iranian lithosphere.

Chapter 1

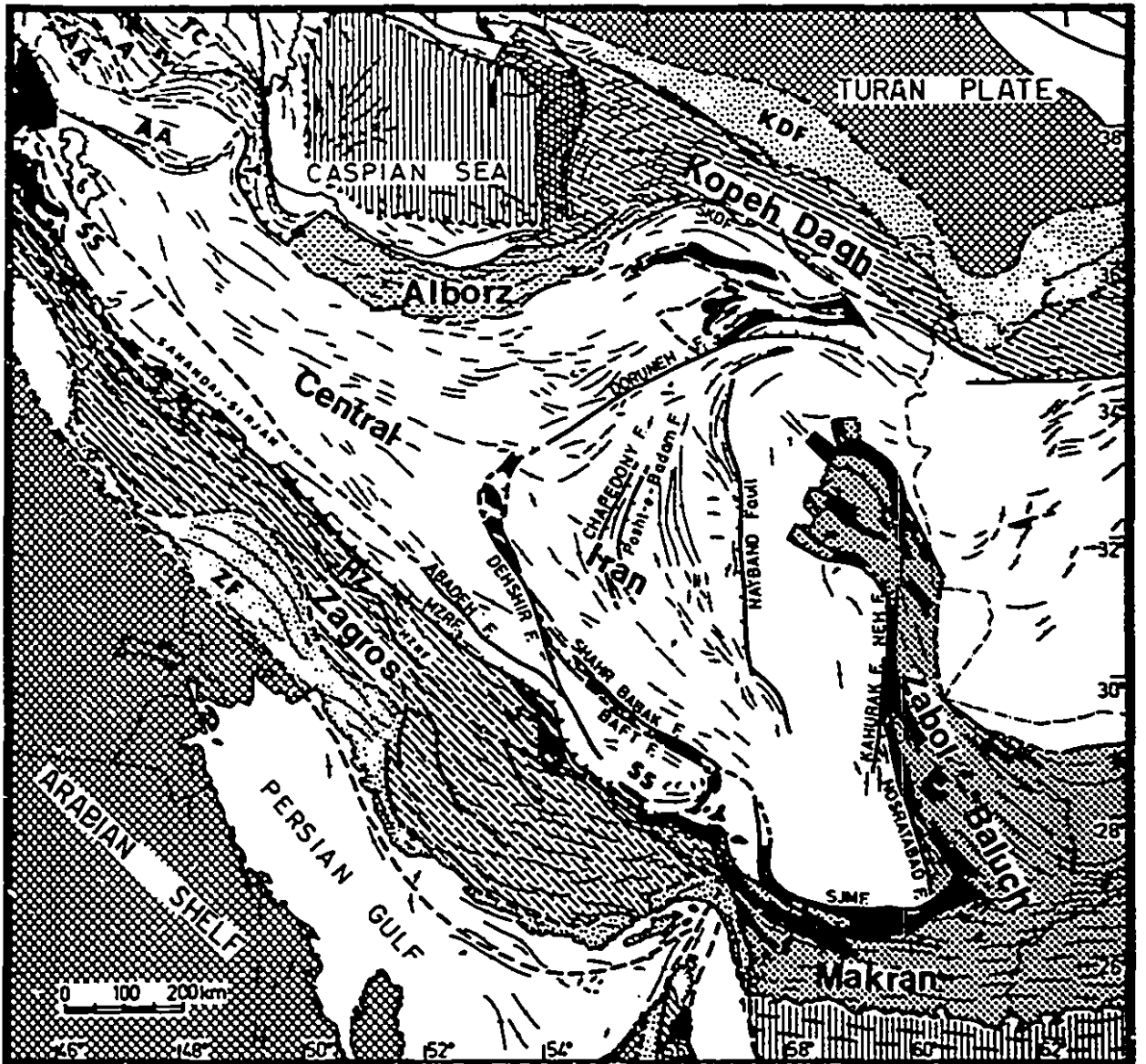
Geology and tectonics of Iran

1.1 A brief history of geological and tectonic evolution of Iran

The Iranian plateau is considered as a part of the Alpine-Himalayan orogenic belt (Figure 1.1). Despite the high rate of recent tectonic activity, the plateau has relatively simple history of deformation, and geological features are mostly young. Geological evidence (Takin 1972, Stöcklin 1974, Sengör & Kidd 1979, Berberian & King 1981) suggest that during the Paleozoic era, southern and central parts of Iran along with some other regions in the Middle East, formed a part of the northern edge of the Afro-Arabian continent, bordered by the Paleo-Tethys ocean in the north. While northern Iran and the Caucasus were to the north of the Paleo-Tethys, as a part of Eurasia. The southern Caspian oceanic block might be a relict of this ocean.

During the Hercynian orogeny in the late Paleozoic-early Mesozoic, when the oceanic crust between Gondwana and Eurasia was being consumed, central Iran and the neighbouring regions travelled across the ocean as continental fragments and connected themselves to the southern margins of Eurasia, leaving the Zagros region behind to become the northern shelf of the Arabian plate. As a result, the tectonic style of Iran during this period was divided into two regions; in the north the subduction of the Paleo-Tethys underneath Eurasia was taking place, although the continental fragments might had been separated from Eurasia until the middle Cenozoic (Sengör & Kidd

Figure 1.1 A map showing the major tectonic units of Iran and adjacent regions discussed in the text (after Berberian 1981).



1979), and in the south the structural features were dominated by extensional movements and opening of a rift along the present day " main Zagros thrust line ". Later in the Triassic, this rifting developed to what is frequently referred to as, the " Neo-Tethys ocean ".

Later probably in the middle Triassic, the subduction shifted from north to south of central Iran and continued during the early Alpine orogeny to the end of the Mesozoic. The result was underthrusting of the Neo-Tethys ocean beneath central Iran (possibly along the main Zagros thrust), formation of a metamorphic belt (the Sanandaj-Sirjan belt) and exposition of an ophiolitic belt in the southern margin of central Iran, and numerous phases of extension which ultimately caused the thinning of the crust in central Iran. During the same period when central Iran was subject to unstable sedimentary environments, the Arabian continental shelf was the site of progressive subsidence, and a uniform thick, mainly carbonaceous marine sedimentation (Berberian & King 1981).

The northward drift of the Afro-Arabian plate eventually led to the closure of the Neo-Tethys ocean at the end of the Cretaceous (65 m.y. ago), and a new compressional environment began to dominate the whole region. The onset of the late Alpine orogeny was in the late Miocene. It was accompanied by the continental collision of Arabia and Asia and the main Zagros thrust is believed to be located on the boundary of the two plates (Stöcklin 1968, Falcon 1974). Since that time, Iran has undergone a progressive phase of crustal thickening and shortening by folding and reverse faulting. The deformation reached its peak during the late Pliocene-early Quaternary, when the mountain ranges gained a considerable height. In fact the Cenozoic features comprise most of the geological outcrops in Iran. The convergence between Arabia and Asia is still taking place at a rate of 4-5 cm y^{-1} (LePichon 1968, McKenzie 1972), and crustal thickening currently has an estimated value of 1 mm y^{-1}

(Snyder & Barazangi 1986). The only place in Iran where ocean-continent convergence is still happening is the Makran coast in the southeast (Farhoudi & Karig 1977, Kadinsky-Cade & Barazangi 1982). It is separated in the west from the Zagros collision zone by a northward trending structural lineament called "the Oman line". This subduction zone is associated with a post-cretaceous accretionary prism with an east-west trend, and the oceanic slab of the Oman sea is subducting northwards with a rate of 5 cm y^{-1} (Farhoudi & Karig 1977, Berberian 1981).

1.2 Active tectonics and recent seismicity

The convergence between the rigid blocks of Arabia and Asia, is the most prominent factor in the active deformation of Iran. The Iranian plateau is a relatively weak zone, entrapped between the two blocks. The fault plane solutions of earthquakes (Figure 1.2) indicate that most of the seismic deformation is taking place by reverse faulting along the mountain ranges (McKenzie 1972, Berberian 1981). The dominance of reverse faulting indicates that in Iran, unlike many other continental regions such as central Asia and western United States, sideways motion away from the convergence zone is almost impossible due to the presence of rigid boundaries on the western and eastern sides of the deforming zone, and uplifting and thickening is the major style of deformation (Berberian 1981). A less amount of strike-slip motion allows minor sideways movement of material along the strike of the Zagros in northwestern Iran and eastern Turkey, and some structural rotations in eastern Iran (Jackson & McKenzie 1984).

Studies of recent as well as historical seismicity in Iran and in the Middle East (Nowroozi 1976, Berberian 1981, Ambraseys & Melville 1982, Jackson & McKenzie 1984), show that seismic activity is not limited to some small number of active faults

Figure 1.2 Map of active faults and selected fault plane solutions in Iran and neighbouring regions (after Berberian 1981). The abbreviations, Do, Db and Ku refer to Doruneh, Dasht-e-Bayaz and Kuh-Banan faults in eastern Iran, respectively.

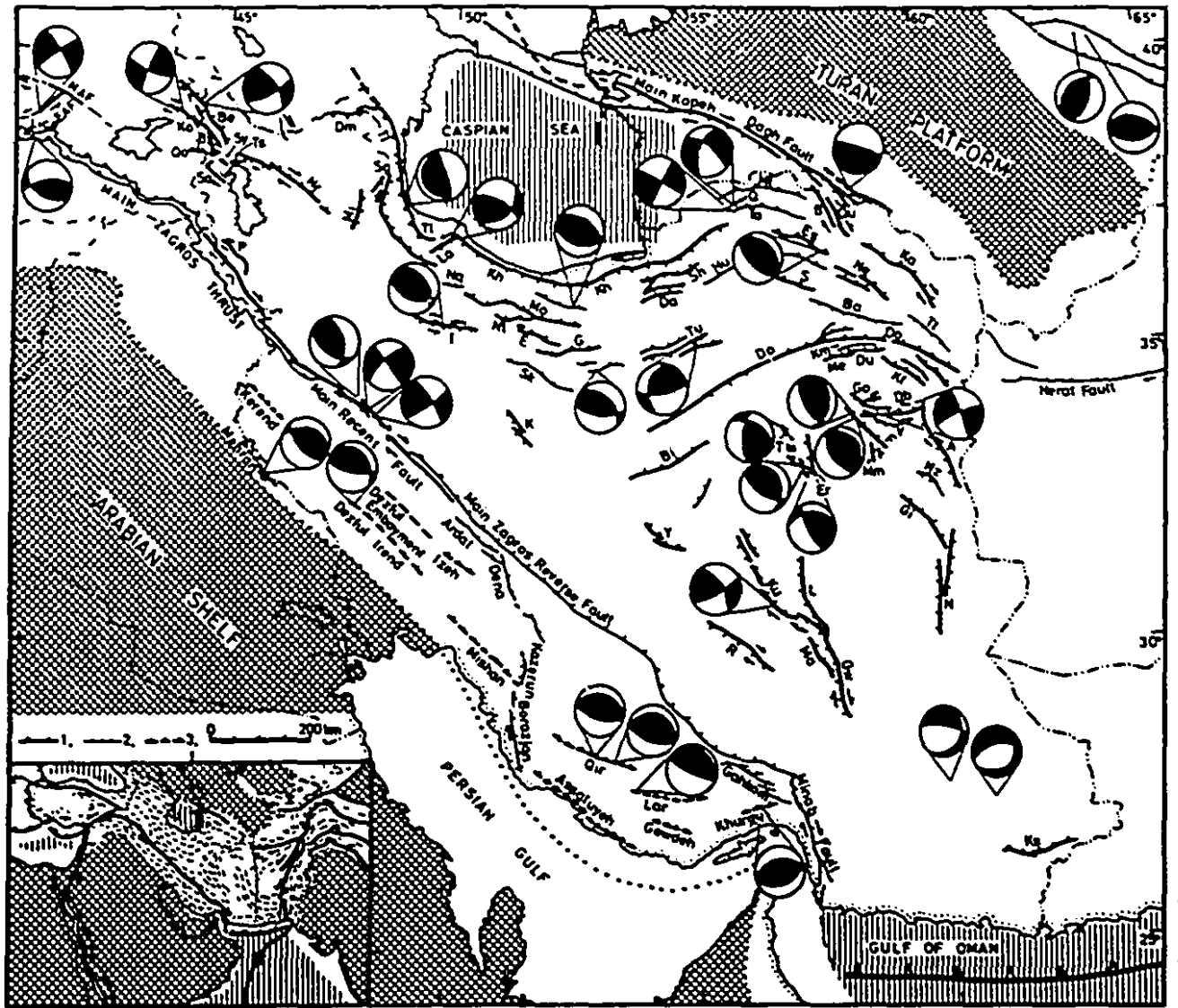


Table 1.1 Rotation poles and the rates for the relative motion between major aseismic blocks (Jackson & McKenzie 1988).

	Latitude	Longitude	Rate*/10 ⁷ yr	Source
Eurasia-Turkey	14.6	34.0	6.43	Jackson & McKenzie (1984)
Eurasia-Africa	29.2	-23.5	1.42	Chase (1978)
Eurasia-Arabia	34.9	7.2	4.93	Chase (1978)
Africa-Turkey	9.3	44.7	5.73	Jackson & McKenzie (1984)
Arabia-Turkey	-20.6	68.9	3.40	Jackson & McKenzie (1984)
Iran-Eurasia	27.5	65.8	5.60	Jackson & McKenzie (1984)
Arabia-Iran	34.5	39.8	9.55	Jackson & McKenzie (1984)
Eurasia-Adriatic	46.0	10.2	unknown	Anderson & Jackson (1987)
Aegean-Africa	40.0	18.0	-23.10	Le Pichon & Angelier (1979)

or narrow bands of few kilometres in width on the boundaries of rigid plates, but rather is spread out over the whole region. Nevertheless this distribution is not quite homogeneous. A closer look at the seismicity maps, reveals that the earthquakes mostly occur within the belts of 100-400 km wide such as, eastern Turkey, the Caucasus, Zagros, Alborz, Kopet Dagh and eastern Iranian mountains, which in turn surround less deforming and less seismically active areas of central Turkey, central Iran, and the southern Caspian block. The relatively high rigidity of these blocks allows one to describe their motion by rotations about poles. Table 1.1 (Jackson & McKenzie 1988) gives the rotation poles and rates of relative motion for the major aseismic blocks in the Mediterranean and the Middle East.

Based on seismicity, topography and deformation patterns, Iran can be divided into several tectonic elements. In the following, seismotectonics and active deformation of each of these elements is briefly discussed:

1.2.1 The Zagros mountains

The Zagros range is located on the convergence zone of the Arabian shield and central Iran. It has a strike of roughly N45°W and is extended from eastern Turkey in the northwest to the strait of Hormoz in the south of Iran. The estimated total thickness of the sedimentary column in the Zagros is 6-12 km, including a thick layer (about 1 km) of infra-Cambrian evaporitic deposits at the bottom (Berberian & King 1981). The Zagros main thrust, a northeastward dipping plane, marks the northern margin of the Arabian continental shelf.

The Zagros mountains is the most active seismic zone of Iran, and much of the convergence between Arabia and Eurasia is taken up in this part of country. Seismicity maps of Iran (e.g. Berberian 1976b, Ni & Barazangi 1986) show that earthquake

epicentres in the Zagros are distributed over a 200-300 km wide zone along the belt. Seismicity is immediately cut off in the northeast of the main thrust. Also there is a considerable quiescence of earthquake activity in the east of the Oman line, which separates the Zagros from the Makran region (Jackson & McKenzie 1984). In general, seismicity increases from northwest to southeast. Most of the earthquake mechanisms in the central and southeastern Zagros, are indicative of shortening of the crust perpendicular to the strike, along many high angle (30° - 60°) reverse basement faults (Berberian 1981, Jackson & Fitch 1981), except for the region near the strait of Hormoz where the penetration of the Musandam peninsular, a southern promontory of the Arabian shield, in to Iran, causes a movement of material along the strike of the mountain ranges (Jackson & McKenzie 1984). In the northwestern Zagros, fault plane solutions show a right lateral strike-slip motion along an active fault zone which follows the trace of the main Zagros thrust (Jackson & McKenzie 1984). The estimated value of slip rates in this part of the Zagros is about 1.5 cm y^{-1} . The slip rates increase southeastward and reach a maximum value of about 3 cm y^{-1} in the southern end (Jackson & McKenzie 1984).

All the work done on the seismotectonics of the Zagros (e.g. Nowroozi 1976, Jackson & Fitch 1981, Jackson & McKenzie 1984, Ni & Barazangi 1986) suggest that the depth of the seismogenic layer is limited to 20 km and majority of the earthquakes occur below the sedimentary cover. There is no substantial evidence for subcrustal seismicity in the Zagros. The relative steepness of the fault planes and their similarity to normal faults in regions of crustal extension, has led some of the workers (e.g. Jackson et al. 1981) to argue that a considerable portion of the seismic activity in the Zagros is taking place on some reactivated reverse faults, which during the past crustal stretching phases in the Mesozoic, were acting as normal faults.

Studies of seismic strain rates on the historical and recent earthquakes

(Ambraseys and Melville 1982, Shoja-Taheri & Niazi 1981, Jackson & McKenzie 1988, Ekström & England 1989) show that the slip vectors calculated from earthquake data are less than 10% of those predicted by plate tectonic theory. In other words, seismicity in the Zagros is responsible for as little as 10% of deformation. The rest is being accomplished by creep processes. This evidence along with the lack of surface faulting in the Zagros (Berberian 1981) and presence of a salt layer at the top of the basement suggest that, this plastic layer is probably acting as a detachment surface, separating the deformation of the basement from that of the overlying sediment. Therefore the tectonic stresses produced in the basement do not efficiently transmit to the upper layers, and while the basement undergoes brittle deformation, the sedimentary column deforms by aseismic folding.

1.2.2 Northwestern Iran and the Caucasus

In the Caucasus, major geological structures have a northwest-southeast trend. The region is bounded by the oceanic crusts of the Black sea in the west and the southern Caspian sea in the east. Seismicity in the Caucasus most of the time, follows the regional trends. The majority of the earthquakes have thrust mechanism with north or slightly northeastward dipping nodal planes. Some lateral motions along the strike of the mountains at both ends of the region as inferred from fault plane solutions, suggest that the Caucasus might be overriding the Black sea and southern Caspian oceanic slabs (Jackson & McKenzie 1984). The seismic zone of the Caucasus continues to southeast across the Caspian sea into the Kopch Dagh mountains.

In northwestern Iran, most of the available focal mechanisms indicate right lateral strike-slip motion, with some normal faulting. Jackson and McKenzie (1984) conclude that, this kind of deformation is a result of the eastward expulsion of eastern

Turkey away from the collision zone in central Turkey, which extends into northwestern Iran. Therefore northwestern Iran has a eastward motion relative to Eurasia. A part of this region shows a lack of seismicity both in historical and recent record. Some authors (e.g. Jackson & McKenzie 1984) regard this area as one of the aseismic regions in Iran.

Much of the well recorded earthquakes in northwestern Iran and the Caucasus, have focal depths shallower than 50 km, and no reliable evidence supports the existence of subcrustal seismicity. Also calculations of seismic strain rate tensors (Jackson & McKenzie 1988) show that like the Zagros, most of the deformation in the Caucasus is taking place aseismically.

1.2.3 The southern Caspian block

Deep seismic studies (Berberian 1983) suggest that in the southern Caspian sea a relatively thick (15-25 km) column of sedimentary material directly overlies a basaltic basement of 15-20 km thick. The evidence for lack of granitic layer is also supported by the efficient propagation of s_p and poor propagation of L_g waves across the basin (Kadinsky-Cade et al. 1981). The southern Caspian is a relatively stable block with feeble seismicity and minor deformation, surrounded by active fold belts and reverse basement faults. It is currently underthrusting towards south beneath the northern ranges of Iran. It is believed (e.g. Berberian 1983) that, it might be a piece of an old oceanic crust, perhaps as old as late Paleozoic, and has survived the convergence of the Afro-Arabian plate towards Eurasia. Based on fault plane solutions in the Caucasus and the slip vectors in the Alborz and Kopeh Dagh, Jackson & McKenzie (1984) have calculated a northward motion of the southern Caspian relative to Eurasia.

1.2.4 The Alborz and Koppeh Dagh mountains

The Alborz and Koppeh Dagh mark the site of the crustal compression of central Iran against Eurasia. Seismicity in these regions is not as intense as it is in the Zagros. Nonetheless a great amount of shortening and thickening is currently taking place in these areas. The Alborz mountains is an arcuate range, bordered by the southern coast of the Caspian sea. Deformation in the Alborz is characterized by series of thrust faulting. In the northern part of the range, faults are dipping southward, possibly indicative of underthrusting of the southern Caspian block. In the southern sections the reverse faults dip northward, as a result of compression against the northern boundaries of Iran. In the east of the Alborz, fault plane solutions indicate some left lateral strike-slip mechanism (Jackson & McKenzie 1984). Although surface faulting in the Alborz is more visible than it is in the Zagros, fault planes are still difficult to be determined.

The structures in the Koppeh Dagh have a northwest-southeast trend and are bordered from the stable block of Turkmenistan in the north, by a fault zone called "the main fault zone" (Tchalenko 1975). Seismicity is diminished immediately to the northeast of this fault zone. Most of the fault plane solutions indicate thrust faulting with left lateral slip in the west, and right lateral slip in the east. All this along with the topographic variations, suggest that northeastern Iran is involved in a considerable crustal shortening and thickening in the northeast direction.

The predicted magnitude of the slip rates from poles of rotations in northern Iran is about 1-1.5 cm y^{-1} . Comparison of this velocity with those calculated from seismic moment release rates (Jackson & McKenzie 1988, Ekström & England 1989) implies that most of the deformation in the Alborz and Koppeh Dagh, is occurring seismically.

1.2.5 Central and eastern Iran

Seismicity in central Iran is sporadic and discontinuous. Historical records (Ambraseys & Melville 1982) also show a relative quiescence of earthquake activity in this part of country. Most of the epicentres are located along the mountain bordering reverse faults (Berberian 1981). The major earthquakes in the northern part of central Iran are involved in thrust faulting and left lateral strike-slip with a northeastward slip vector (Jackson & McKenzie 1984). These earthquakes are associated with several major left lateral strike-slip faults such as Doruneh and Dasht-e-Bayaz faults (see Figure 1.2), which run from east to west. To the south of these faults, is another system of faults striking north-south. These faults are subordinate to the first set and do not intersect them. The north-south trending faults extend to the Makran region in the southeast and dominate the morphology of eastern Iran. They mark the boundaries of the Lut block, a relatively aseismic region in eastern Iran, sometimes considered as a small micro-continent in the literature (e.g. Nowroozi 1976, Arkani-Hamed & Strangway 1986). Some of the north-south trending faults such as Kuh-Banan fault (see Figure 1.2), are active and have historical record of activity (Ambraseys & Melville 1982). Most of these faults have a dominant right lateral sense of motion with some thrust faulting towards east.

Seismicity decreases dramatically in the east of Iran-Afghanistan border (Shoja-Taheri & Niazi 1981) and the structures in eastern Iran are directed towards the south as Iran is being compressed against the western Afghanistan stable block.

The combination of a dominant east-west left lateral faulting with a subordinate system of north-south right lateral faults in northeast and eastern Iran, and thrust faulting with northwesterly strike in northeastern Iran, has led Jackson & McKenzie (1984) to propose that, the eastern parts of Iran are experiencing some structural

rotations as Iran is being compressed at its northern and eastern boundaries. They suggest that the rotation results in a lateral movement of material away from the compression zone towards south to the Makran region on the strike-slip faults. The possibility of structural rotations in eastern Iran is also supported by paleomagnetic data (Conrad et al. 1981). These data indicate an anticlockwise rotation of 90° since the Miocene in the southern Lut block.

1.2.6 The Makran region

In contrast to the Zagros, the Makran region shows a feeble and scattered seismicity. The focal depths of earthquakes increase from very shallow (< 10 km) at the coast of the Oman sea, to intermediate depths (80 km) inland (Berberian 1981). There are only two earthquakes located at depths greater than 100 km. Nevertheless this few evidence of intermediate seismicity has not prevented some workers (e.g. Farhoudi & Karig 1977) from proposing a subduction model for the Makran. The sporadic nature of the seismicity has been accounted for the very shallow angle (about 1° as proposed by Farhoudi & Karig 1977) of the subducting slab. Fault plane solutions suggest two different types of earthquakes (Berberian 1981). The first group is shallow earthquakes associated with east-west trending and northward dipping reverse faults, which characterize the deformation of the sedimentary cover. The second group is intermediate earthquakes accompanied with normal faulting produced during the deformation of the subducting oceanic crust. The predicted slip vectors in the Makran are directed N10°-15°E, with a magnitude of 4 cm y^{-1} (Jackson & McKenzie 1984).

Chapter 2

Modelling the continental deformation

2.1 A brief introduction to the continuum approach

One of the first attempts in continuum medium modelling of the deformation, taken by those working on the Himalayan collision zone (e.g. Tapponnier & Molnar 1976), was to compare the patterns of strain with the slip line fields produced during the indentation of a rigid-plastic thin plate, by a rigid indenter. Specifically, central Asia was taken as the thin plate with a highly nonlinear viscoplastic rheology, and the Indian subcontinent was assumed as the indenter. One of the main arguments of this model was that, the major strike-slip fault zones in the central Asian collision site, correspond to the slip lines developed in the deforming plate. This model assumed a plane horizontal strain condition and the deformation was controlled by the regional stress fields applied by the indenter.

Although this approach can explain the large scale deformation and is relatively successful in matching the calculated slip lines with the orientation of major faults, it has many limitations, as England & McKenzie (1982) and Tapponnier & Molnar themselves have mentioned. First, in the regions of excessive crustal thinning or thickening, the condition of plane horizontal strain fails, since considerable amount of deformation takes place in the vertical direction. Second, forces due to the gravitational potential differences between columns of lithospheric material, have no role in this

model. Third, the calculated slip lines are appropriate only for the beginning stages of indentation. They change direction as the deformation proceeds. Furthermore this model predicts a uniform stress field, while the nonuniform distribution of the fault zones in central Asia, is indicative of existence of a nonuniform stress field.

New approaches (e.g. Bird 1978, Bird & Piper 1980, England & McKenzie 1982, England & Houseman 1986, Vilotte et al. 1982, 1984, 1986) emphasize on the importance of the kinematic constraints, in the deformation of continents, and reason that the deformation is controlled by strain rate and not stress. These models take the advantage of numerical techniques, to include the effects of crustal thickness variations, buoyancy forces, different rheologies and more realistic boundary conditions. These techniques have been significantly successful in providing reasonable descriptions for deformational processes in the continents, both quantitatively and qualitatively. The thin viscous sheet model essentially developed by Bird & Piper (1980), England & McKenzie (1982), and Vilotte et al. (1982, 1984, 1986), is one of the most successful of these. This model has been able to carry out quantitative measurements on stress and strain rate fields in the Himalayan collision zone, with results which are fairly in agreement with the observations. In the current study, this model has been taken as a basis to investigate the deformation history in the Iranian plateau. In the following, the mechanical formulation of the thin viscous sheet model is presented:

2.2 The thin viscous sheet model

The fundamental idea of the thin viscous sheet model is that the deformation of the continents, is the response of a viscous medium to the forces applied at its boundaries, and to the buoyancy forces arising within the medium from elevation contrasts. A quasi-three-dimensional plane stress condition is adopted and buoyancy

forces are taken into account by allowing strain in vertical direction. The buoyancy forces are balanced against the ambient stress field deforming the viscous medium. The numerical approach permits the calculation of the time dependent deformation, stress and strain rate fields and the crustal thickness development in time. By applying different stress-strain rate constitutive laws and different viscosities, the effect of rheology on the deformation can be studied. Also the relation between the calculated stress, strain and strain rate at each stage of deformation, with the styles of the observed discontinuous deformation can be investigated. A detailed description of the thin viscous sheet model is given by England & McKenzie (1982, 1983). In the following, a summary of the assumptions and formulation of the model is presented:

2.2.1 Assumptions

1. The lithosphere is approximated by a thin sheet, with a horizontal expansion of at least ten times the thickness of the plate, overlying an inviscid medium. This assumption is based on the fact that the lithosphere is underlain by an asthenosphere much weaker than itself. As a result, the shear stresses on the top and bottom of the sheet are assumed to be negligible.

2. If the gradient of crustal thickness, i.e. the topography gradient is small, the vertical variation of horizontal velocity within the thickness of the lithosphere will be insignificant.

3. The deformation of the lithosphere is assumed to be governed by rheological properties of its strongest portion, presumably the upper mantle or the lower crust. Therefore the discontinuous behaviour of deformation of the upper crust is ignored. The reasons for neglecting the role of faulting in the deformation are a) the nature of the continuum approach does not allow us to take into account the brittle deformation

of the lithosphere and b) although faults are outstanding features of the surface of the earth, fracturing is restricted to the upper 20 km of the crust. We assume here that faulting in the upper crust passively follows the ductile deformation in the deeper parts.

4. A few reliable measurements on the rheological properties of the lithospheric material are available (Goetze 1978). Nevertheless this little information suggests that the upper mantle is probably the strongest part of the lithosphere, under the temperature and pressure conditions existing in the collision zones. Hence by accepting a vertically averaged over the thickness of the lithosphere, rather than a detail rheology, we assume that rheological properties of the lithosphere is controlled by those of olivine, the dominant constituent of the upper mantle. Studies on the deformation of the earth materials at laboratory scales (e.g. Goetze 1978) show that steady state creep of most materials obeys a law of the form:

$$\dot{\epsilon} = C(\sigma_1 - \sigma_3)^n \exp(-Q/R\theta) \quad 2.1$$

where $\dot{\epsilon}$ is the strain rate, C, Q and n are experimentally determined constants of materials, σ_1 and σ_3 are the greatest and the least principal stresses, R is the gas constant and θ is the absolute temperature. By vertical averaging on material properties and the deviatoric stress and strain rate, a more useful constitutive law is obtained;

$$\tau_{ij} = B\dot{E}^{(1/n-1)} \dot{\epsilon}_{ij} \quad 2.2$$

where B represents all temperature dependent terms in equation (2.1), throughout the lithosphere, and τ_{ij} and $\dot{\epsilon}_{ij}$ are the components of the deviatoric stress and strain rate tensors, respectively. The strain rate tensor is defined by:

$$\dot{\epsilon}_{ij} = \frac{1}{2} \left(\frac{\partial u_i}{\partial x_j} + \frac{\partial u_j}{\partial x_i} \right) \quad 2.3$$

where u_i is the component of velocity vector along the i th coordinate axis. \dot{E} in

equation (2.2) is the second invariant of the strain rate tensor:

$$\dot{E} = (\dot{\epsilon}_{ij} \dot{\epsilon}_{ij})^{1/2}. \quad 2.4$$

Equation (2.2) is the constitutive relation between stress and strain rate. For Newtonian materials n is unity, and viscosity is constant and strain rate is proportional to stress. When n is greater than unity, the material is called non-Newtonian or power law, and viscosity ($= B\dot{E}^{(n-1)}$) is strain rate dependent. In most geological situations where condition of shear thinning holds, viscosity decreases with increasing stress, and the flow of material tends to concentrate in the regions of highest stress.

5. The flow of the material is considered to be incompressible in three dimensions:

$$\nabla \cdot \mathbf{u} = \dot{\epsilon}_{xx} + \dot{\epsilon}_{yy} + \dot{\epsilon}_{zz} = 0 \quad 2.5$$

in which \mathbf{u} is the velocity vector.

2.2.2 Mathematical formulation

Because of very high viscosity of the lithosphere, the acceleration term in the force balance equation is negligible, and the components of the Navier-Stokes equation become:

$$\begin{aligned} \frac{\partial \sigma_{xx}}{\partial x} + \frac{\partial \sigma_{yx}}{\partial y} + \frac{\partial \sigma_{zx}}{\partial z} &= 0 \\ \frac{\partial \sigma_{xy}}{\partial x} + \frac{\partial \sigma_{yy}}{\partial y} + \frac{\partial \sigma_{zy}}{\partial z} &= 0 \\ \frac{\partial \sigma_{xz}}{\partial x} + \frac{\partial \sigma_{yz}}{\partial y} + \frac{\partial \sigma_{zz}}{\partial z} &= \rho g \end{aligned} \quad 2.6$$

where σ is the stress tensor, ρ is the density and g is the gravitational acceleration.

With the assumptions of zero shear stress at the top and bottom of the sheet, and

negligible topography gradient at the surface, gradients of σ_x and σ_y are negligible and the third component of equation (2.6) will reduce to:

$$\frac{\partial \sigma_{zz}}{\partial z} = \rho g, \quad 2.7$$

indicating that σ_{zz} is a principal stress, and equal to the lithostatic pressure within the lithosphere. The stress tensor is defined by:

$$\sigma_{ij} = \tau_{ij} - \delta_{ij}P \quad 2.8$$

where τ_{ij} are the elements of deviatoric stress tensor and $P = -1/3(\sigma_{xx} + \sigma_{yy} + \sigma_{zz})$ is the pressure. It is assumed that the condition of isostatic equilibrium holds for the crustal thickness variations. Figure 2.1 shows a sketch of the lithosphere. Below the depth of compensation the horizontal gradient of σ_{zz} is taken as zero. At the base of the lithosphere ($z = 0$), σ_{zz} is chosen to be equal to $-P_o$ (compressional stress is assumed to be negative). The top of the lithosphere having crust, is at a level of $z = L + h$, where L is the thickness of the lithosphere without crust. Normal stress at the top is zero. Equations (2.7) and (2.8) yield:

$$\sigma_{zz} = \tau_{zz} - P = g \int_0^z \rho dz + f(x,y). \quad 2.9$$

Using the conditions;

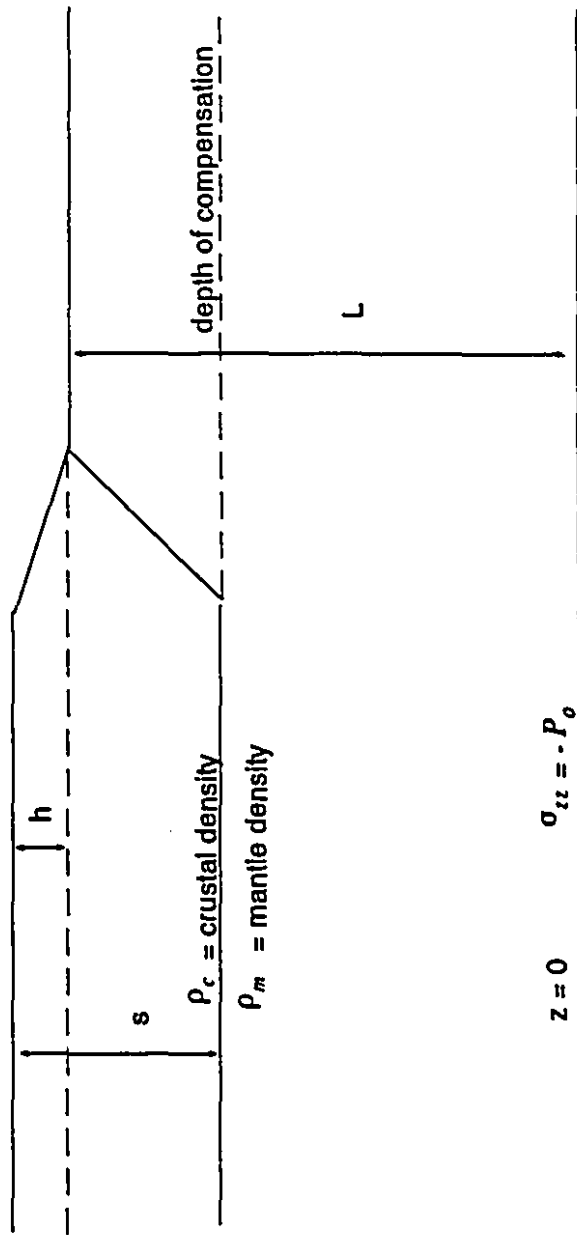
$$\begin{aligned} \sigma_{zz}(z=0) &= -P_o, \\ \sigma_{zz}(z=L+h) &= 0, \end{aligned} \quad 2.10$$

and isostatic equilibrium, the normal stress at the base of the lithosphere is given as:

$$f(x,y) = -P_o = -g \int_0^{L+h} \rho dz = -\rho_m Lg. \quad 2.11$$

Substituting for σ in the first two of equation (2.6) from equation (2.8) yields;

Figure 2.1 A sketch of vertical structure of the lithosphere.



s = crustal thickness
 $L + h$ = thickness of lithosphere having crust

$$\frac{\partial \tau_{xx}}{\partial x} + \frac{\partial \tau_{yx}}{\partial y} = \frac{\partial P}{\partial x} \quad 2.12$$

$$\frac{\partial \tau_{xy}}{\partial x} + \frac{\partial \tau_{yy}}{\partial y} = \frac{\partial P}{\partial y}$$

All the z-dependent terms are omitted since $\sigma_{xz} = \sigma_{zx} = \sigma_{yz} = \sigma_{zy} = 0$.

The next step is to adopt a vertical averaging over the thickness of the lithosphere, of the pressure and deviatoric stress. Using equations (2.9) and (2.11), the averaged pressure p_{avg} , is obtained as:

$$P_{avg} = \bar{\tau}_{zz} + P_o - \frac{g}{L-h} \int_o^{L-h} dz \int_o^z \rho dz \quad 2.13$$

where $\bar{\tau}_{zz}$ is the average of normal stress. The condition of isostatic equilibrium gives:

$$h = s(1 - \rho_c/\rho_m) \quad 2.14$$

with ρ_c and ρ_m as the crust and mantle densities respectively, and s is the crustal thickness. With the help of equation (2.14) and assuming $h \ll L$, equation (2.13) after dropping the subscript and the bar from P and τ_{zz} , becomes:

$$P = \tau_{zz} + \frac{g \rho_c s^2 (1 - \rho_c/\rho_m)}{2L} + \frac{g \rho_m L}{2} \quad 2.15$$

Putting for τ_{ij} and P in equation (2.12) from equations (2.2) and (2.15) and using the continuity equation (2.5) yields:

$$\frac{\partial}{\partial x_\beta} [B \dot{E}^{(1/n-1)} \dot{\epsilon}_{\alpha\beta}] + \frac{\partial}{\partial x_\alpha} [B \dot{E}^{(1/n-1)} (\dot{\epsilon}_{xx} + \dot{\epsilon}_{yy})] = g \rho_c s \frac{(1 - \rho_c/\rho_m)}{L} \frac{\partial s}{\partial x_\alpha}, \quad 2.16$$

$$\alpha, \beta = 1, 2$$

with summation convention over the repeated α and β indices. The right hand side represents the horizontal gradients of forces due to the weight of material, and the terms in the left hand side, show the gradients of forces arising from the ambient strain rates.

Equation (2.16) can be written in the non-dimensional form using the normalization factors:

$$(x', s') = (x, s)/L, \quad u' = u/u_0, \quad t' = tu_0/L, \quad 2.17$$

where t is time and u_0 is a characteristic velocity, taken to be the collision velocity. The final non-dimensionalized force balance equation is:

$$\frac{\partial}{\partial x_\beta} [\dot{E}^{(1/n-1)} \dot{\epsilon}_{\alpha\beta}] - \frac{\partial}{\partial x_\alpha} [\dot{E}^{(1/n-1)} (\dot{\epsilon}_{xx} - \dot{\epsilon}_{yy})] = Ar s \frac{\partial s}{\partial x_\alpha}, \quad \alpha, \beta = 1, 2, \quad 2.18$$

where the Argand number, Ar , is defined by:

$$Ar = \frac{g \rho_c L (1 - \rho_c / \rho_m)}{B (u_0 / L)^{1/n}}, \quad 2.19$$

which signifies the relative importance of buoyancy forces due to crustal thickness contrasts, and viscous forces required to deform the medium.

Equation (2.18) gives the spatial variation of velocity field at each instant of deformation. Once the velocity field is determined, the temporal variation of crustal thickness can be obtained, using the non-dimensionalized continuity equation:

$$\frac{\partial s}{\partial t} = -\nabla \cdot (su), \quad 2.20$$

Equation (2.18) shows that, for a given set of boundary conditions, the flow of material is controlled by two factors: the exponent n in the power law rheology, and the Argand number Ar (England & McKenzie 1982). When Argand number is small, e.g. the viscosity of the lithosphere is large, deformation is controlled by the kinematic constraints imposed at the boundaries. On the other hand, large Argand number indicates that the lithosphere is weak, and it can not sustain appreciable crustal thickness differences.

2.2.3 The results of the model in central Asia

The formulation mentioned above was used by several authors to model the history of deformation in the collision zone of central Asia, since the beginning 30-40 m.y. ago. In all of these works velocity field, principal stress and strain rate fields, and crustal thickness distributions at various stages of deformation for different sets of boundary conditions and rheologies have been calculated. England & McKenzie (1982) carried out finite difference technique on geometries of fixed boundaries. Houseman & England (1986) and Vilotte et al. (1984,1986) used finite element method with more realistic boundary conditions, by choosing a moving boundary, as an effect of a rigid indenter. Also, the effect of lithospheric heterogeneities was studied by Vilotte et al. (1984, 1986) and England & Houseman (1985). The main achievements of these experiments can be outlined as follows:

- All the models have been successful in simulating the diffuse nature of the deformation. The calculated crustal thicknesses span over regions with dimension at least as great as the collision boundary.

- The significance of buoyancy forces in the flow even when the lithosphere is capable of supporting large shear stresses is confirmed. For small Argand numbers, the deformation tends to focus near the influx boundary, producing large elevation contrasts. While for large Argand numbers, the influence of buoyancy forces increases, and deformation shows a more diffuse nature and extends to greater distances away from the indenting boundary, producing smaller elevation contrasts. For Newtonian materials, the scale of sideways flow exceeds the dimension of the influx boundary, while in the case of power law materials, the flow is more restricted and its lateral extension is comparable to the size of the indenter. The models predict that a power law material of n equal to 3 or larger, and Argand number between 1 and 10 can

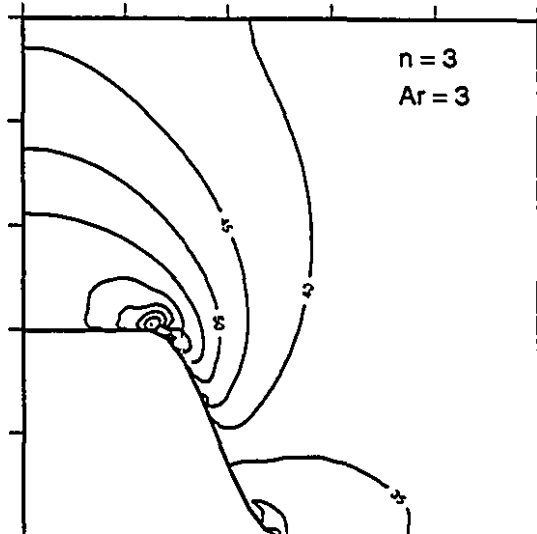
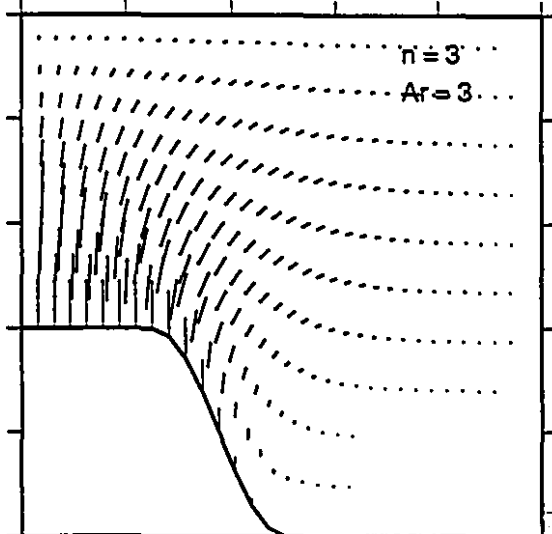
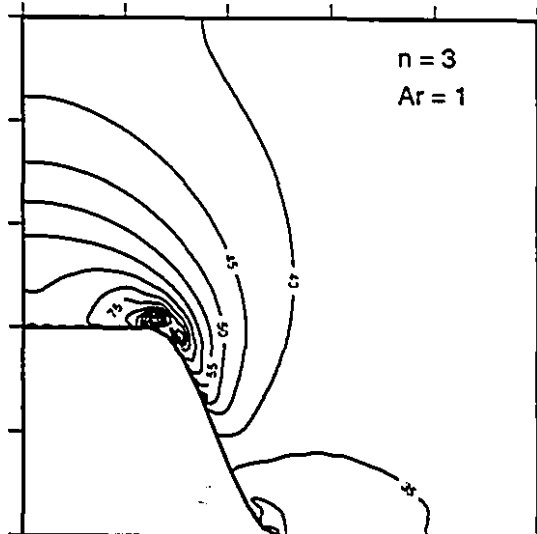
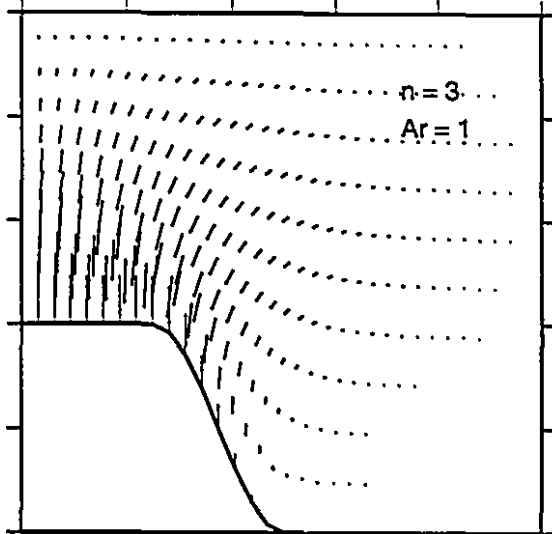
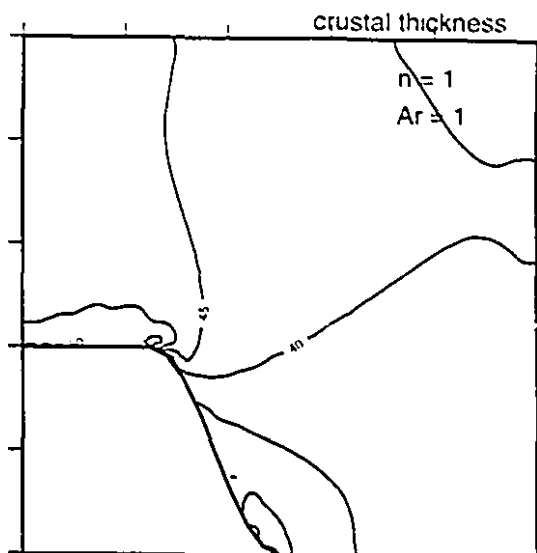
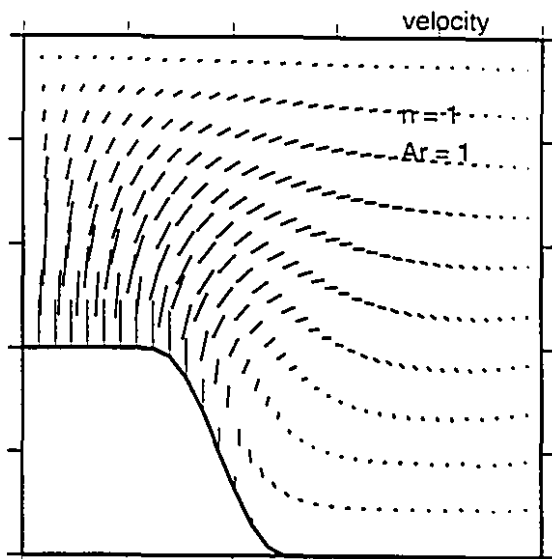
approximate the present day tectonic settings and crustal structure in central Asia.

_ The values for stresses and strain rates obtained in these experiments, are in accord with those obtained from other observations in the collision zones.

_ These models also notice the development of the large along-strike extensions in the regions of substantial crustal thickening, a phenomenon which seems to be a prominent feature in the last stages of deformation of the Tibetan plateau.

Before proceeding to model the deformation of Iran, I tested the continental collision of central Asia, with the geometries and boundary conditions used by England & McKenzie (1982, 1983) and Houseman & England (1986), using the computer program I designed. The results agree with those of the above mentioned authors to better than 5 percent. In Figure 2.2 the velocity fields and crustal thickness distributions for some of the calculations, carried out for the model of Houseman & England (1986), are illustrated.

Figure 2.2 Plots of velocities and crustal thickness distributions after 40 m.y. of deformation in Asia, calculated for the models given by Houseman and England (1986). The dimension of the box is 5000 km in each direction. The position of the indenting rigid plate is drawn in the lower left corner of the box. (a) velocity field for a model with $n = 1$, $Ar = 1$. (b) crustal thickness distribution for $n = 1$, $Ar = 1$, (c) velocity field for $n = 3$, $Ar = 1$. (d) crustal thickness for $n = 3$, $Ar = 1$, (e) velocity field for $n = 3$, $Ar = 3$. (f) crustal thickness for $n = 3$, $Ar = 3$.



Chapter 3

Numerical modelling of deformation in the Iranian plateau

3.1 Initial assumptions

The Iranian plateau is considered as a nearly wedged shape piece of lithospheric plate, located in the convergence zone of the Arabian shield and Eurasian plate. All the numerical studies have been restricted to the investigation of deformation of Iran during the Himalayan-type collision of Arabia and Eurasia, spanned from the Miocene period to the present day, a time interval of 15 million years. It is assumed that the deformation is exclusively controlled by the northeastward motion of Arabia in southwest. Although the importance of all the pre-Neogene deformations is quite evident in the geology of Iran, due to insufficient information on the structure of the crust in the past periods of time, and also to avoid complexity in the models, all the previous orogenic phases have been ignored, and the lithosphere is modelled as a thin flat plate having a uniform initial crust on top. The crust is assumed to be in isostatic compensation, which is supported by the presence of negative Bouguer anomalies (-100 to -200 mGal) over the plateau (Basavaiah et al. 1991).

In order to assess the influence of lateral heterogeneities in lithospheric strength on the tectonics of the plateau, greater rheologies have been assigned to the less deforming blocks of central Iran and southern Caspian. Although some of the smaller features such as the Lut block, could be of significance in smaller scale deformations,

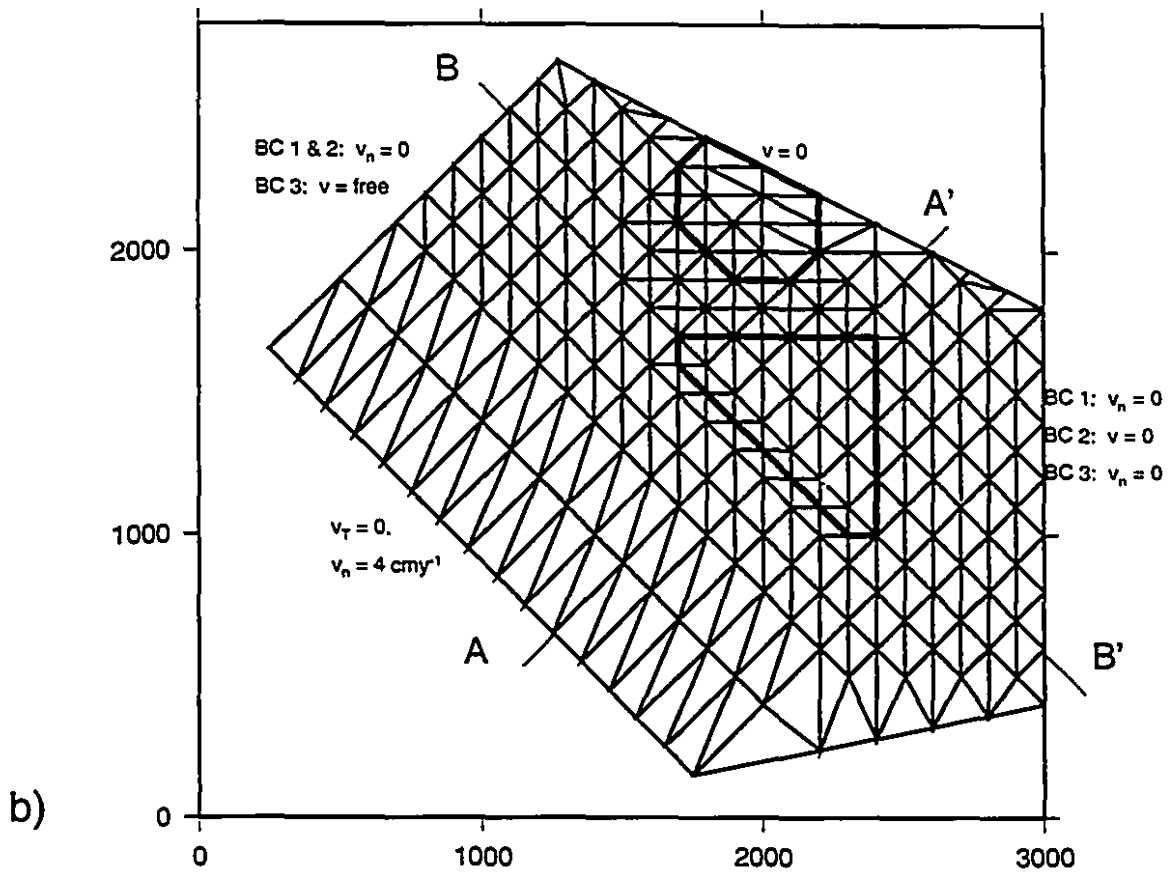
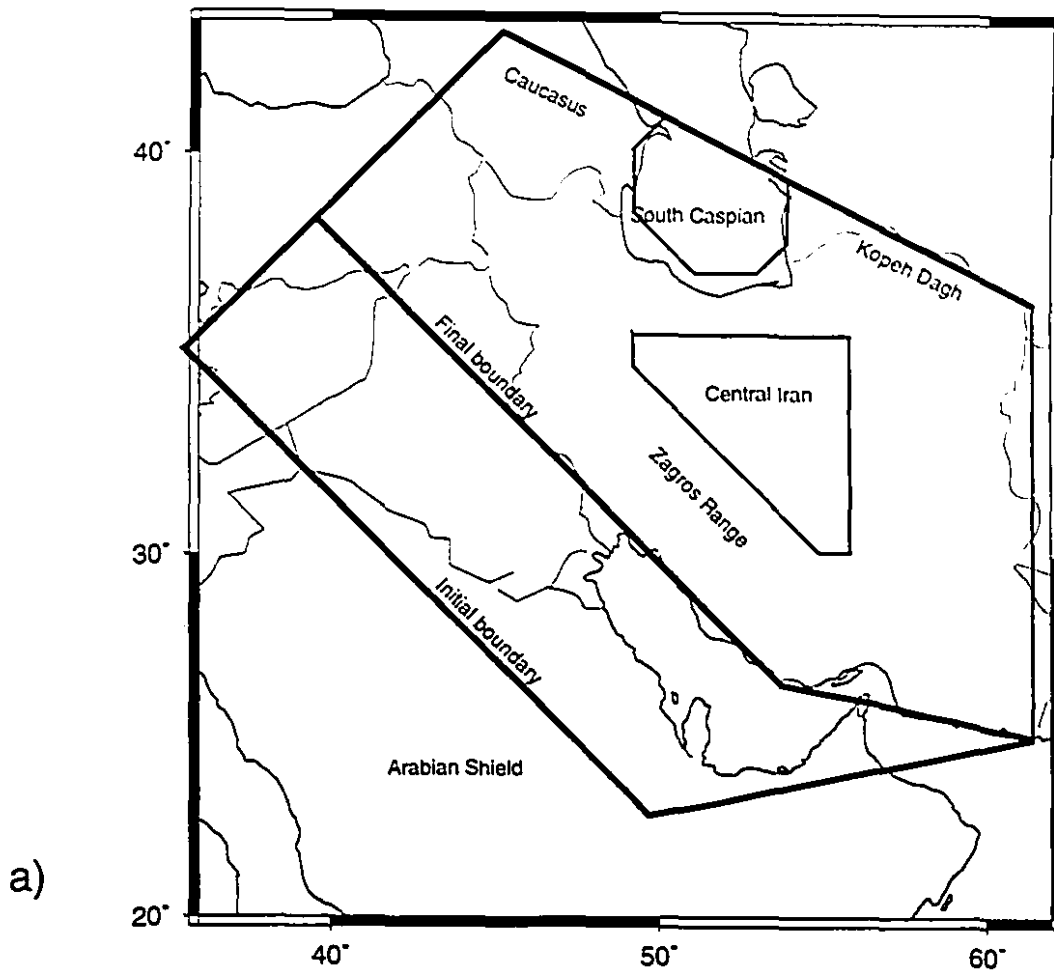
again, it is attempted to keep the lithospheric structure as simple as possible. The evidence for greater rigidity in central Iran is supported by the topographic distributions, and seismic and geopotential studies. In the southern Caspian block, the existence of a basaltic oceanic crust has been inferred through seismic studies.

3.1.1 Geometry of the models

The final geometry of the region of interest is taken to be a pentagonal body surrounding Iran, eastern Turkey, the Caucasus and the southern Caspian block (Figure 3.1a). The Arabian plate has been excluded from the model. It shows only minor deformation (which is not relevant to the current convergent motion) and no seismicity (Nowroozi 1971). It can effectively transmit the forces produced at the Red sea oceanic rift, to the deforming zones in southwestern Iran and eastern Turkey. Therefore instead of placing the southern boundary of the mesh at the Red sea axis, southwestern Iran is taken as the boundary of the grid, where it is the site of the contact of a rigid mass and a deforming belt.

The southern boundary consists of two segments. The longer segment runs almost parallel to the southern foothills of the Zagros mountains and stretches from the vicinity of the conjunction of the northern and eastern Anatolian faults in eastern Turkey, to nearby the strait of Hormoz in the Persian gulf. The shorter segment lies on the southern border of the Makran ranges along the northern coast of the Oman sea. The eastern boundary is a south-north trending line parallel to the fault zones of western Pakistan, and marks the boundary between the western Afghanistan block and eastern Iranian ranges. The northern boundary draws the border between the Eurasian plate in the north, and Kopeh Dagh, southern Caspian block and Caucasus in the south. Finally the western boundary is taken as a line in the direction of shortening in the Caucasus.

Figure 3.1 (a) The geometrical configuration of the finite element grid and its location on the geographic map. The two polygons inside the mesh, correspond to the central Iran and southern Caspian inclusions. (b) The finite element grid and the velocity boundary conditions on each side of the mesh. Each triangle consists of four three-node triangular elements. The grid has a total number of 855 nodes, and 1616 elements. At each boundary all the velocity boundary condition sets are defined. The lines AA' and BB' are used to draw profiles of velocity and crustal thickness. In the subsequent figures the x and y components of the coordinate system are in west-east and south-north direction, respectively.



and separates it from central Turkey and the Black sea.

The initial shape of the mesh is then constructed, by stretching the southern and western boundaries, back to their position in 15 million years ago, assuming that the convergence has had a constant rate over the deformation period. This assumption is supported by the data derived from magnetic strip anomalies (Mohajer-Ashjai et al. 1975). In Figure 3.1a the actual location of the mesh before and after deformation, is depicted on the geographic map. For heterogeneous models the shape and dimensions of central Iran and the southern Caspian block, are inferred from topography patterns and earthquake epicenter distribution in Iran. Both regions show low relief topography and sparse earthquake activity. Central Iran is bounded by some major fault zones (Takin 1972) such as Doruneh fault in the north, and Naiin fault in the west and southwest (see Figure 1.2).

3.1.2 Initial and boundary conditions

All the boundary conditions in the models are given in terms of prescribed boundary velocities and crustal thicknesses. The estimated convergence rate between Arabia and Eurasia ranges from 5 cm y^{-1} (Ni & Barazangi 1986) to 4 cm y^{-1} (DeMets et al. 1990) in the north-northeast direction. Here, a constant velocity of 4 cm y^{-1} in the $\text{N}45^\circ\text{E}$ direction along the southern boundary (the Zagros part) is taken, and it is assumed that velocity does not change during the time of deformation. As for the Makran subduction zone, although the rate of subduction is at least equal to the rate of continental convergence in the Zagros, nevertheless since there is no flow of continental material inland Makran, the boundary velocity is assumed to be linearly decreasing to zero towards the eastern end. On the eastern side, two possible boundary conditions are considered: a) fixed boundary with zero velocities and b) free slip with zero normal

velocity along the boundary. The second choice is assumed, in order to study the possible effects of north-south trending strike-slip zones in the east of Iran (Jackson & McKenzie 1984). The northern boundary is kept fixed (i.e. zero prescribed velocity) where it is believed to be the site of compression of northern Iran and the Caucasus against Eurasia. As for the western boundary, again, two different boundary conditions are investigated: a) zero motion normal to the boundary and prescribed tangential velocity linearly decreasing to zero towards the northern end, and b) free-stress condition. The logic behind the first option comes from the observation that most of the motion in the Caucasus is taken up in the form of folding and thrust faulting in the northeast direction. The second option is chosen to examine the influence of overthrusting of the Caucasus on the Black sea, on the stress fields in the western part of the models. In Figure 3.1b all the boundary condition sets are specified.

For all of the numerical experiments a constant initial crustal thickness of 35 km everywhere in the mesh is selected, and is assumed to be fixed on all the boundaries.

3.1.3 Physical parameters

The characteristic parameters which govern the deformation with a given boundary conditions are n , the exponent in the power law rheology and non-dimensional Argand number, Ar . In this study the influence of different values of n and Ar on the deformation is systematically studied. The choices of n are 1, 3, 5 and 10 and those of Argand number are 0, 1, 3, 10 and 30. In the heterogeneous models, the rheology contrast of the inclusions are expressed in terms of Argand numbers:

$$R = Ar_2 / Ar_1, \tag{3.1}$$

where R is the rheology contrast, and numbers 1 and 2 stand for the finite elements

associated with the inclusions and the rest of the mesh, respectively. Having all other physical parameters constant, smaller Argand number means stronger lithosphere. Rheology contrasts of factor of 2 and 5 are examined in the experiments.

In addition to power law exponent and Argand number, other physical parameters used are:

Lithospheric thickness,	($L = 100$ km),
crustal density,	($\rho_c = 2950$ kg m ⁻³),
mantle density,	($\rho_m = 3300$ kg m ⁻³) and
gravitational acceleration,	($g = 9.81$ m s ⁻²).

3.2 Results of numerical experiments

The finite element formulation of equations of flow are discussed in detail in the Appendix. The finite element mesh representing the lithosphere consists of 855 nodes and is divided into 1616 three-node triangular elements. For each experiment, the flow field, crustal thickness variation, rate of vertical deformation, principal stresses, maximum shear stress and strain rate fields, and surface topography maps and profiles in various stages of deformation are calculated. The results are presented as isovalue contour maps, vector maps and cross sections. Velocities and crustal thicknesses are calculated at the nodal points of the grid, and all the stresses and strain rates are calculated at the elemental Gaussian quadrature integration points. Only some of the elements are considered, to avoid crowding on the symbol maps.

In the following, the results of calculations for homogeneous and heterogeneous models with different values of parameters n and Ar and different boundary conditions, are presented and discussed.

3.2.1 Homogeneous models

3.2.1.1 Models with $Ar = 0$

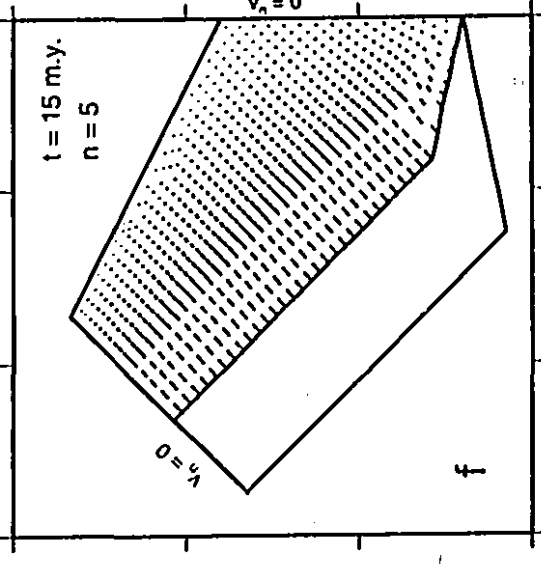
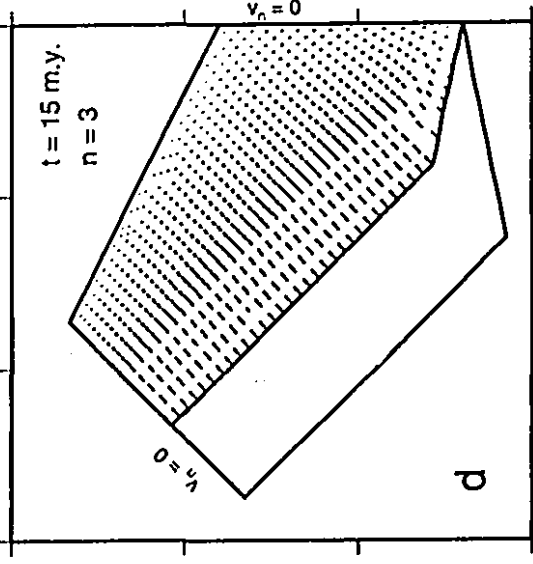
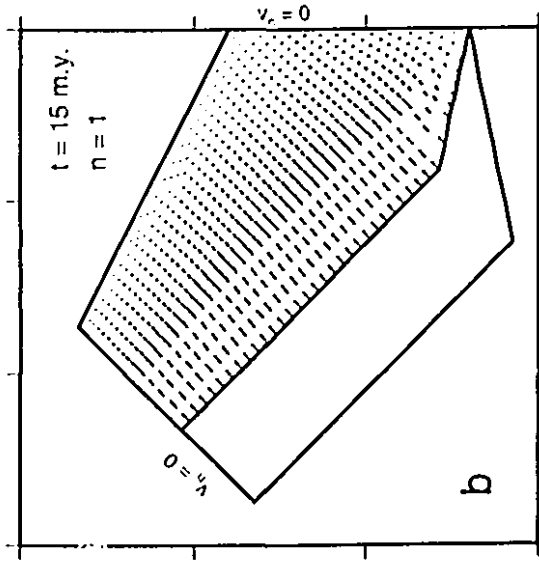
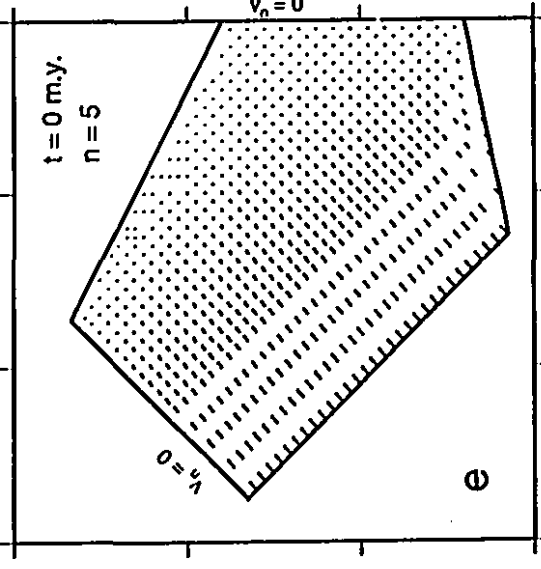
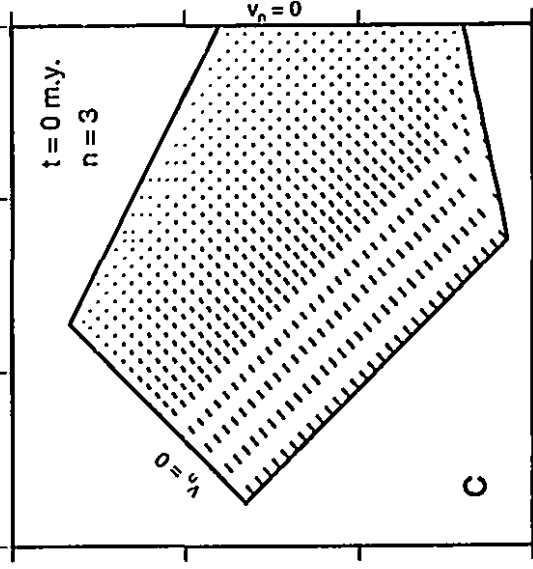
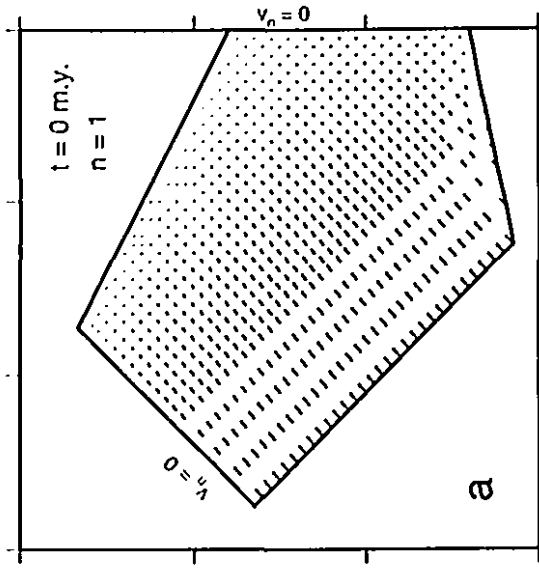
When Argand number is zero, the viscosity of the medium is undefined, and the effects of crustal thickness contrasts on the deformation are neglected. Under these circumstances, equations (2.18) and (2.20) decouple, and the flow will be controlled only by velocity boundary conditions, and will be independent of time (provided the boundary conditions do not change in time). Incompressibility of the material however, will produce crustal thickness differences, as a result of variations in the gradients of flow in the medium.

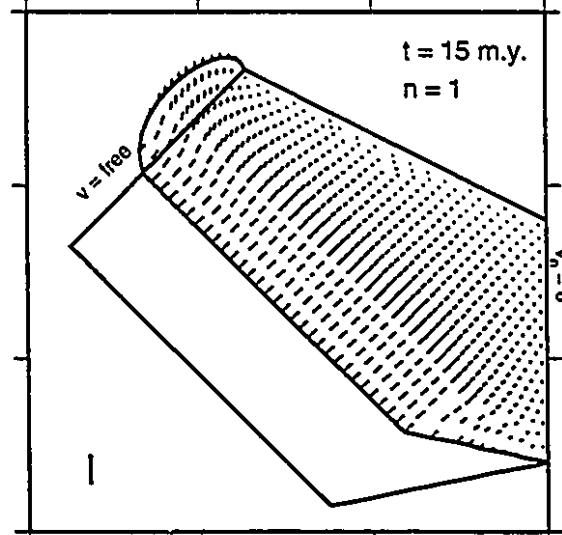
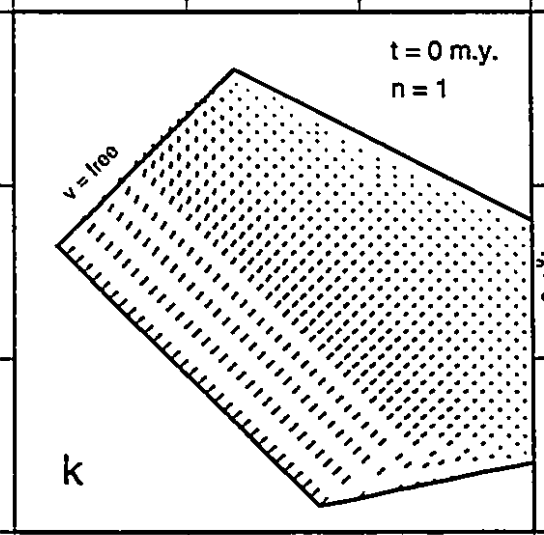
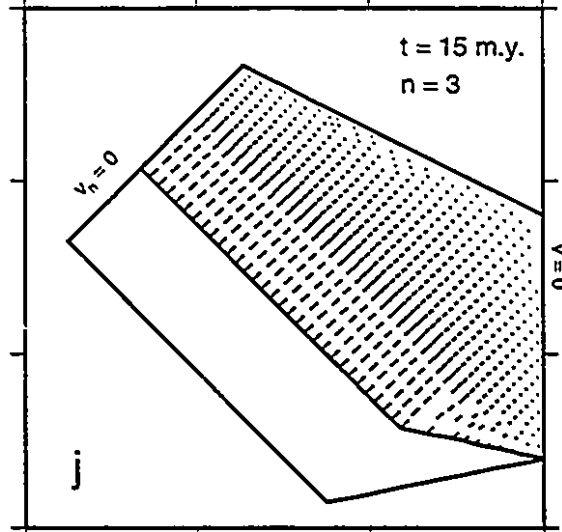
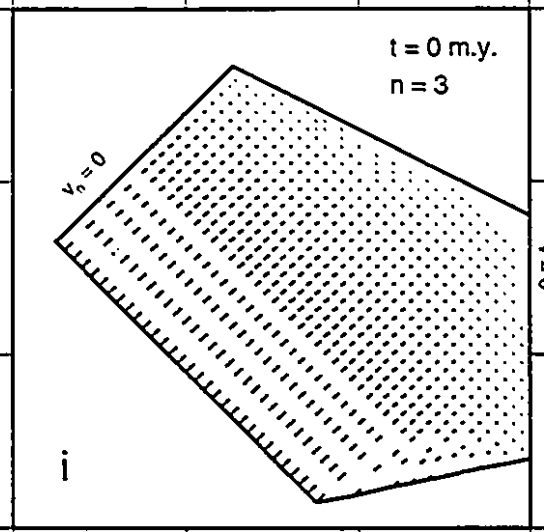
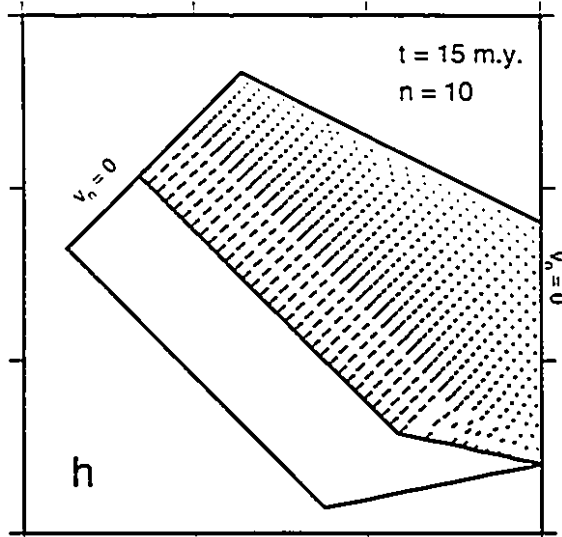
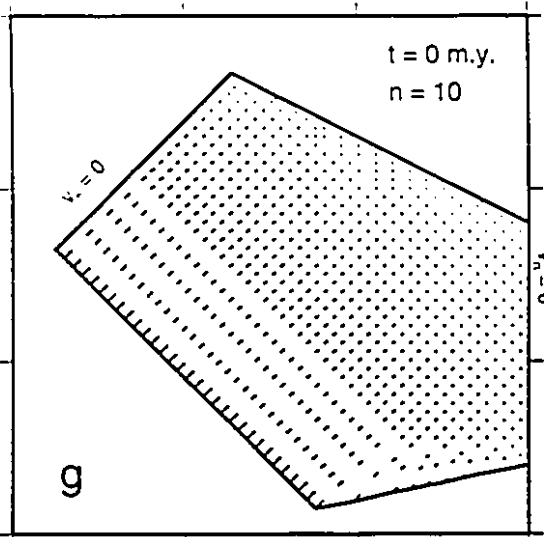
Velocity field

In Figure 3.2 the velocity fields for fluids with different values of n , different boundary conditions, and at different stages of deformation are illustrated. The Figure implies that even in the initial time steps, the extent of deformation reaches the northern boundary, and the choices of large numbers of power law exponent do not prohibit the deformation in the areas far from the indenting (i.e. southern) boundary. This can be due to the fact that the length of the indenting boundary is much larger than the width of the deforming zone. There are two factors that control the flow field; the boundary conditions, and rheology, with the first one being the dominant one. The effect of each of these factors on the velocity patterns is described separately.

The general sense of motion in all models is a southwest-northeast direction arising from south, with a monotonic decrease in magnitude towards the northern boundary. As it is expected, both components of the velocity vector vanish at the fixed

Figure 3.2 Velocity fields for homogeneous models with $Ar = 0$ at $t = 0$ and $t = 15$ m.y.. (a)-(b) velocity field for a Newtonian material and boundary condition set 1. (c)-(d) velocity field for a non-Newtonian material ($n = 3$) and boundary condition set 1. (e)-(f) velocity field for a non-Newtonian material ($n = 5$) and boundary condition set 1. (g)-(h) velocity field for a non-Newtonian material ($n = 10$) and boundary condition set 1. (i)-(j) velocity field for a non-Newtonian material ($n = 3$) and boundary condition set 2. (k)-(l) velocity field for a Newtonian material and boundary condition set 3. The velocity vector at the southern boundary is equal to 4 cm y^{-1} .

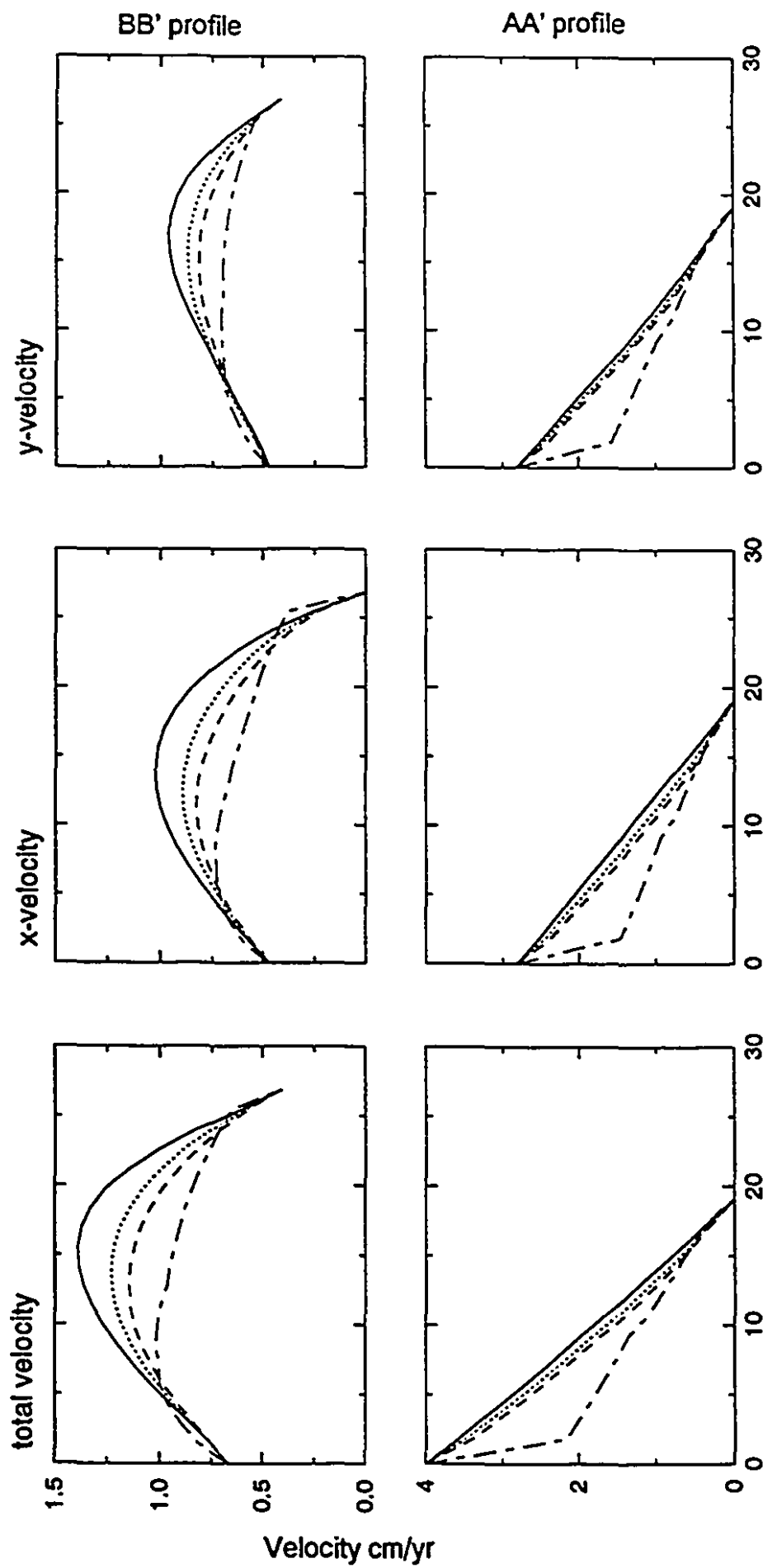




northern boundary. In the eastern boundary, replacing the fixed boundary with a slip-free one, produces a northward flow of material along the boundary (compare the directions and magnitudes of velocity vectors in the vicinity of the eastern boundary in Figures 3.2h and 3.2l with those in Figure 3.2j). Unlike the eastern end where the influence of different boundary conditions is restricted to the eastern part of the mesh, the choice of stress-free side on the western boundary has a profound effect on the entire flow field (Figure 3.2k-l). The fixed boundaries in the east and north, cause a divergence of the velocity vectors towards west, allowing the fluid to escape through the western boundary. The velocity vectors in the middle part of the mesh are generally in N45°E direction. Towards the western end of the mesh, the y-component (in the south-north direction) of the velocity gradually increases, resulting in an anti-clockwise rotation in the velocity field.

In Figure 3.3 profiles of absolute velocity and its two components along the lines AA' and BB' in Figure 3.1b, for different boundary conditions and different rheologies at time $t = 0$, are shown. On the AA' line, the profiles have more or less similar shapes. In the case of boundary condition set 3, the magnitude of x-component of velocity is decreased (about 0.2-0.4 cm y^{-1} for highly non-Newtonian materials) compared to that of the y-component, which is the result of westward rotation and outflow of material through the western boundary. On the BB' line, the effect of boundary conditions on the velocity field is more visible. For experiments with boundary condition sets 1 and 2, the magnitudes of the two components of velocity in most parts of the mesh (the region between 500-2500 km from the western boundary), are almost equal and both fall in the range of 0.5 to 1.0 cm y^{-1} . Whereas for the boundary condition set 3, the profiles have different shapes, and there is a significant decline in the magnitude of x-velocity (0.3-0.5 cm y^{-1}) while the absolute magnitude of y-velocity remains almost unchanged. All these differences in the velocity field, result

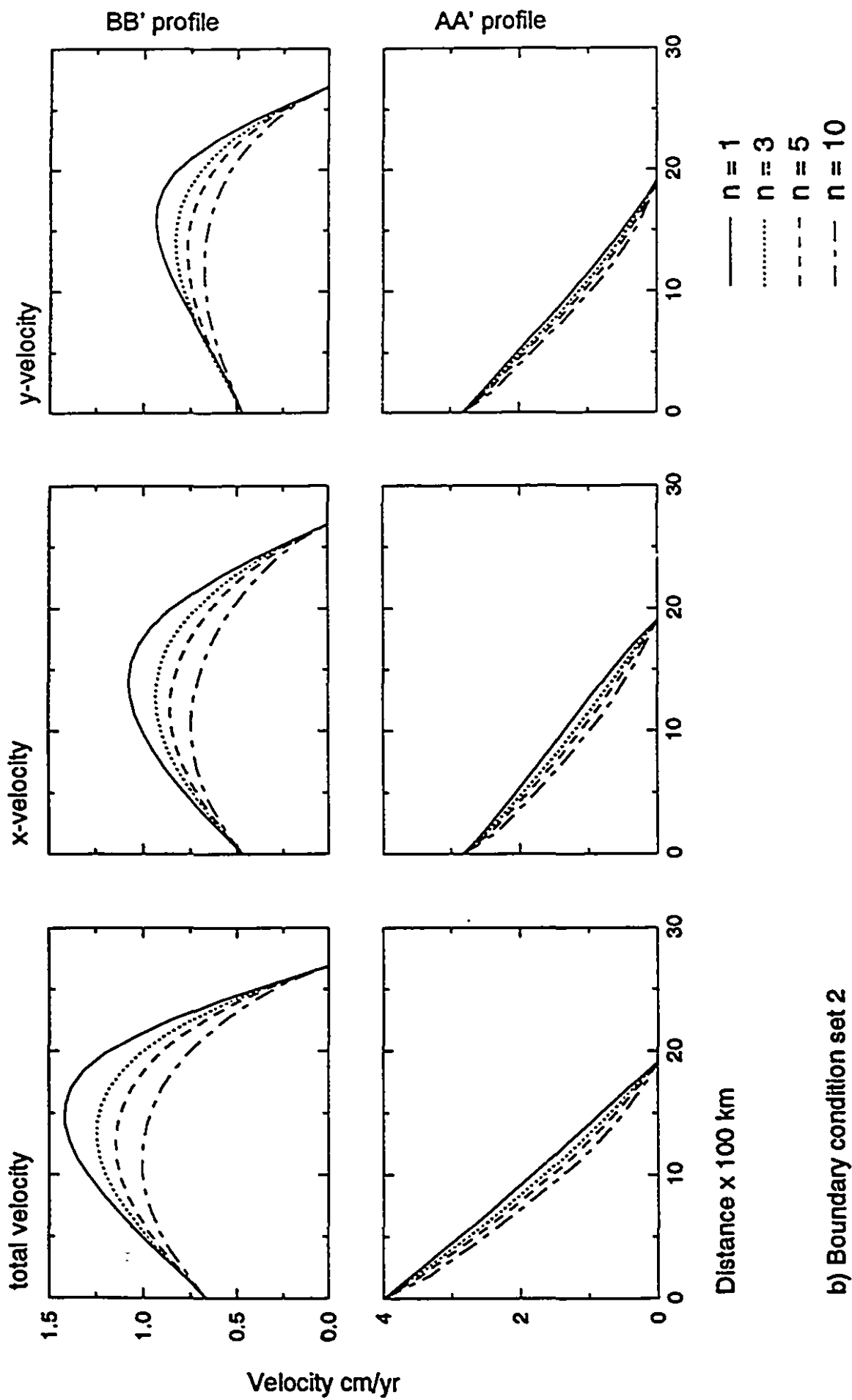
Figure 3.3 Velocity profiles for homogeneous materials with different rheologies and boundary condition sets along the profiles AA' and BB' in Figure 3.1b., (a) models with boundary condition set 1. (b) models with boundary condition set 2. (c) models with boundary condition set 3.



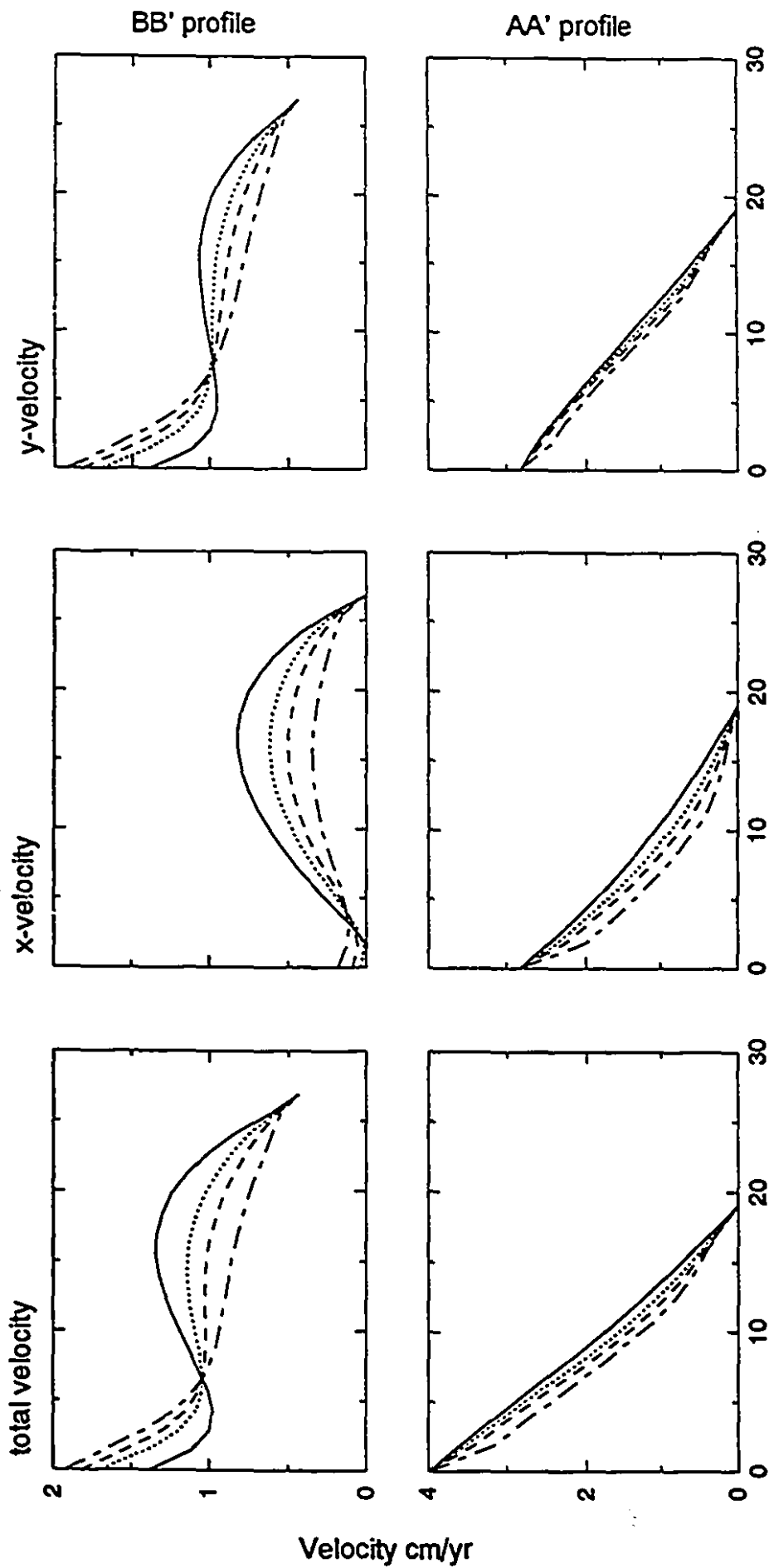
Distance x 100 km

- $n = 1$
- $n = 3$
- - - $n = 5$
- · - · $n = 10$

a) Boundary condition set 1



b) Boundary condition set 2



— $n = 1$
 $n = 3$
 - - - $n = 5$
 - · - · $n = 10$

Distance x 100 km

c) Boundary condition set 3

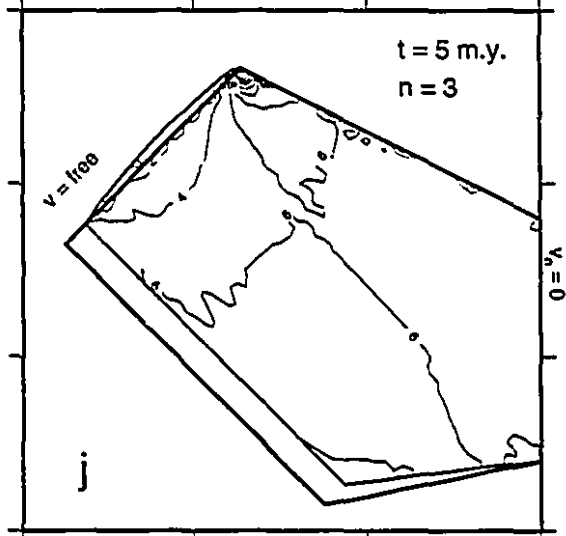
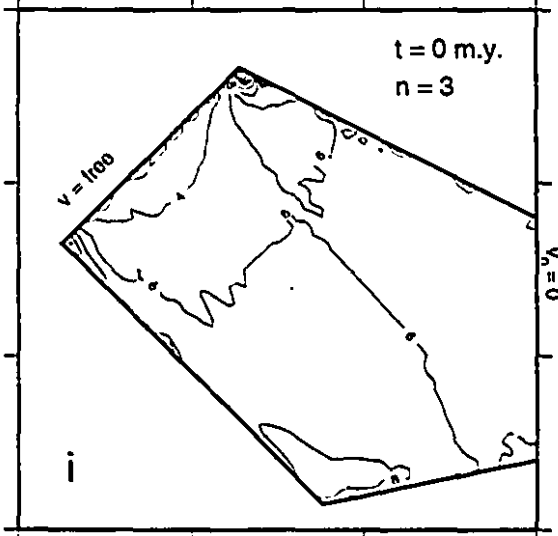
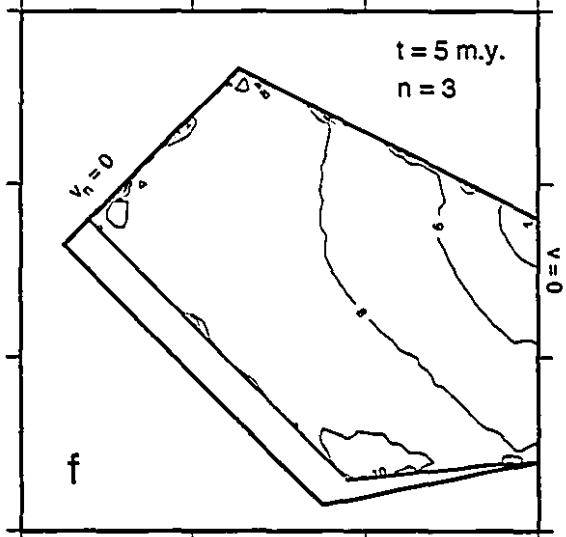
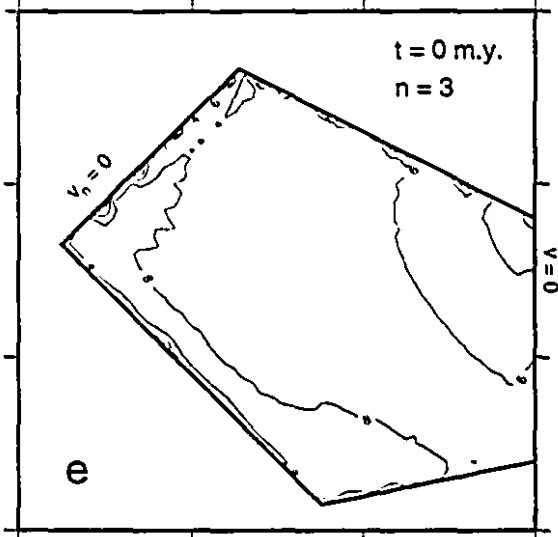
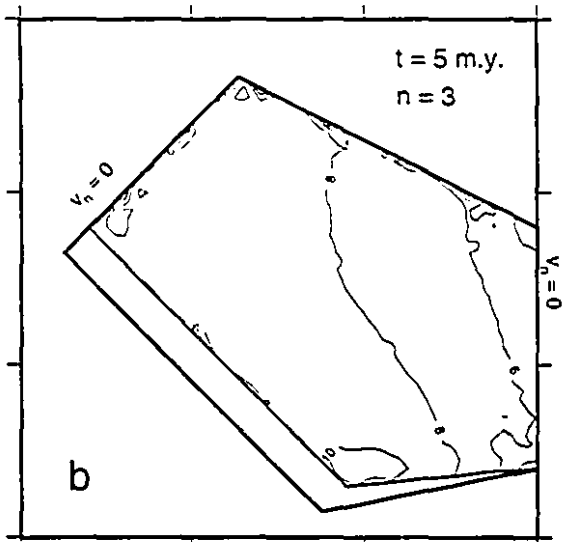
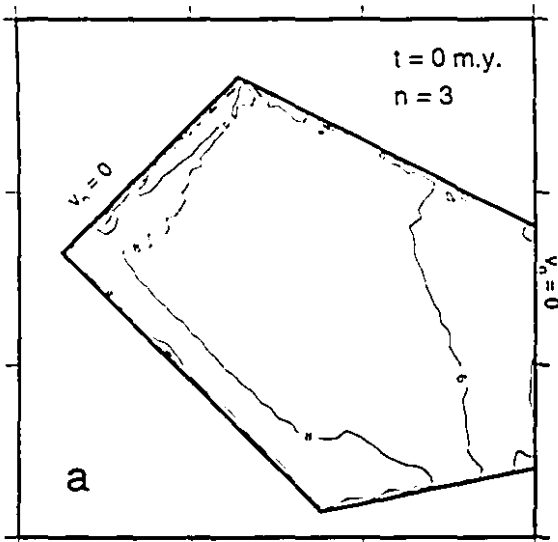
in greater gradients of crustal thickening in the western side of the deforming mesh.

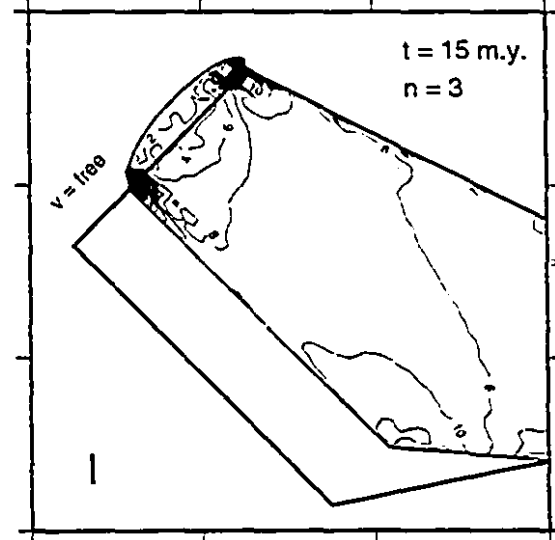
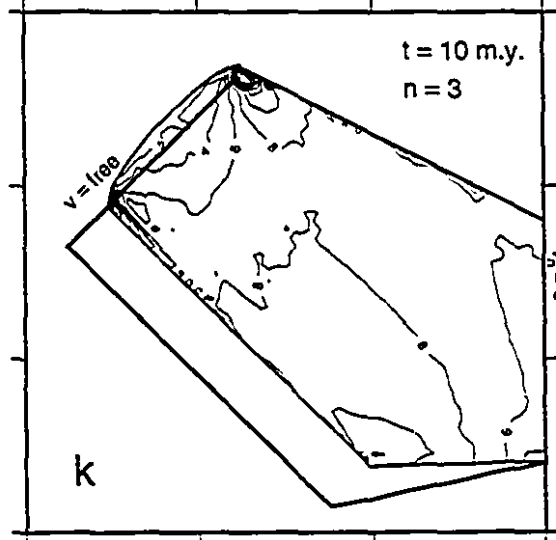
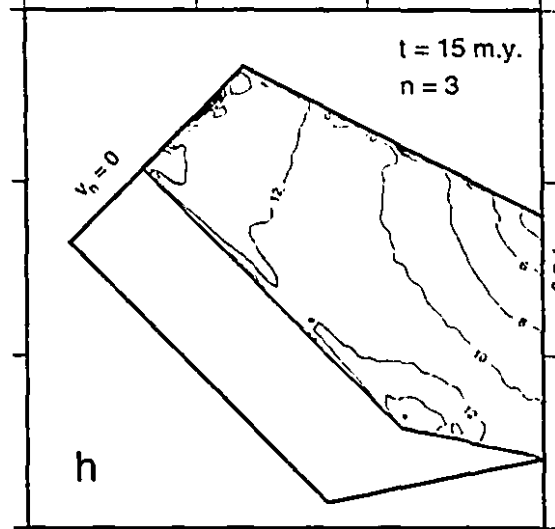
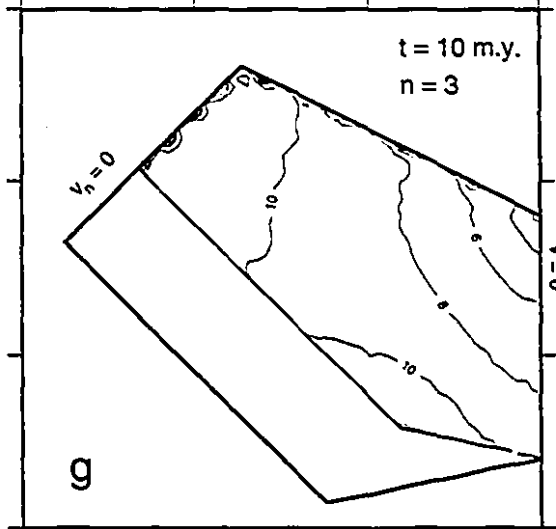
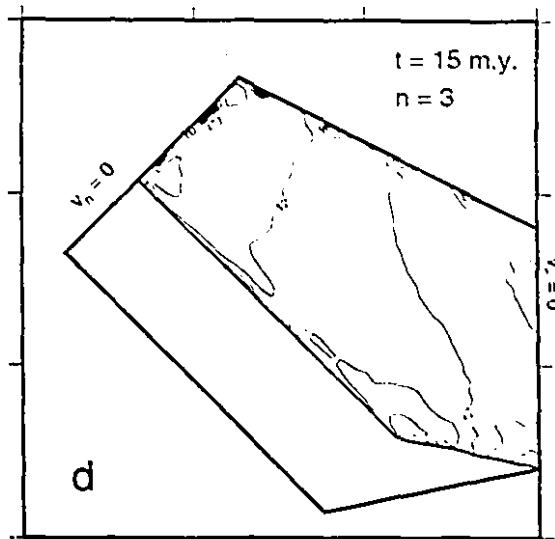
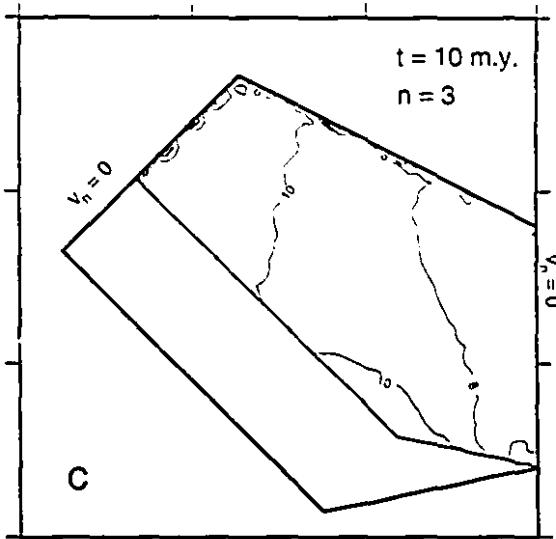
The velocity field is also affected by rheology of the medium through the exponent n . The effect of nonlinearity is similar for all kinds of boundary conditions. Figure 3.3 (profiles along AA') shows that, as n increases from 1 to 10, the flow of material progressively concentrates in front of the southern boundary. For Newtonian material the viscosity of the medium is independent of stress and constant everywhere (putting n equal to unity in equation (2.18) reduces the viscosity to a constant number). However when n is greater than unity, viscosity becomes a function of stress. As a result, viscosity decreases with increasing stress, and deformation tends to concentrate in the regions of highest stress. Therefore, for increasing values of n the gradient of velocity becomes steeper near the southern boundary where stress is at maximum. The shapes of velocity profiles along the line BB' can be explained in a similar way. Near the eastern and western boundaries where shear stresses are large, gradients of velocity are also large. With increasing distance from the boundaries, shear stresses decrease and the medium becomes highly viscous in the center of the mesh, resulting in smoother gradient of velocity and flatter curves for large values of n . As a general conclusion, as the viscosity becomes more dependent on the stress field, the flow of material becomes more concentrated around the boundaries of the mesh.

Strain rate fields

Figures 3.4-3.6 show the time evolution of the vertical strain rate, $\dot{\epsilon}_{zz}$ (instantaneous rate of thickening or thinning) and maximum shear strain rate fields, for different rheologies and boundary conditions. The patterns of instantaneous vertical deformation in Figure 3.4 are almost similar for boundary condition sets 1 and 2. The main difference is that for the free-slip boundary in the east, the greater velocities along

Figure 3.4 Vertical strain rates for homogeneous models with $Ar = 0$, at time steps of 5 m.y. All the contours are in units of $10^{-16} s^{-1}$. (a)-(d) non-Newtonian material ($n = 3$) with boundary condition set 1, (e)-(h) non-Newtonian material ($n = 3$) with boundary condition set 2, (i)-(l) non-Newtonian material ($n = 3$) with boundary condition set 3.





the boundary lead to pronounced motion of crustal material towards the north. Therefore, strain rates become greater and have smoother gradients along the boundary.

The thickening of the crust at all times tends to concentrate around the southern boundary, and in the narrower part of the mesh near the western boundary. The smallest rate of thickening occurs close to the northeastern corner of the mesh, where the flow rate has the lowest magnitude. As time proceeds, the rate of crustal thickening in all of the models shows a steady increase everywhere in the mesh. The location of the maximum thickening rate seems to be in front of the hinge point on the southern boundary. This is due to the nature of the boundary condition at that point. The reason for greater rate of thickening in the western part is that, as the southern boundary advances northward, the horizontal area of the mesh decreases faster in this part than in the other parts of the mesh. Therefore there is increasingly less space for horizontal flow and more chance for vertical deformation. A reverse process takes place when the western boundary is free to move outward (Figure 3.4i-1). In this case the absence of a confining boundary makes the buoyancy forces strong enough to prevent the crust from extensive thickening.

The effect of rheology on the vertical rate of deformation is depicted in Figure 3.5, in which contours of vertical strain rate are plotted at $t = 15$ m.y., for four different values of n and boundary condition set 1. The same as the velocity fields, the transition from Newtonian material to a highly non-Newtonian, results in progressive concentration of deformation around the indenting boundary. However as the nonlinearity decreases, horizontal variations of vertical strain rate within the mesh become smoother, and the regions far from the indenting boundary (e.g. northeastern parts), experience more crustal thickening.

The maximum shear strain rate fields are presented in the form of isovalue contour maps. Figure 3.6 shows the results of calculations for experiments with $n = 1$.

Figure 3.5 Vertical strain rates at $t = 15$ m.y. for homogeneous models with $Ar = 0$ and boundary condition set 1. (a) $n = 1$, (b) $n = 3$, (c) $n = 5$, (d) $n = 10$. Contours are in units of 10^{-16}s^{-1} .

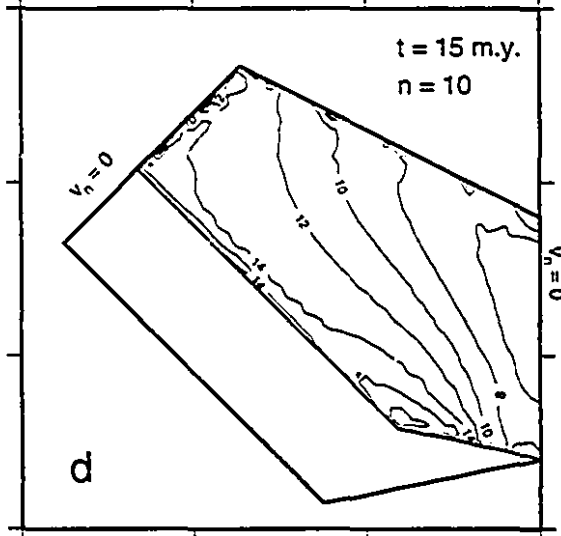
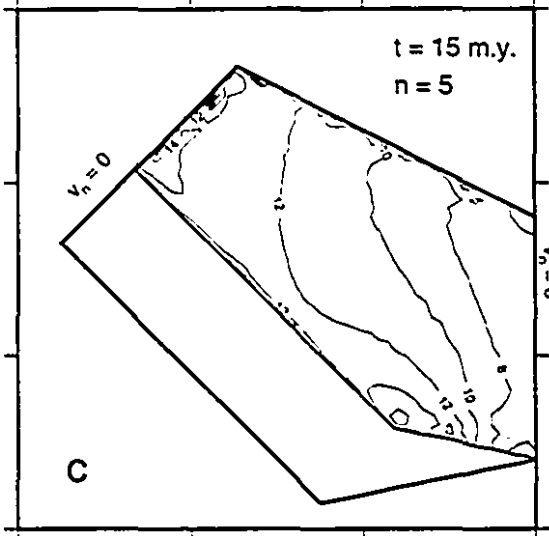
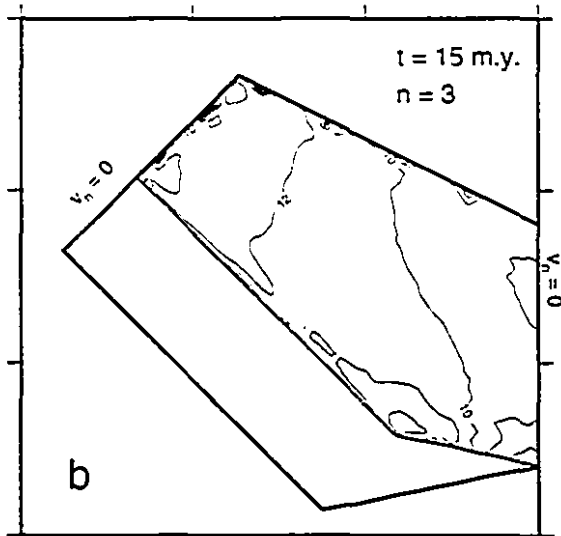
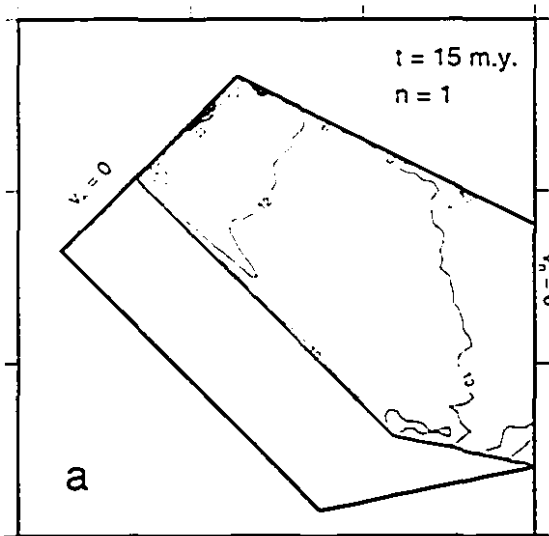
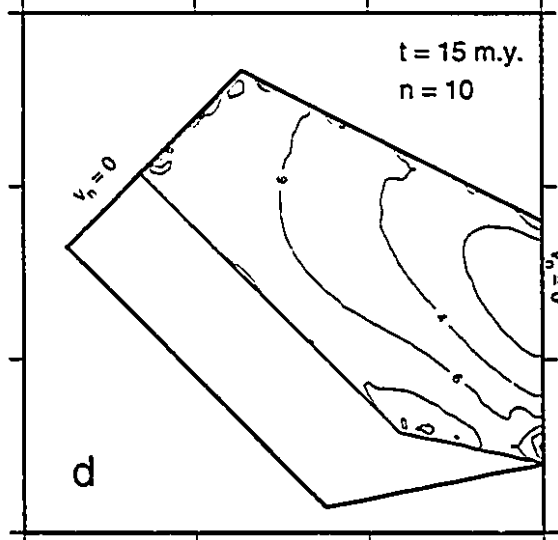
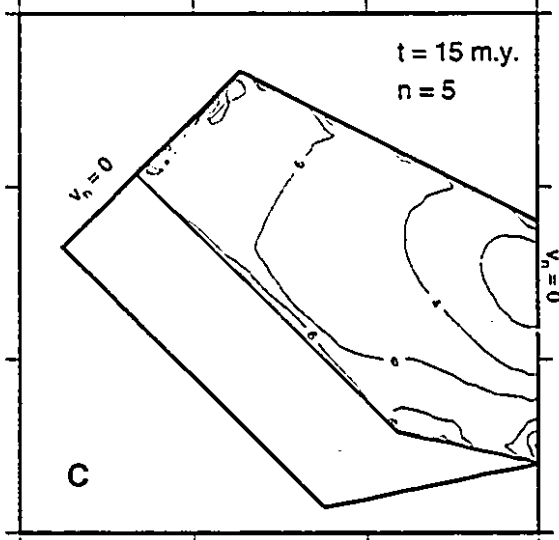
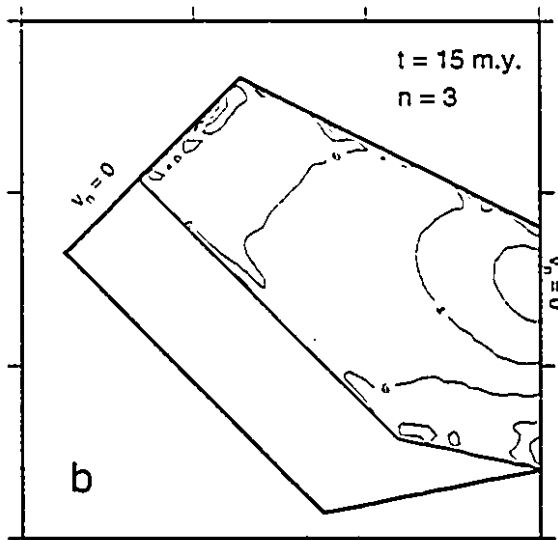
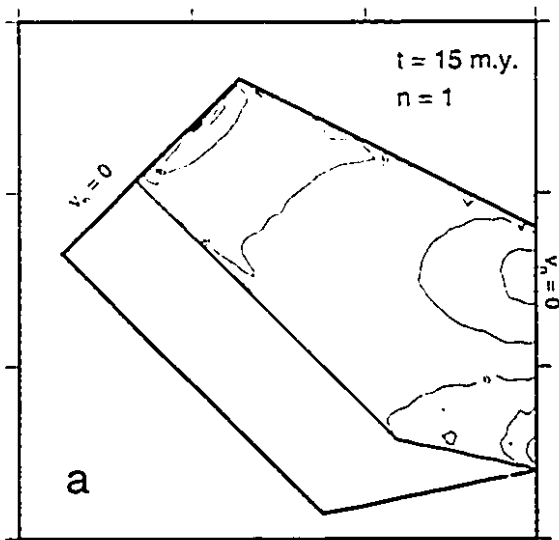


Figure 3.6 Shear strain rates at $t = 15$ m.y. for homogeneous models with $Ar = 0$ and boundary condition set 1. (a) $n = 1$. (b) $n = 3$. (c) $n = 5$. (d) $n = 10$. Contours are in units of 10^{-16}s^{-1} .



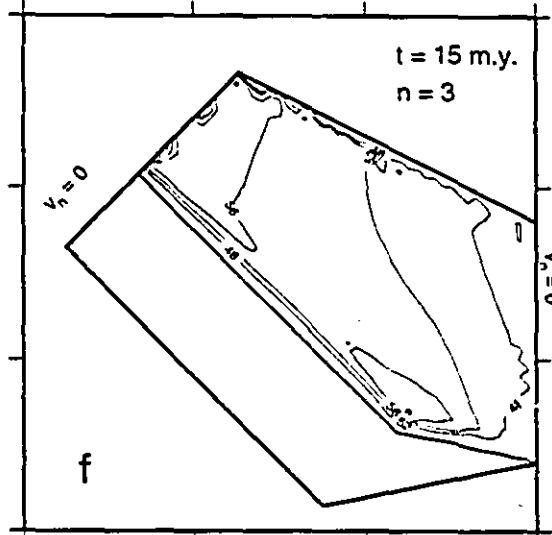
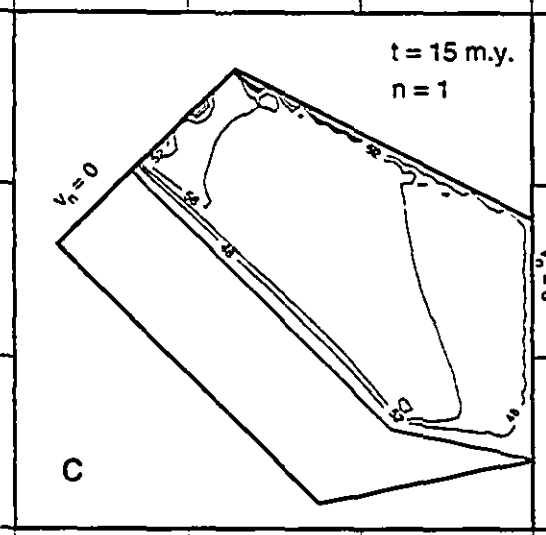
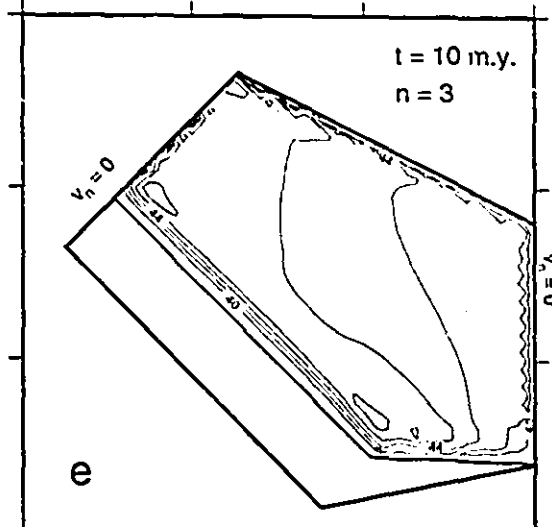
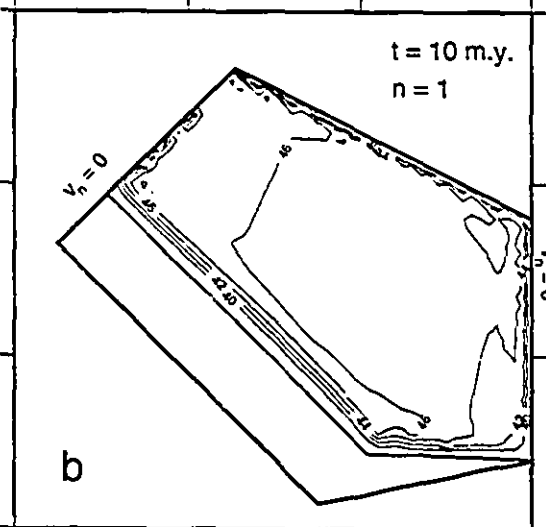
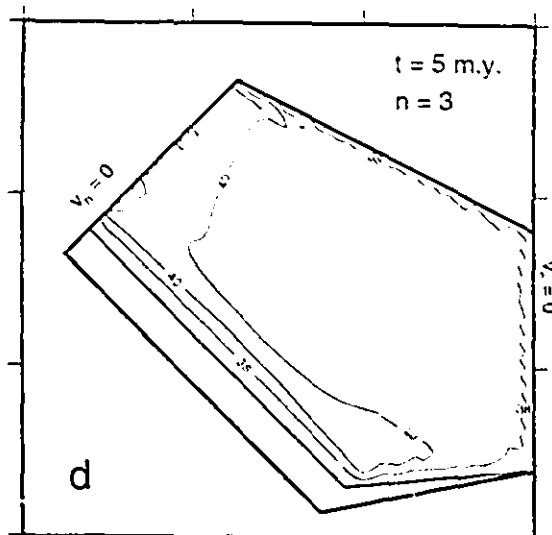
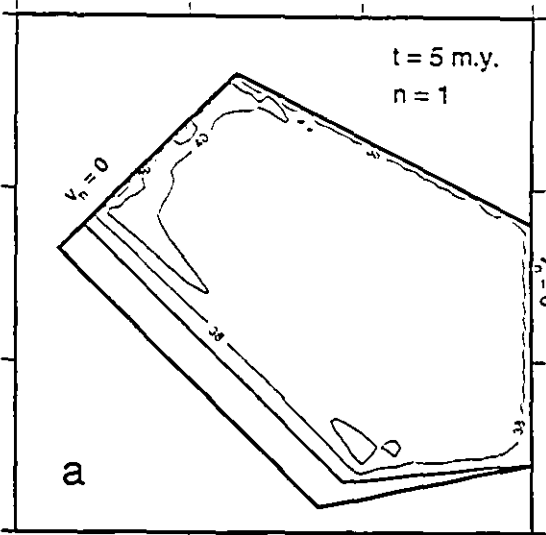
3, 5 and 10. Similar patterns to those of the vertical strain rate can be seen in these plots. Most of the shearing happens near the moving boundaries in the south and west. The maximum is along the smaller segment of the southern boundary, where there is a major gradient of velocity along the boundary. In the region immediately in front of the northern boundary, pure shear strain tends to increase. This is because, the advancement of the boundary produces a greater amount of compressive shortening in southwest-northwest direction and a less amount of extension in northwest-southeast direction. Comparison of the results for different values of n reveals that, the gradients of maximum shear tend to develop in northwest-southeast direction, for smaller numbers of n , whereas shear strain rate in this direction for larger values of n , is more uniform and the gradients are in the direction of flow. This is in accord with the velocity fields described in the previous section. It can be seen that, power law materials have gentler gradients in the middle of the mesh along the profile BB'.

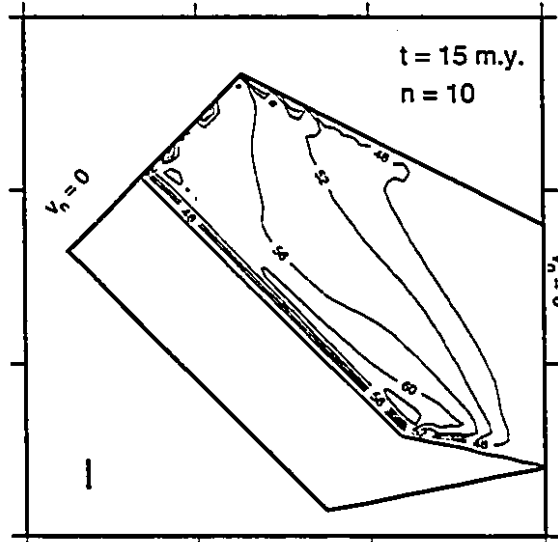
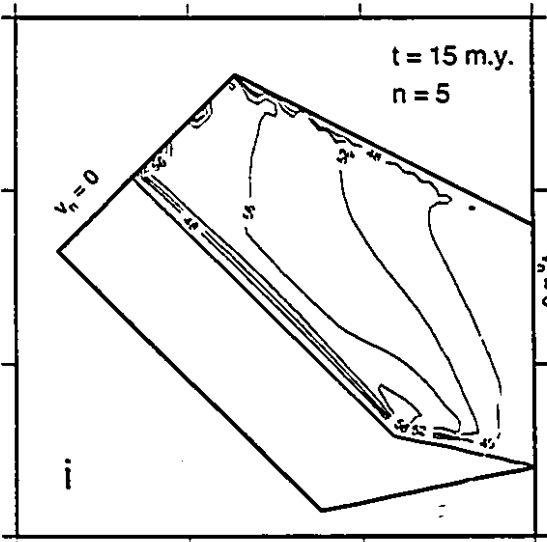
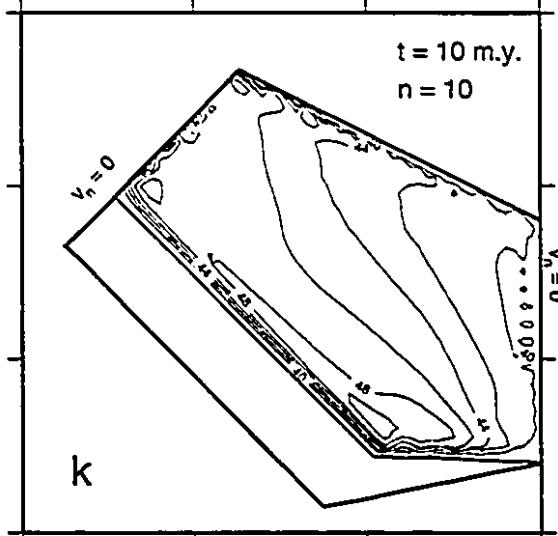
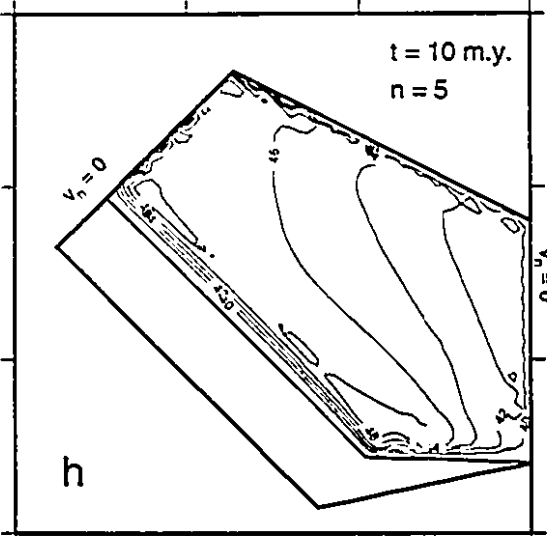
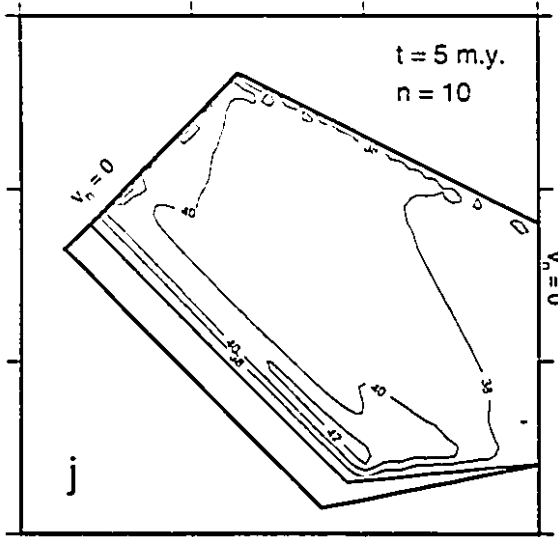
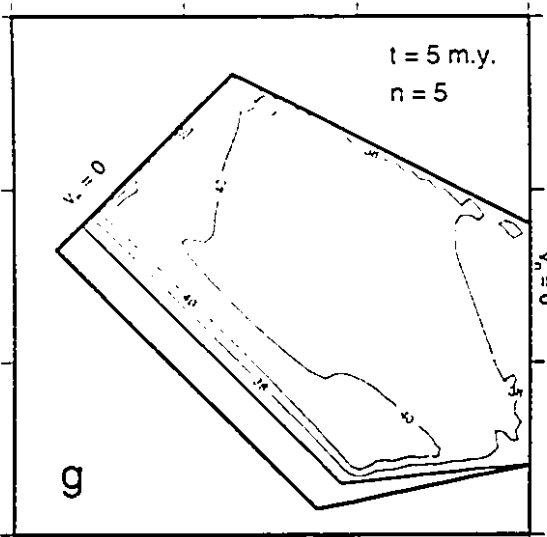
Shear strain rates in general, increase as deformation proceeds. The extent of the deforming mesh in the northwest-southeast direction remains almost unchanged during the deformation, while there is a persistent shortening in the direction of flow. Thus the difference between horizontal principal strain rates continues to increase in time, and greater shear deformation develops. This is best seen in the western part of the mesh in the cases of a fixed boundary (boundary condition sets 1 and 2), where the rate of shortening is at the maximum. On the other hand, a free boundary significantly decreases the rate of northeastward compression and, subsequently, the rate of shearing along the western boundary.

Crustal thickness

The crustal thickness variations follow, but do not exactly match, the vertical

Figure 3.7 Crustal thickness development at time intervals of 5 m.y., for homogeneous models with $Ar = 0$ and boundary condition set 1. (a)-(c) $n = 1$. (d)-(f) $n = 3$. (g)-(i) $n = 5$. (j)-(l) $n = 10$. Contours are in units of 1 km.





strain rate field. This is because a) the vertical strain rate is a measure of the instantaneous vertical deformation while crustal thickness is the integral of the total deformation since the time zero, each carries different information about the evolution of the deformation, and b) the continuity equation (2.20) is solved in Lagrangian description, and the time variation of the crustal thickness is calculated with respect to the moving points within the flow, rather than to a point fixed relative to the mesh.

In Figure 3.7 the crustal thickness development of the mesh at time intervals of 5 m.y., for four values of n and boundary condition set 1, is illustrated. The Figure suggests that, although the lithosphere is chosen to be arbitrarily strong, the extent of deformation quickly reaches to the northern edge of the mesh, even when n has very large value. The area of maximum thickened crust is located in front of the southern boundary at all times, and the intensity of thickening in this area increases as n is increased. The maximum thickness after 15 m.y. of deformation in the southern boundary, increases from 54 km for $n = 1$ to 63 km for $n = 10$.

The choice of a fixed eastern boundary (boundary condition set 2), creates some differences in the gradients of crustal thickness in the eastern parts of the mesh. The effect is the formation of a thicker crust in the south, and a thinner crust in the north, since the northward transport of material is diminished compared to the case of free-slip boundary. As for the free boundary in the west, the westward escape of the material causes an overall reduction in crustal thickening, which at $t = 15$ m.y., is in the range of 3 km (for a Newtonian material).

3.2.1.2 Models with $Ar > 0$

The influence of Argand number on the deformation can be discussed in terms of two parameters, the effective viscosity of the lithosphere, and density contrast

between the crust and the mantle. When Argand number is small, there are two possibilities; either the viscosity of the medium is too high, in which case great amount of viscous forces will develop, or the density difference between the crust and the mantle is not large enough to build up sufficient amount of gravity forces during the process of isostatic compensation to overcome the viscous deformation. Very large Argand numbers on the other hand, imply that the lithosphere is too weak even to support modest gravity forces, or the buoyancy forces are so large that are capable of relaxing very high viscous flows. For a normal lithosphere where viscous and gravity forces are of the same order, the role of buoyancy forces is of considerable importance.

Velocity field

The effect of Argand number on the velocity field is to some extent overshadowed by the geometrical dimensions of the mesh. Regardless of the choice of Ar , the flow of material always reaches the northern edge of the mesh, and the profiles of the velocity are quite similar to those with zero Argand number. However some features are recognizable. Figure 3.8 shows the velocity fields for models with boundary condition sets 1 and 3, $n = 1$ and 3, and Argand values of 1, 3, 10 and 30. For larger Ar values, buoyancy forces become stronger in the medium and exert a driving force on the material towards the eastern parts, where the crust has not thickened significantly. The eastward rotation of velocity vectors for large Argand numbers is the result of this process. The effect of higher Argand numbers is most noticeable in the case of free-velocity boundary condition on the western side. As the strength of the lithosphere decreases, more material is diverted towards west and the rate of escape of material through the boundary increases (compare the area of the portion of the mesh to the left of the western boundary, for different values of Ar).

Figure 3.8 Velocity fields for homogeneous models with $Ar > 0$ at $t = 15$ m.y. **(a)-(d)** models with boundary condition set 1 and non-Newtonian material ($n = 3$), **(a)** $Ar = 1$, **(b)** $Ar = 3$, **(c)** $Ar = 10$, **(d)** $Ar = 30$, **(e)** boundary condition set 3, $n = 1$, $Ar = 3$, **(f)** boundary condition set 3, $n = 1$, $Ar = 10$. The velocity vector at southern boundary is equal to 4 cm y^{-1} .

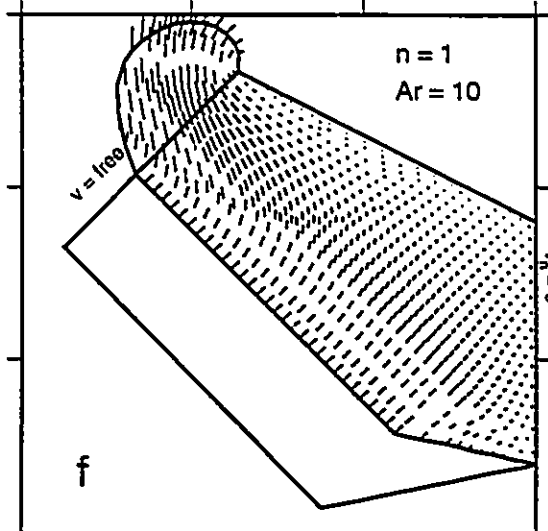
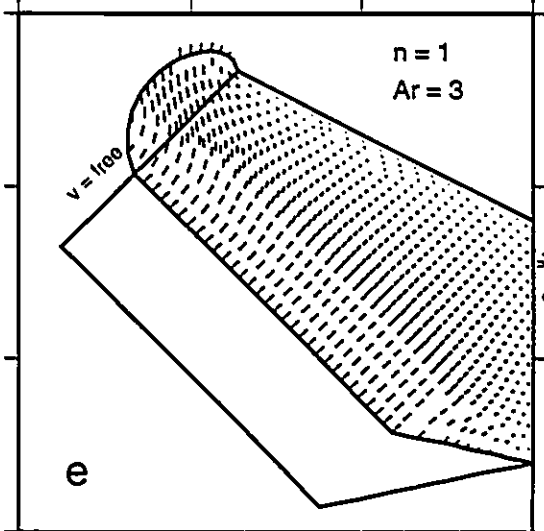
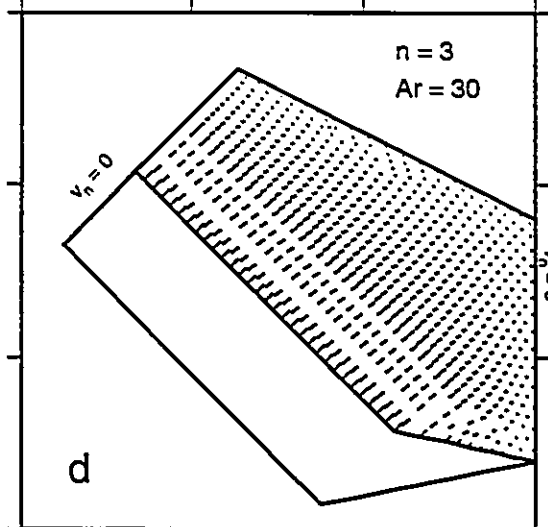
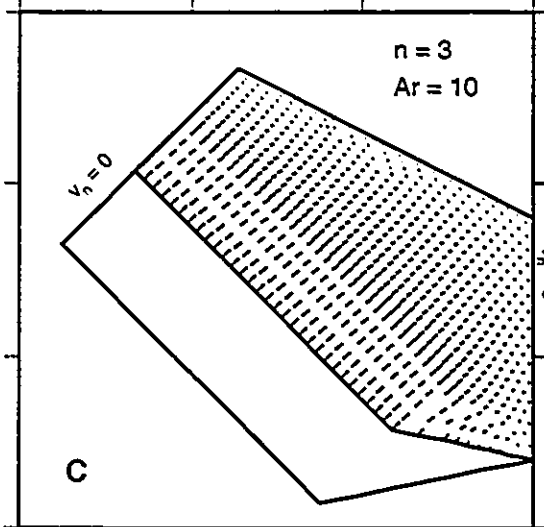
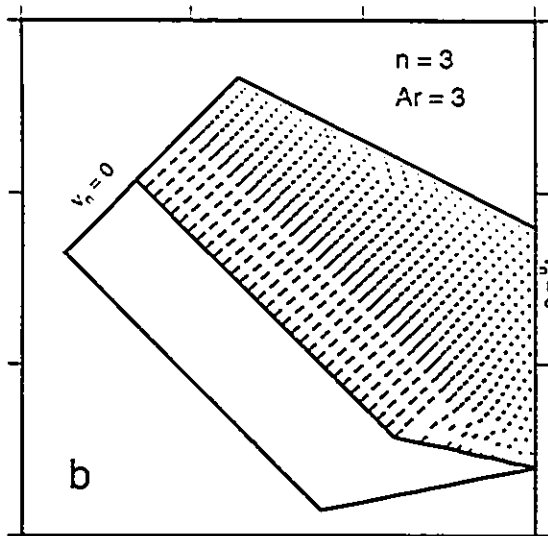
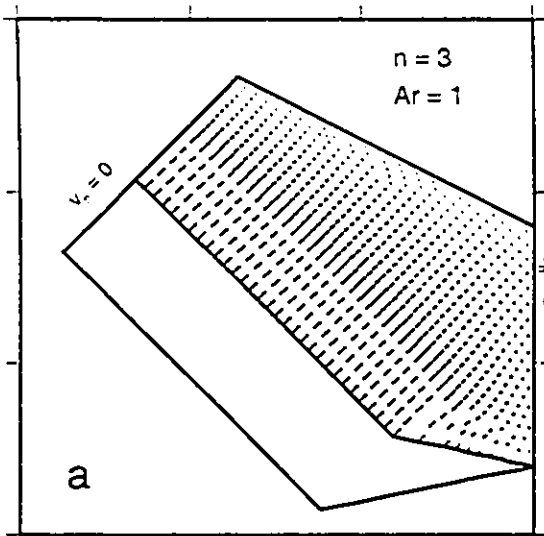
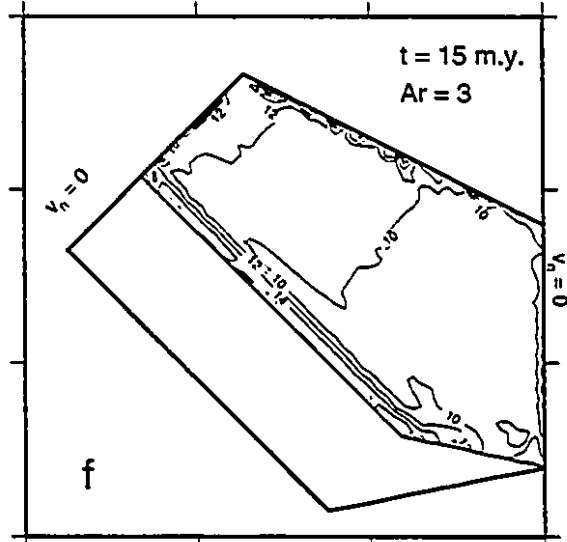
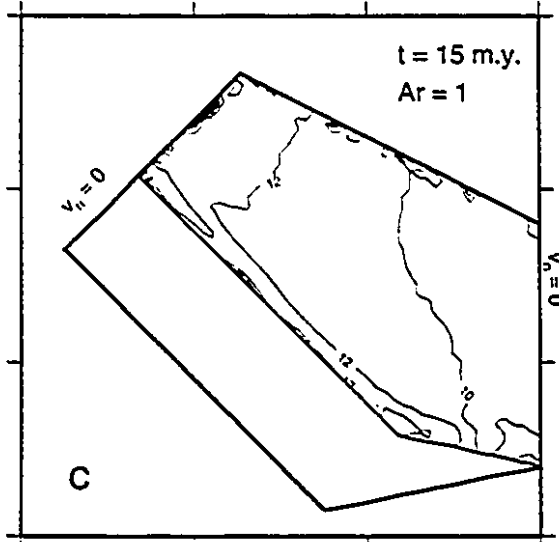
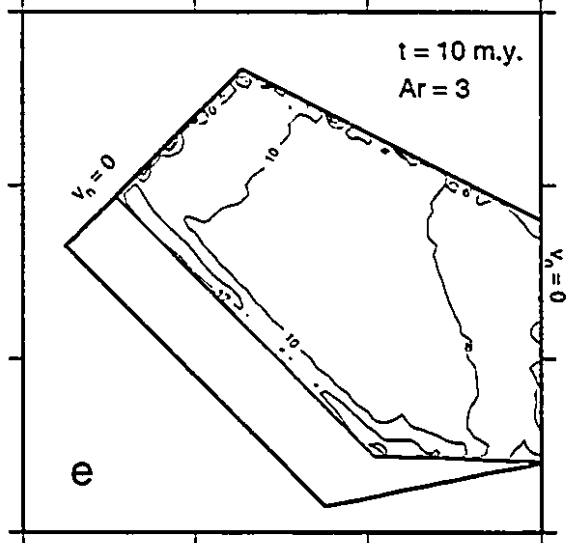
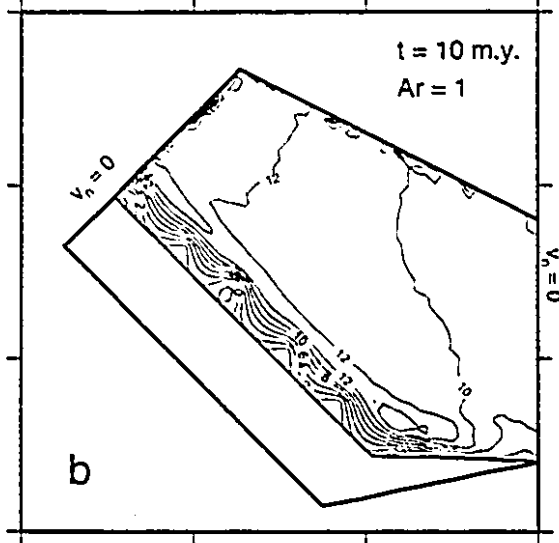
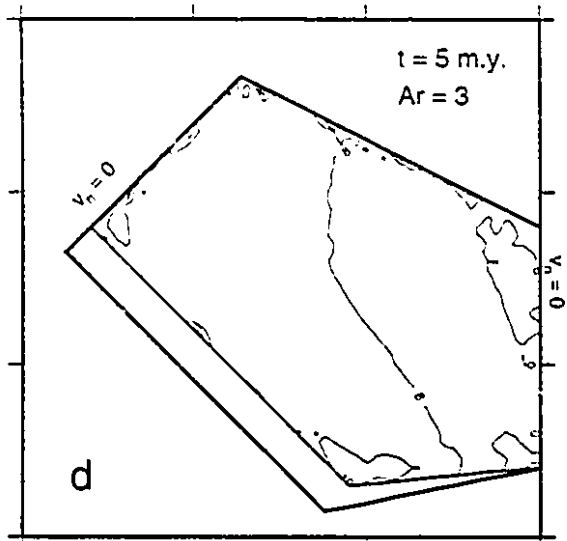
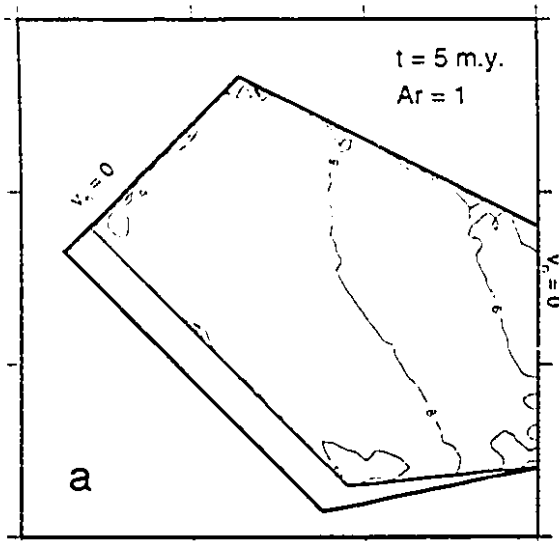
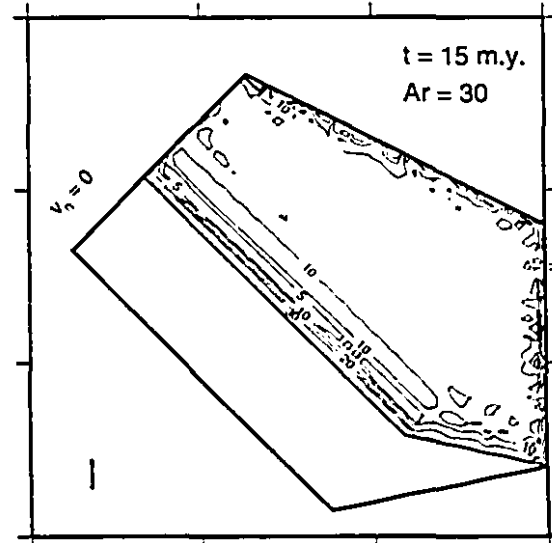
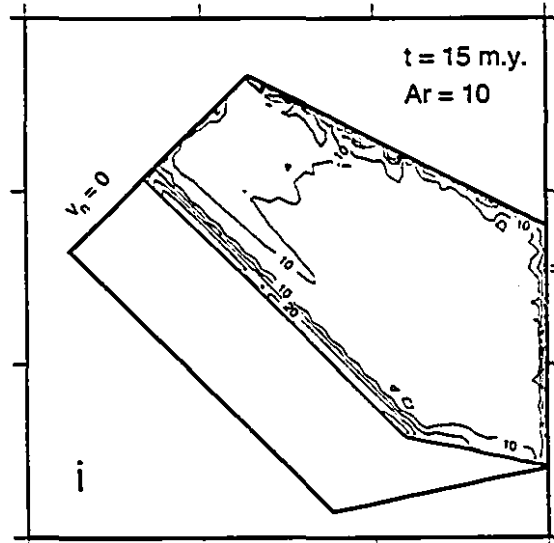
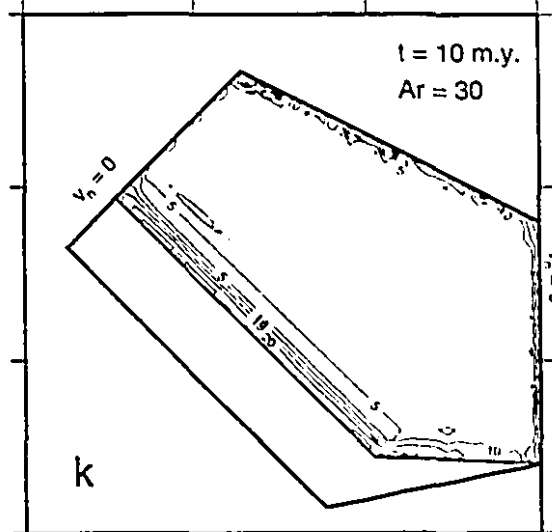
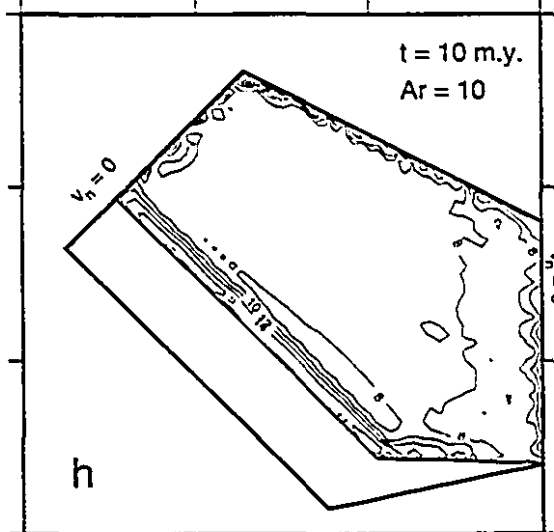
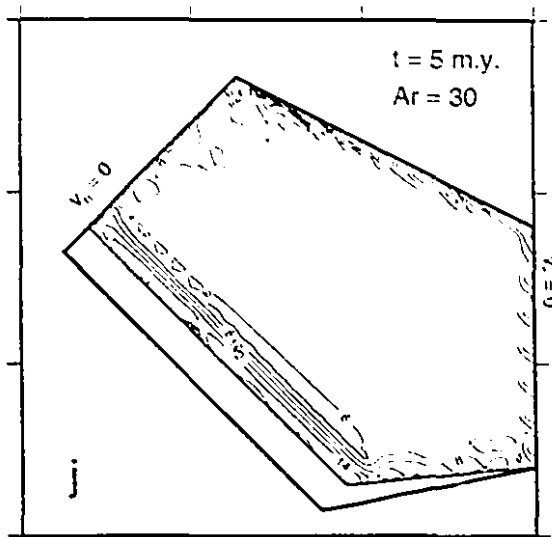
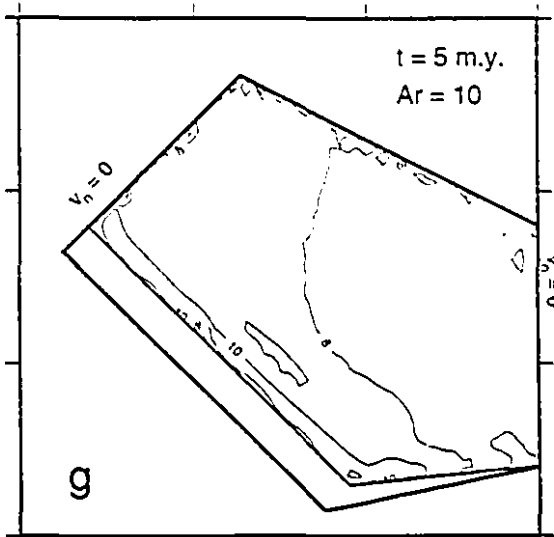


Figure 3.9 Time evolution of the vertical strain rates at time intervals of 5 m.y. for homogeneous models with boundary condition set 1 and $n = 3$ and different Ar values, (a)-(c) $Ar = 1$, (d)-(f) $Ar = 3$, (g)-(i) $Ar = 10$, (j)-(l) $Ar = 30$. Contours are in units of $10^{-16}s^{-1}$. In (l), a zone of negative strain rate develops inside the contour 5×10^{-16} . It is not shown here since the rate of crustal thinning is one order of magnitude smaller than that of crustal thickening.





Strain rate fields

The patterns of vertical strain rates are similar to those described in the previous section for $Ar = 0$. However as Ar is increased gravity forces introduce some differences. In Figure 3.9 the time evolution of vertical strain rates for models with boundary condition set 1, $n = 3$ and $Ar = 1, 3, 10,$ and 30 is presented. In all cases vertical strain rates tend to localize in front of the southern boundary, and there seems to be no limit on the thickening of crust as time proceeds. However as Ar is increased, an elongated zone with smaller rate of thickening is produced parallel to the advancing boundary. For $Ar = 30$ and at $t = 15$ m.y., the rate of thickening in this zone becomes negative, and an area of net extension develops. As a result, a trough-like structure with a thinner crust is produced towards the end of deformation. The effect of increase in the strength of buoyancy forces for large Argand numbers is also seen in the northwest-southeast gradient of vertical strain rates. As Argand number is increased, the lithosphere becomes less capable of supporting great crustal thicknesses in the western side of the mesh, and vertical deformation expands towards eastern parts, resulting in more uniform crustal thickening inside the mesh.

The effect of Argand number on the shear strain rate has been studied, and the results of some of the experiments are shown in Figure 3.10. As Ar is increased from 1 to 30, the lower viscosity of the medium allows more material to move inside the mesh. This will result in a progressive increase in the gradient of velocity vectors normal to the influx direction. Consequently, greater shear zones will develop on the southern part of the mesh. The strain rate fields have been calculated for other values of n (1, 5 and 10). They are not presented here since they lead to similar conclusions. The effects of different boundary conditions also, resemble those discussed in the previous section.

Figure 3.10 Shear strain rates at $t = 15$ m.y., for homogeneous models with boundary condition set 1 and $n = 3$. (a) $Ar = 1$. (b) $Ar = 3$. (c) $Ar = 10$. (d) $Ar = 30$. Contours are in units of 10^{-16}s^{-1} .

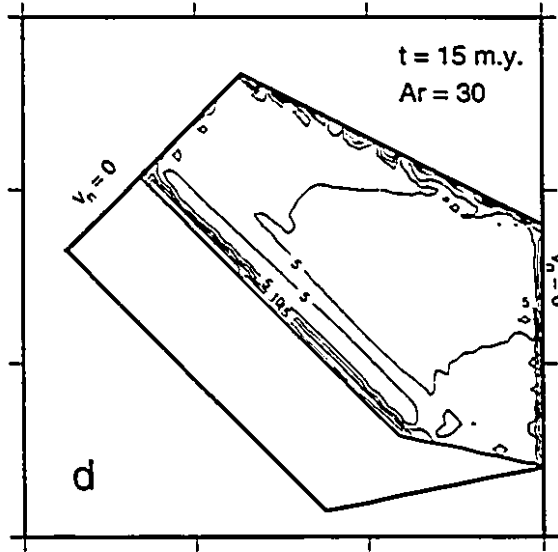
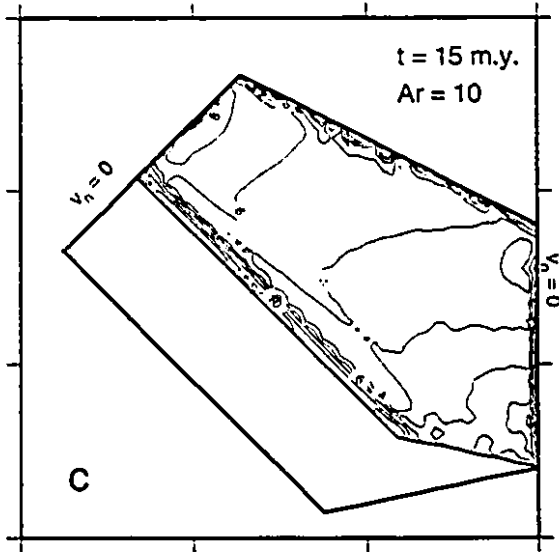
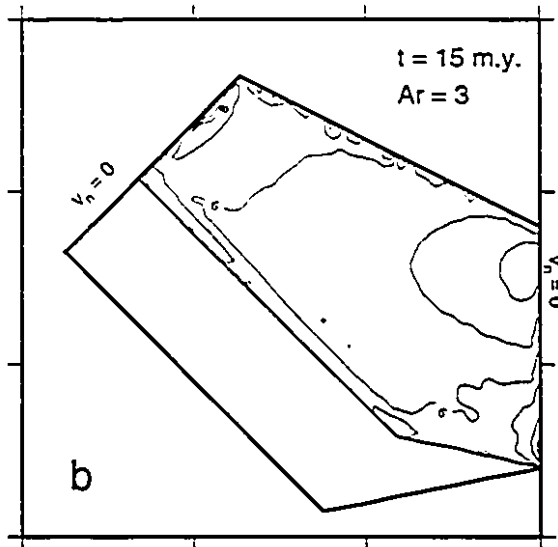
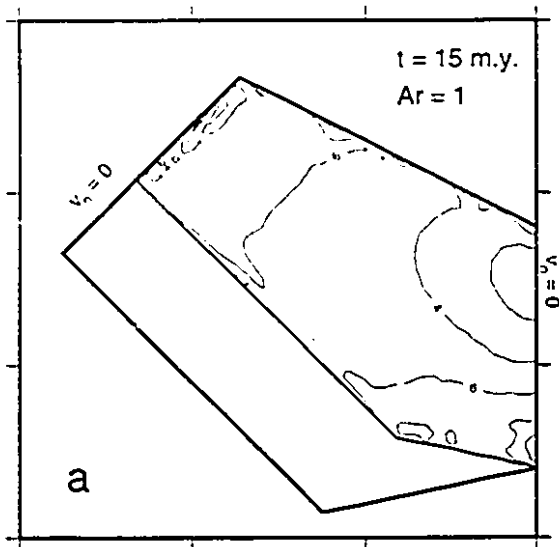
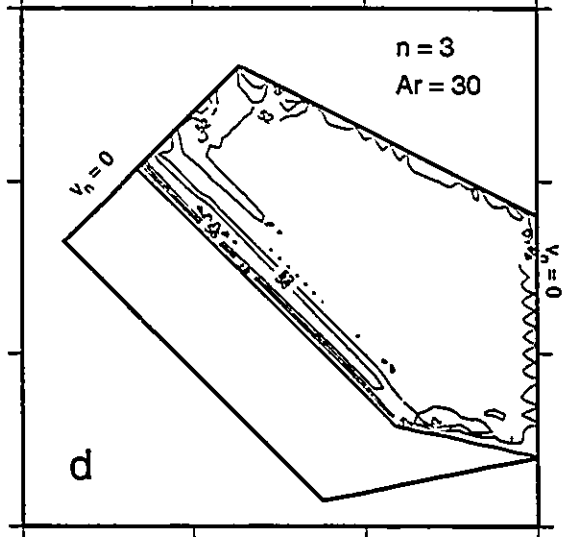
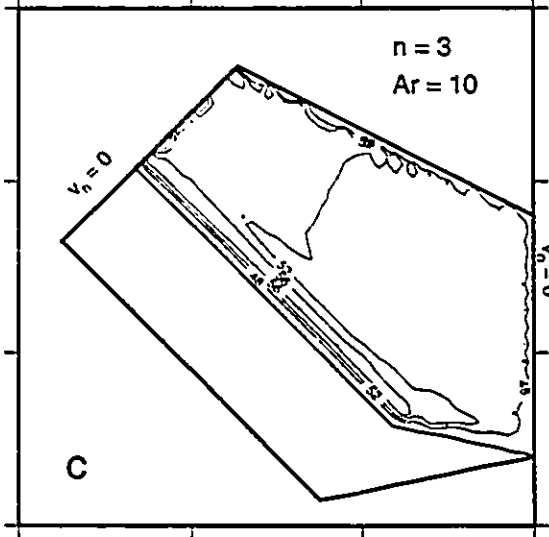
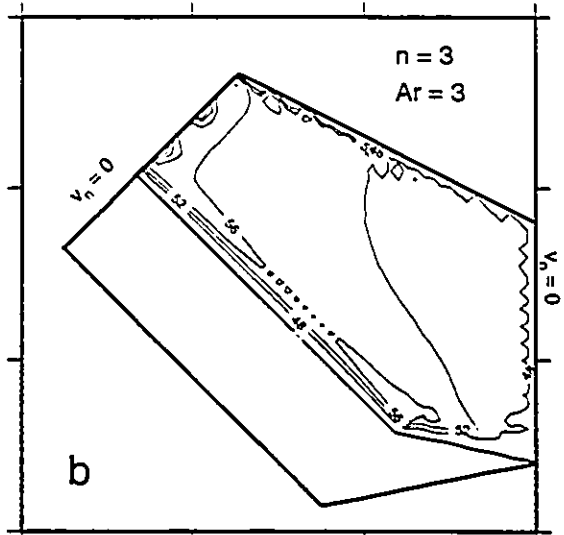
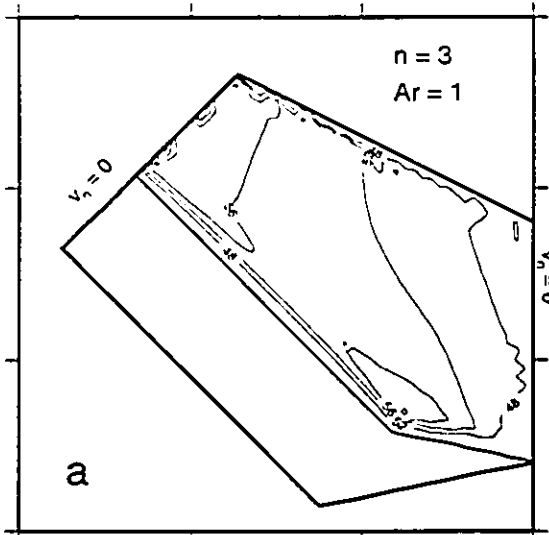
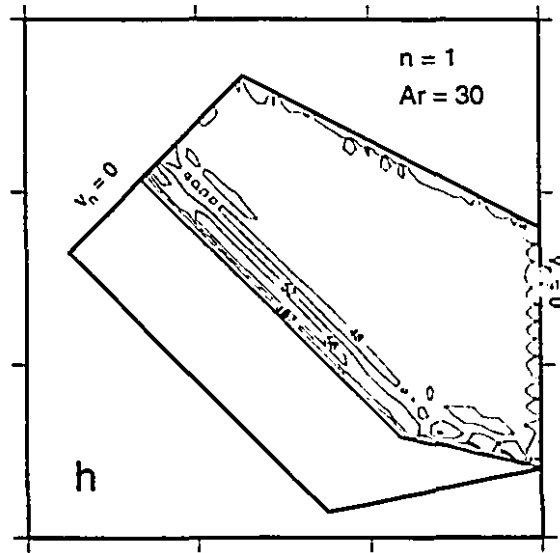
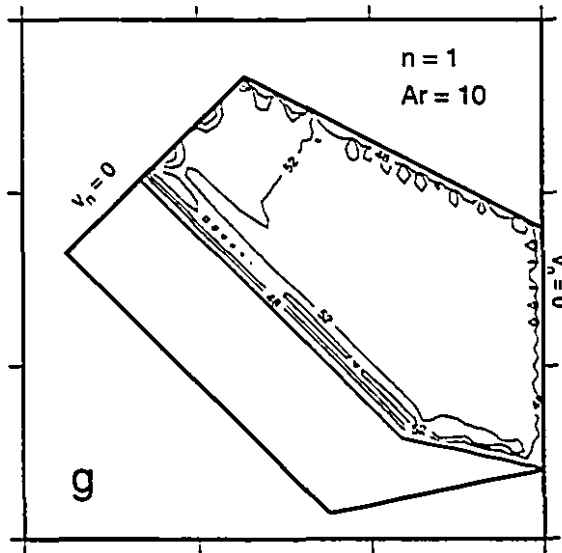
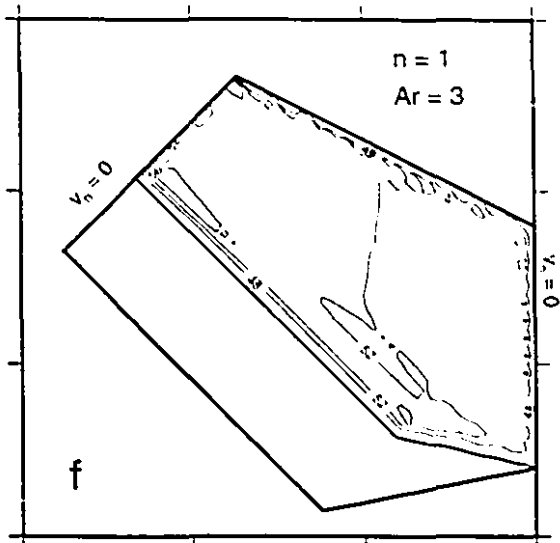
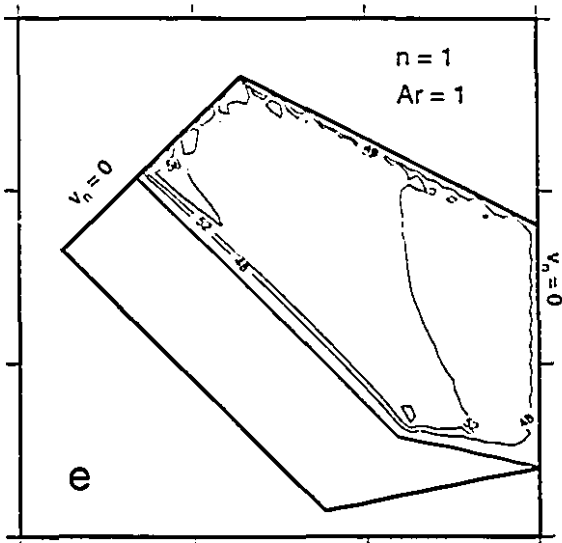


Figure 3.11 Crustal thickness distributions at $t = 15$ m.y., in homogeneous models with $Ar > 0$ and boundary condition set 1. (a)-(d) non-Newtonian material with $n = 3$, (a) $Ar = 1$, (b) $Ar = 3$, (c) $Ar = 10$, (d) $Ar = 30$, (e)-(h) Newtonian material, (e) $Ar = 1$, (f) $Ar = 3$, (g) $Ar = 10$, (h) $Ar = 30$. Contours are in units of 1 km.





Crustal thickness

Figure 3.11 shows the crustal thickness distribution for different rheologies and different Argand numbers at $t = 15$ m.y. As the strength of the lithosphere is decreased (larger Ar values) the gradients of the thickness in the eastern direction diminish (compare the results with those with zero Argand number, where substantial thickness variations exist in this direction). This is best visible in the case of Newtonian material, where the flow has greater tendency to extend into the interior of the mesh.

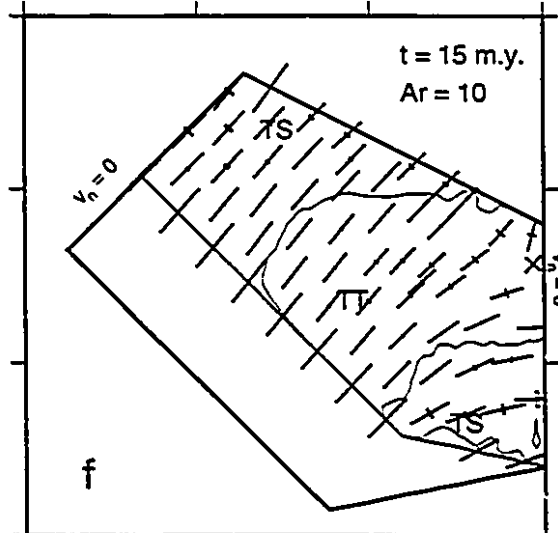
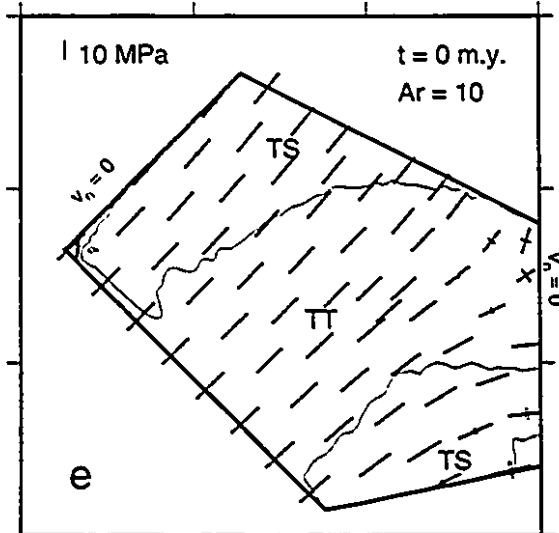
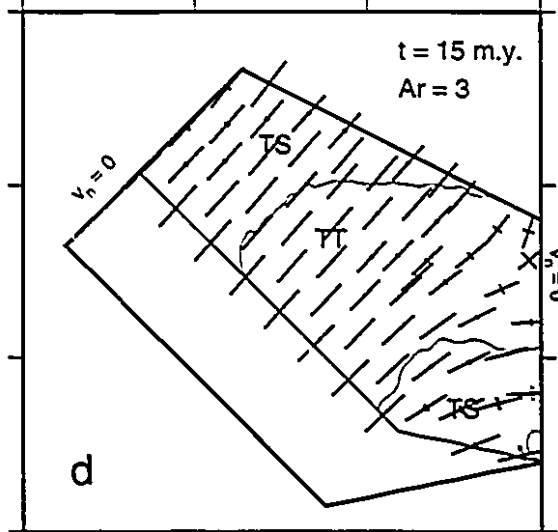
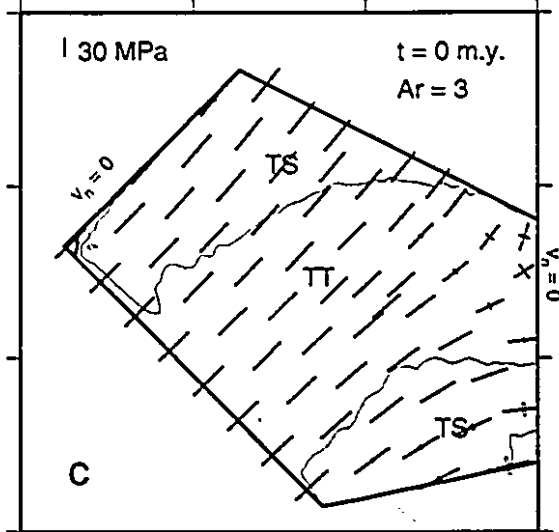
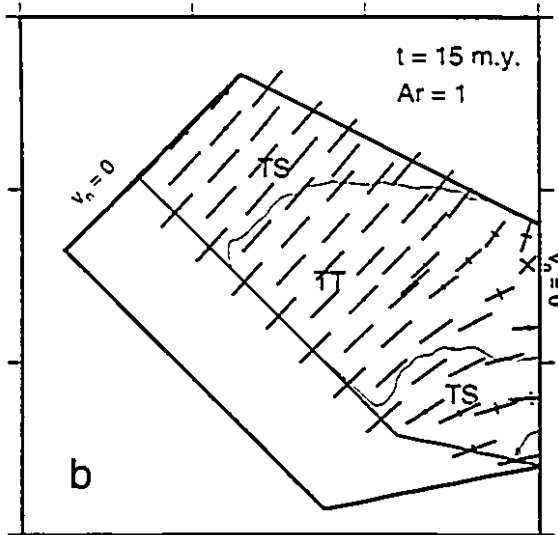
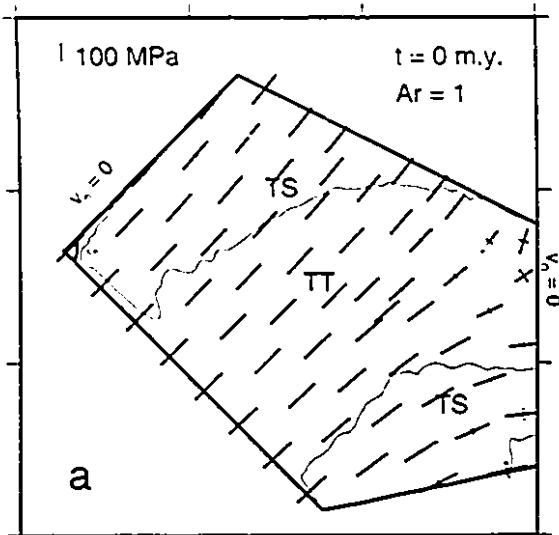
For large Argand numbers the crustal thickness immediately in front of the southern boundary, shows rather large values, which is not expected. This is probably due to the choice of fixed crustal thickness boundary condition which leads to large gradients near the boundary (England & McKenzie 1982).

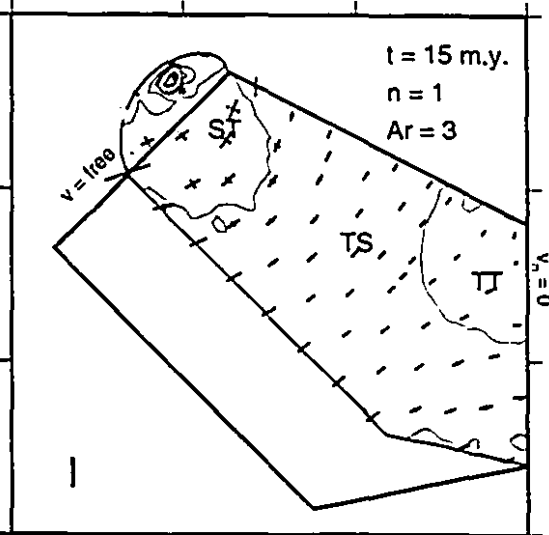
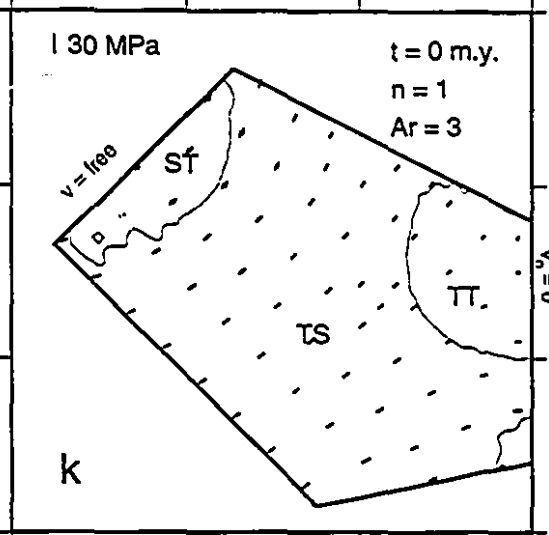
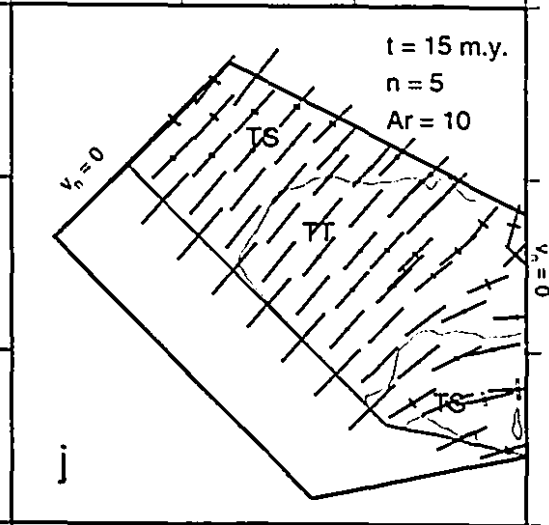
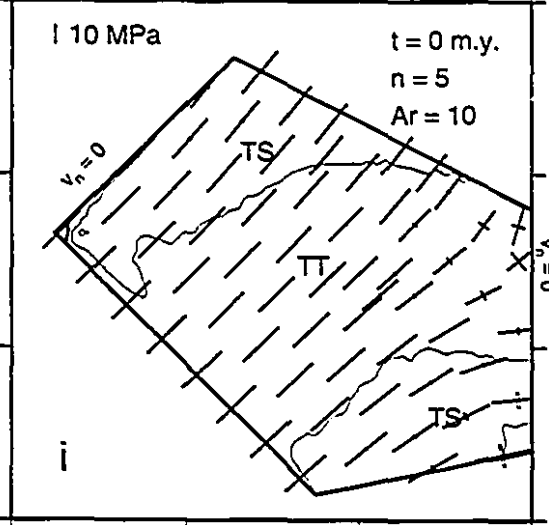
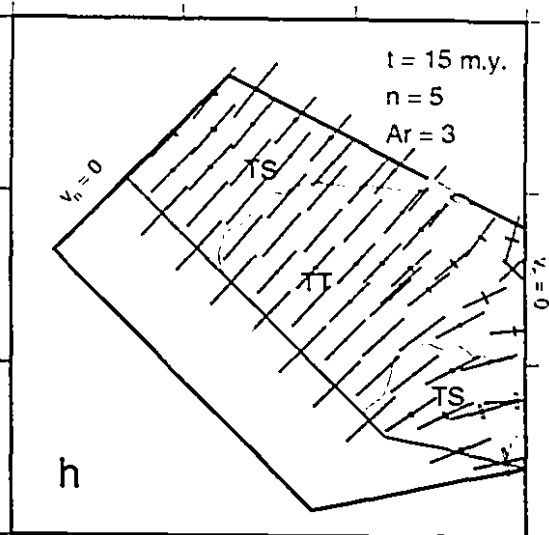
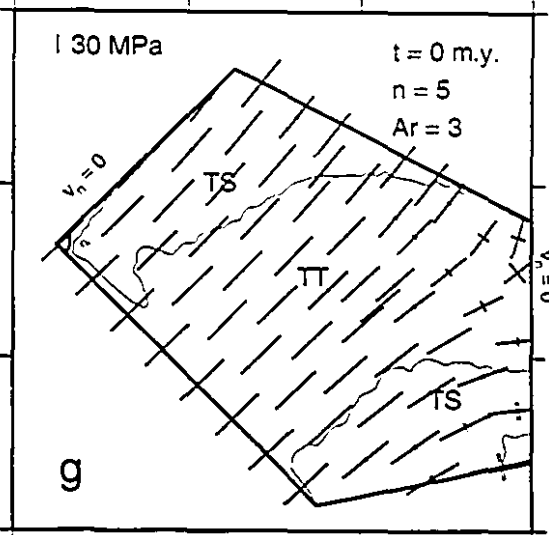
Stress fields and style of faulting

The stress field can be used to assess the style of faulting in the deforming mesh. It is assumed here that two of the principal stresses always lie on the horizontal plane. Although the calculated stress field, prevails in the strongest part of lithosphere where the velocity field is continuous, as mentioned in the previous chapter, it is accepted that there are sufficient number of randomly distributed preexisting faults in the upper crust. Therefore the response of the brittle crust to the underlying continuous stress field is isotropic (McKenzie & Jackson 1983, Houseman & England 1986).

The horizontal principal deviatoric stresses for $n = 3$ and 5 , and $Ar = 1, 3$, and 10 , calculated at $t = 0$ and $t = 15$ m.y. and for boundary condition set 1 are illustrated in Figure 3.12. The magnitude of the stress field for a fixed Argand number increases as the nonlinearity of the flow increases. For example, the maximum compressional

Figure 3.12 Plots of the principal horizontal deviatoric stress axes, at $t = 0$ and $t = 15$ m.y. for homogeneous models with boundary condition sets 1 and 3. Thick lines correspond to tensional stress, and thinner lines to compressional stress. The small bars on the upper right corner of the boxes are the scales of the magnitudes of the stresses. Superimposed on the plots are the contours of the quantity $\tan^{-1}(\dot{\epsilon}_2/\dot{\epsilon}_1)$ separating areas of different styles of faulting, where $\dot{\epsilon}_2$ and $\dot{\epsilon}_1$ are the principal horizontal strain rates. TT refers to thrust faulting on planes striking parallel to each principal axis, TS, thrust faulting striking perpendicular to the major principal axis with minor strike slip faulting, ST, strike slip faulting with minor thrusting. A full discussion of calculation of styles of faulting is given in Houseman & England (1986). (a)-(f) models with boundary condition set 1 and $n = 3$, (a) $t = 0$, $Ar = 1$, (b) $t = 15$ m.y., $Ar = 1$, (c) $t = 0$, $Ar = 3$, (d) $t = 15$ m.y., $Ar = 3$, (e) $t = 0$, $Ar = 10$, (f) $t = 15$ m.y., $Ar = 10$, (g)-(j) models with boundary condition 1 and $n = 5$, (g) $t = 0$, $Ar = 3$, (h) $t = 15$ m.y., $Ar = 3$, (i) $t = 0$, $Ar = 10$, (j) $t = 15$ m.y., $Ar = 10$, (k)-(l) model with boundary condition set 3 and Newtonian material, (k) $t = 0$, $Ar = 3$, (l) $t = 15$ m.y., $Ar = 3$.





stress at $t = 15$ m.y. for models with $Ar = 1$ increases from 50 MPa for $n = 1$, to 120 MPa for $n = 3$, and to 155 MPa for $n = 5$. This is expected since for highly nonlinear materials viscosity strongly depends on the strain rate. The magnitude of the stress for a fixed power law rheology decreases as Argand number increases (i.e. effective viscosity decreases). For example, the maximum compressional stress at $t = 15$ m.y. for models with $n = 3$, decreases from 120 MPa for $Ar = 1$ to 40 MPa for $Ar = 3$, and to 10 MPa for $Ar = 10$.

The major principal deviatoric stress is always compressional and oriented along the direction of flow. It has a monotonic gradient towards the northeastern corner of the mesh. The minor principal deviatoric stress, however, has magnitudes far less than those of the major principal stress (most of the time at least one order of magnitude) and shows more complicated patterns. Several distinctive regions in the stress field are recognizable. In the western part of the mesh, the minor principal stress is tensional and the tension as well as compression increases as the deformation proceeds. In front of the southern boundary in the center, a state of uniaxial contraction or isotropic contraction endures. Tensional stress does not develop in this region unless the lithosphere is too weak ($Ar > 10$). Further to the east, again a tensional field in the northwest-southeast direction develops as a consequence of large velocity gradients in the eastern direction. From center of the mesh towards the northeastern corner, both principal stresses become compressional, with a gradual increase in the magnitude of the minor principal stress relative to that of the major principal stress. The development of contraction regime in this part is because of the convergence of the velocity field towards the northeast.

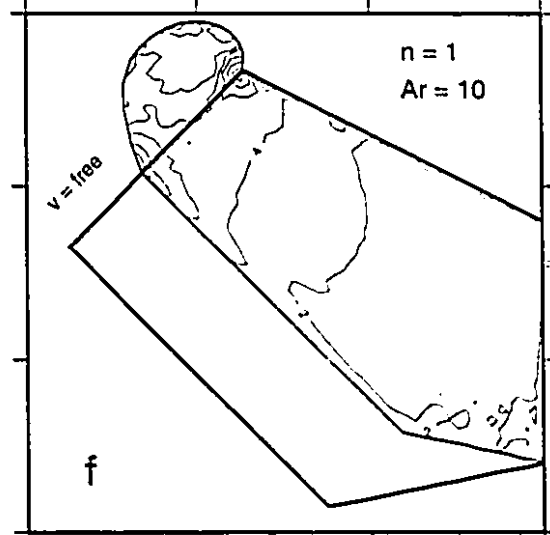
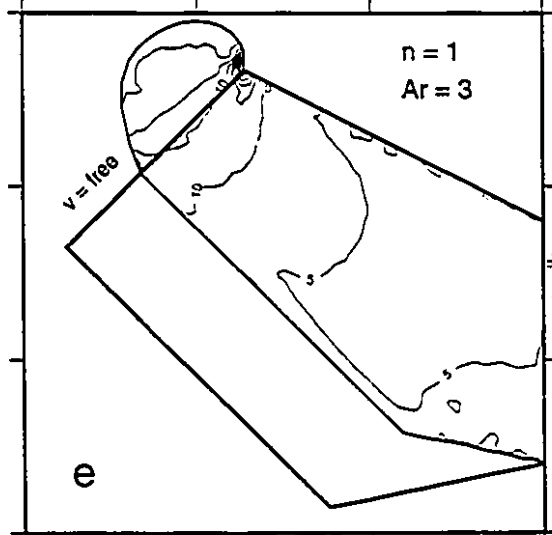
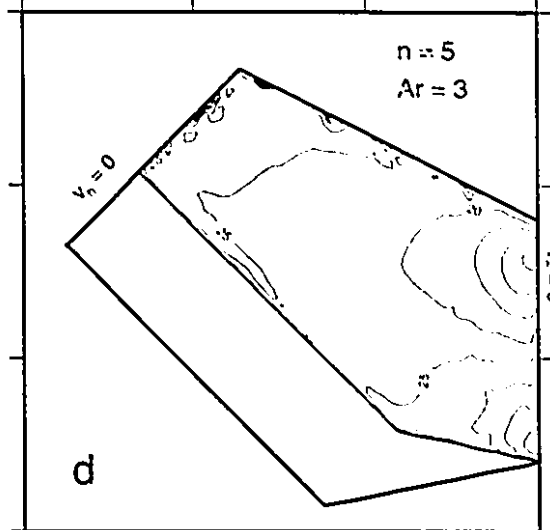
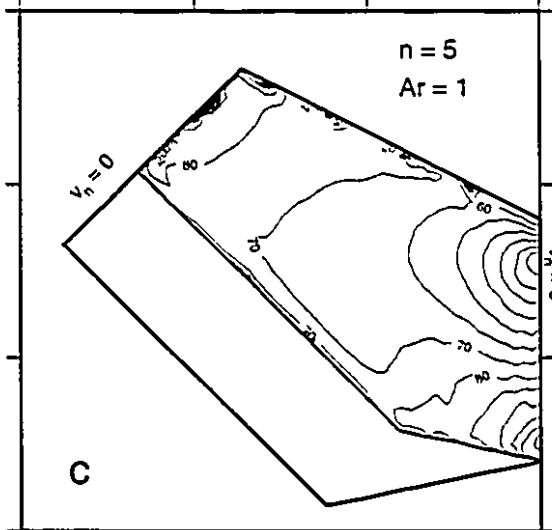
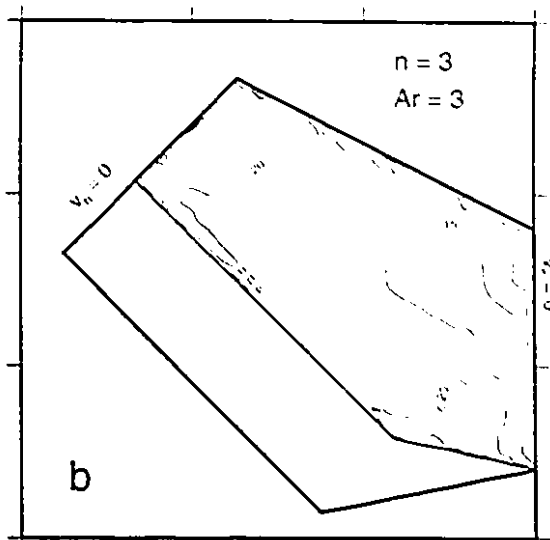
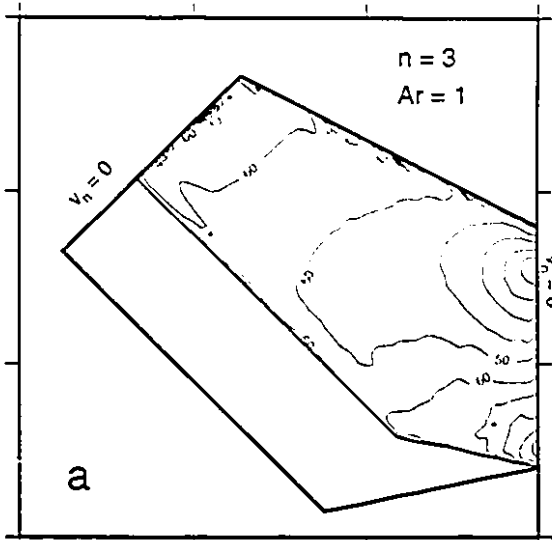
Based on the stress field described above, and relative magnitudes of the principal horizontal strain rates, the deformation in the mesh can be divided into three distinct regions regarding the styles of faulting. In Figure 3.12 the contour lines

separating the areas of different types of faulting are superimposed on the stress fields. Each of the symbols on the plots refers to a different region of discontinuous deformation: 1) in the west and northwest, deformation is accomplished mainly by thrust faulting on planes striking in northwest-southeast direction, accompanied by some minor strike-slip faulting (style TS). 2) in the south, center and northeast, thrust faulting in planes parallel to both principal axes (style TT) takes up the entire crustal thickening. In the case of very weak lithosphere where lateral components of flow are of relative importance, some strike-slip motion exerted by buoyancy forces, occurs in the direction normal to the flow, and 3) in the southeast the motion is taken up along the predominant thrust faulting in east-northeast direction along with some strike-slip motion parallel to the thrust faults (style TS). The amount of strike-slip motion in this part is at the maximum in the mesh.

The styles of faulting are also inferred from the variations of the maximum shear stress. The greatest shear zones are localized in the western and southeastern parts of the mesh (Figure 3.13), where principal stresses are of opposite signs. For very stiff lithosphere ($n = 5$ and $Ar = 1$), shear stress can reach to as much as 100 MPa. For very weak lithosphere ($n = 1$ and $Ar = 30$) it is of the order of 1 MPa.

With the boundary condition set 3, the state of stress dramatically changes. In this case while the major horizontal principal stress is still compressional in the direction of shortening, pure compression is confined to a small region in the northeast, and tension along the minor principal axis dominates the western and southern parts of the mesh. This leads to an enhancement of the strike-slip component of deformation, especially in the west, and shearing becomes more important in front of the southern boundary. The extension in the west can reach up to one third of compression in magnitude.

Figure 3.13 Maximum shear stresses at $t = 15$ m.y. in homogeneous models. **(a)-(d)** models with boundary condition set 1 and non-Newtonian materials: **(a)** $n = 3$, $Ar = 1$. **(b)** $n = 3$, $Ar = 3$. **(c)** $n = 5$, $Ar = 1$. **(d)** $n = 5$, $Ar = 3$. **(e)-(f)** boundary condition set 3 and Newtonian material: **(e)** $n = 1$, $Ar = 3$. **(f)** $n = 1$, $Ar = 10$. Contours are in units of 1 MPa.



3.2.2 Heterogeneous models

In this section the effects of two heterogeneous inclusions shown in Figure 3.1, are discussed. The inclusions are defined by assigning a greater value of effective viscosity to them, compared to that of the surroundings. The results show that, even a strength contrast of factor of 2, has profound effects on the stress and strain rate fields. In the following, models with one inclusion (i.e. central Iran) as well as two inclusions are presented. It should be mentioned that the Caspian inclusion is considered fixed to the northern boundary. Otherwise the presence of a narrow zone of deformation between the inclusion and boundary, leads to a huge gradient of crustal thickness which ultimately causes numerical instability.

Velocity field

Figure 3.14 shows the velocity field and the final geometries of the two inclusions for models with $n = 3$, and different Argand numbers and rheology contrasts. It is easily seen that although the rheology contrast is not very high, the inclusions deform almost like a rigid body and the gradient of velocity inside them is very minute. While the corresponding regions in the homogeneous models (Figure 3.8) experience shear deformation and larger gradient of velocity.

Strain rate fields and crustal thickness

The presence of the heterogeneities significantly changes the patterns of the rate of thickening. The main feature is that crustal thickening is inhibited within the strong regions, whereas it is enhanced in the other parts. Figures 3.15 and 3.16 show the

Figure 3.14 Velocity fields at $t = 15$ m.y. for heterogeneous models with boundary condition set 1 and a non-Newtonian material ($n = 3$): (a) $Ar = 3$, $R = 2$. (b) $Ar = 3$, $R = 5$. (c) $Ar = 10$, $R = 2$. (d) $Ar = 10$, $R = 5$. The final shapes of the inclusions are shown in the figures.

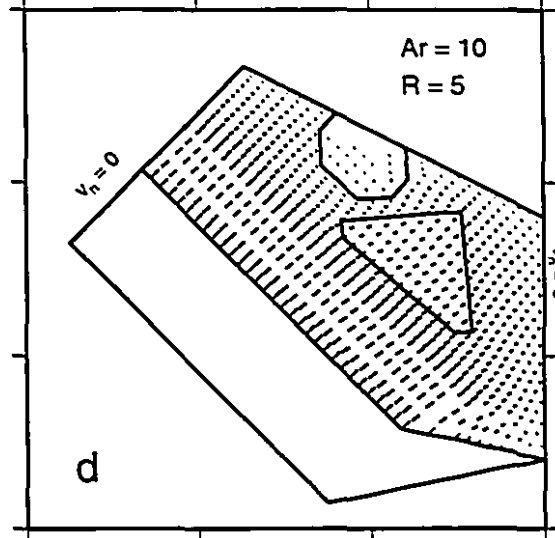
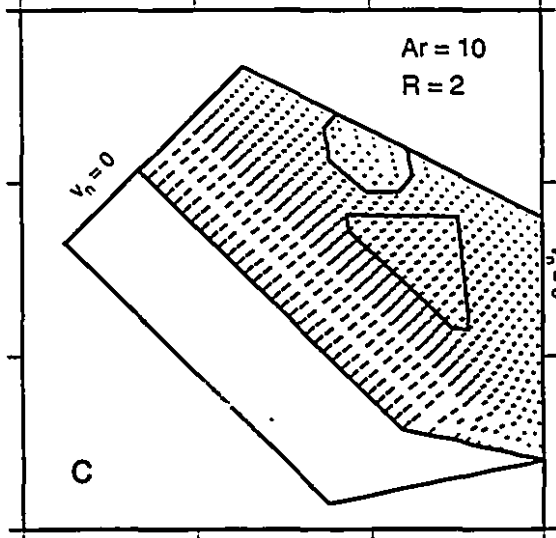
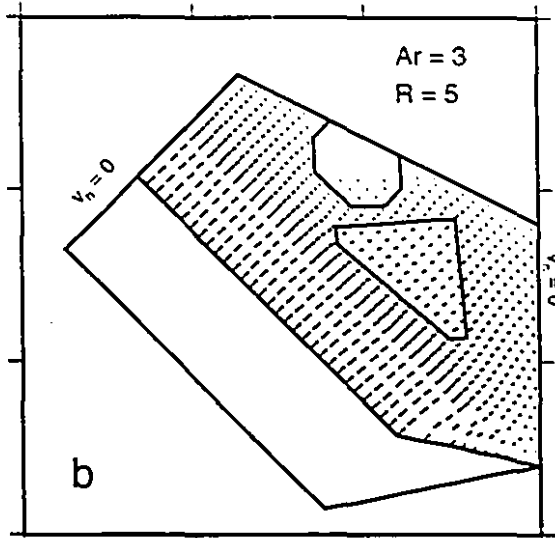
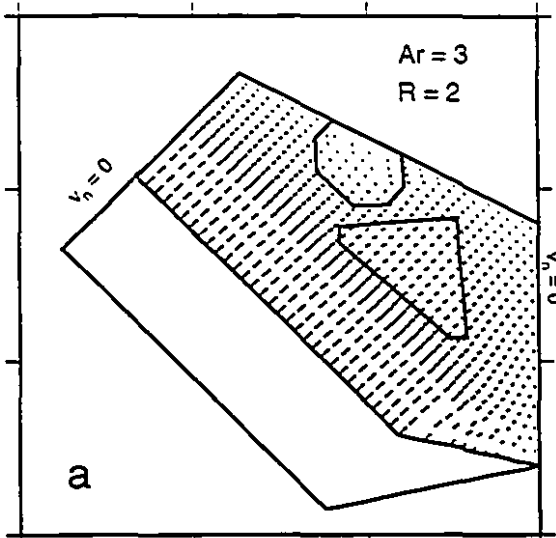


Figure 3.15 Vertical strain rates at $t = 15$ m.y., for heterogeneous models with boundary condition set 1 and $Ar = 3$: (a) $n = 3, R = 2$, (b) $n = 3, R = 5$, (c) a one-inclusion (central Iran) model with $n = 3, R = 2$, (d) a one-inclusion model with $n = 3, R = 5$, (e) $n = 5, R = 2$, (f) $n = 5, R = 5$. The contours are in units of $10^{-16} s^{-1}$.

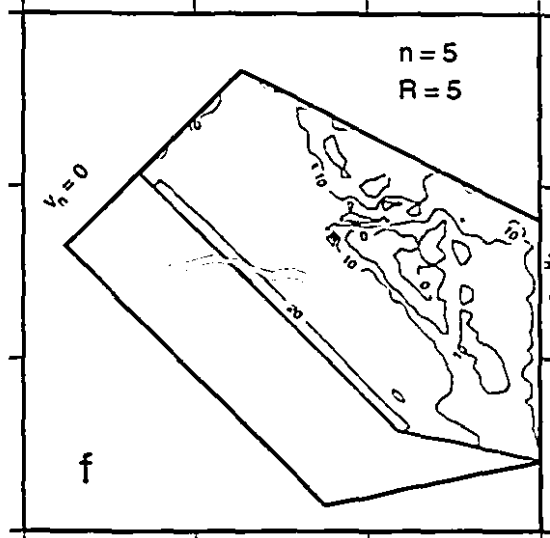
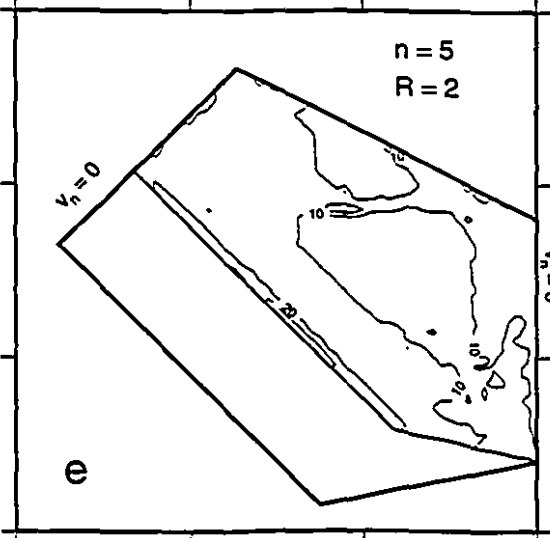
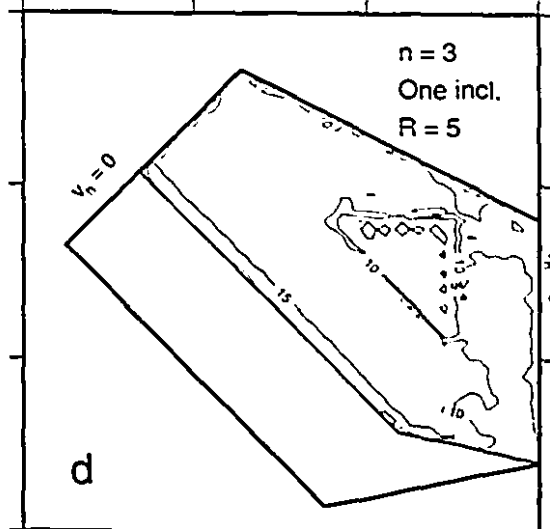
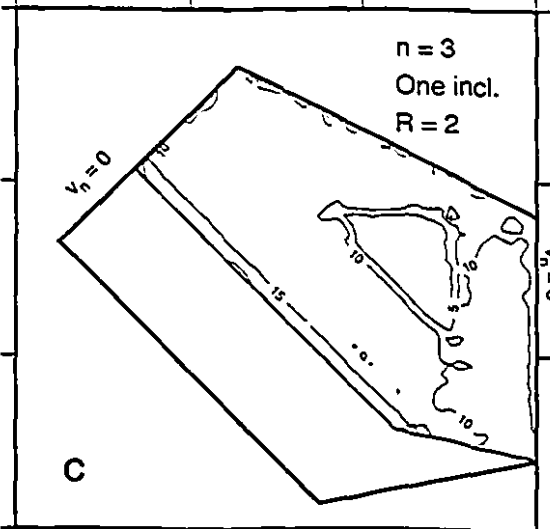
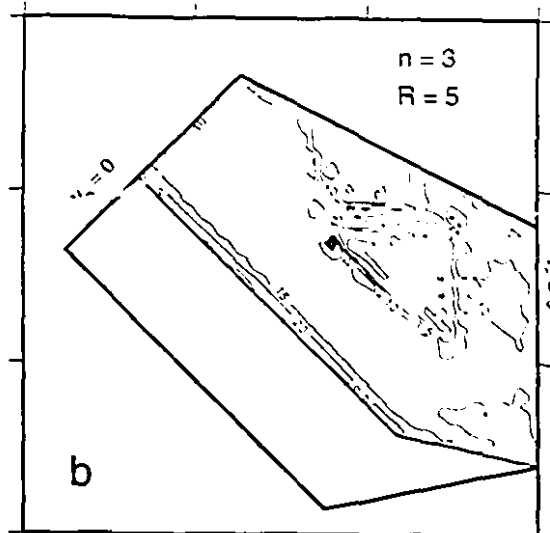
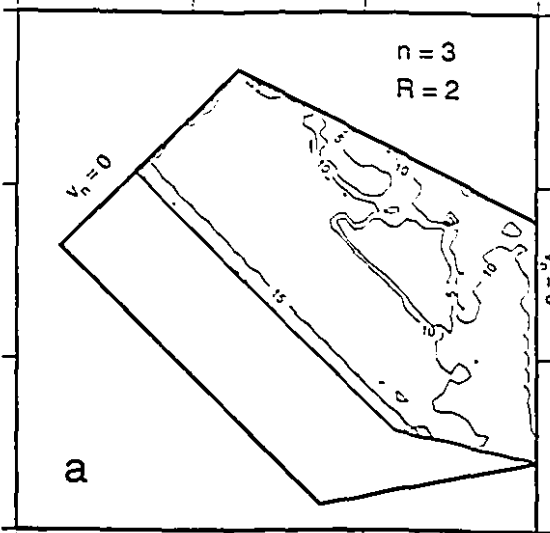
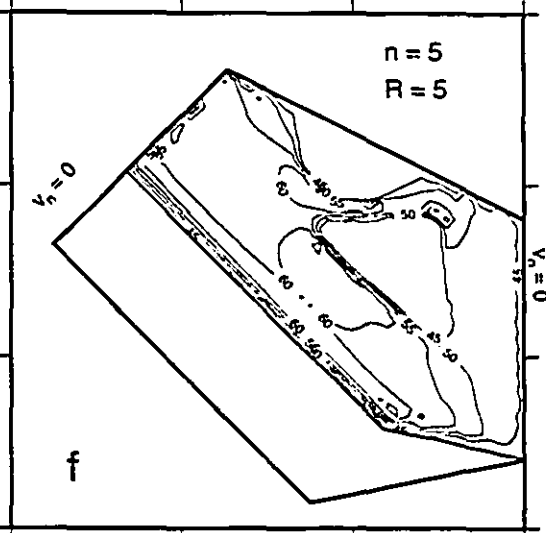
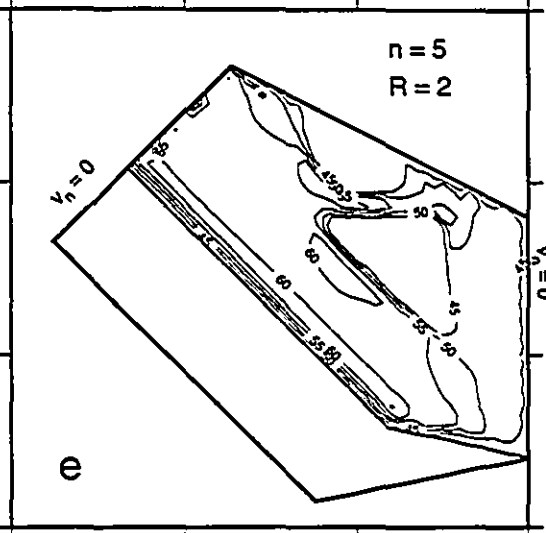
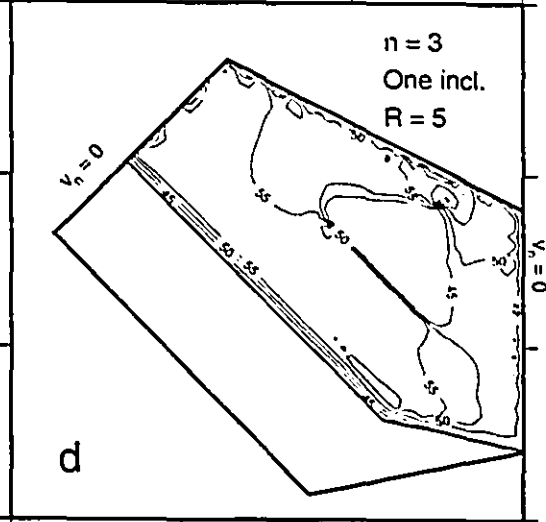
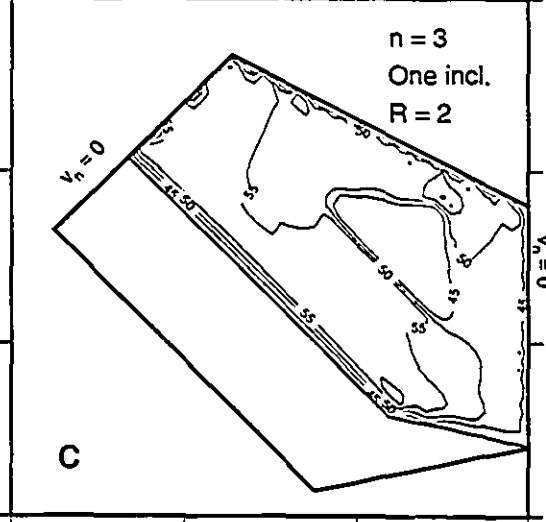
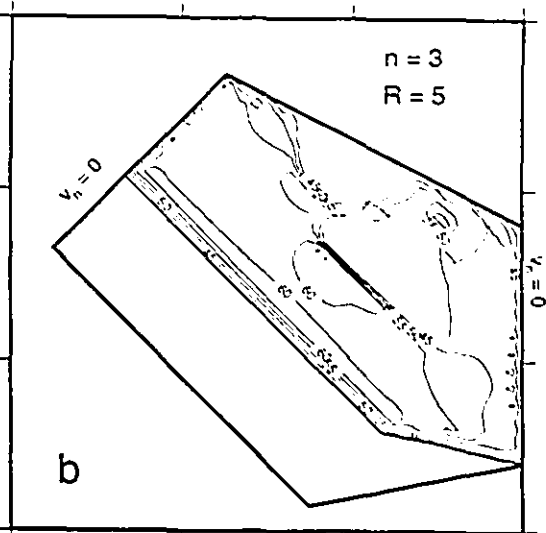
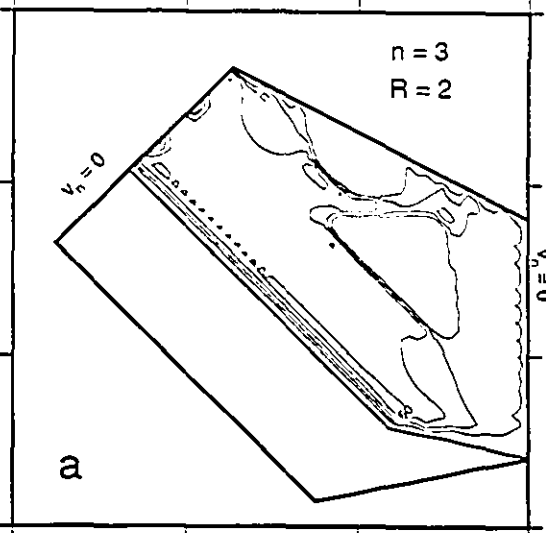


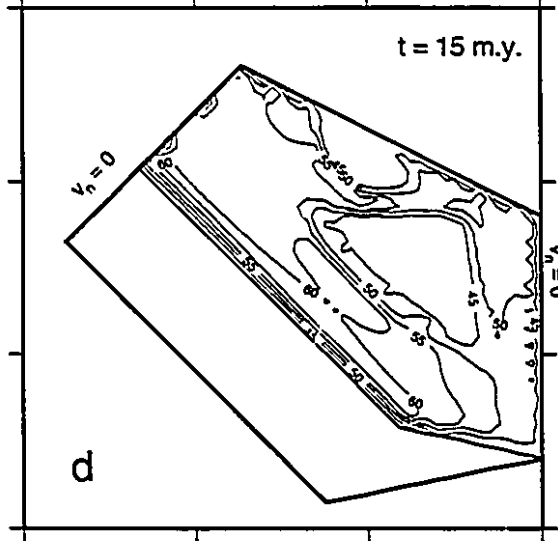
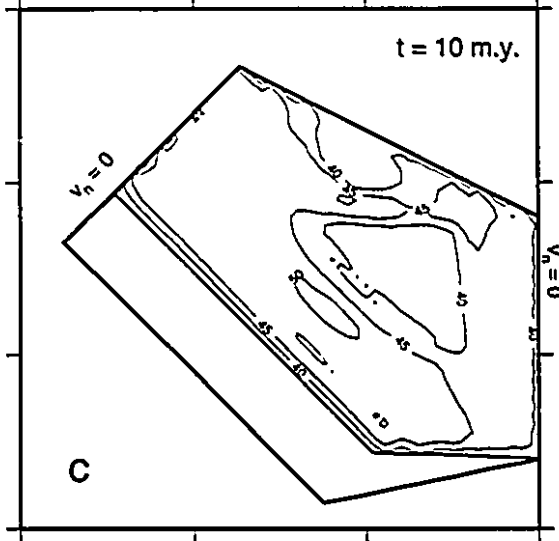
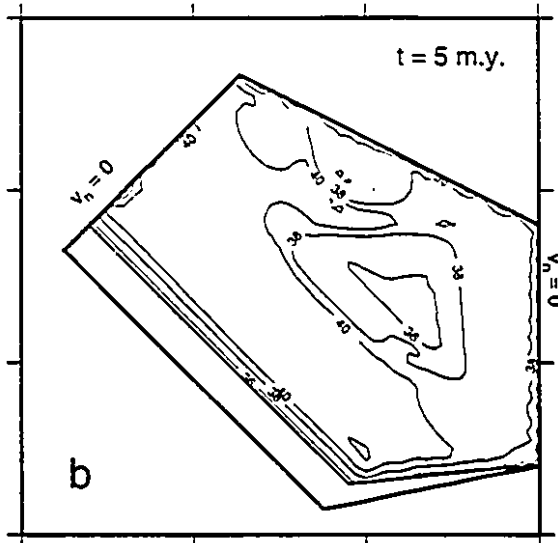
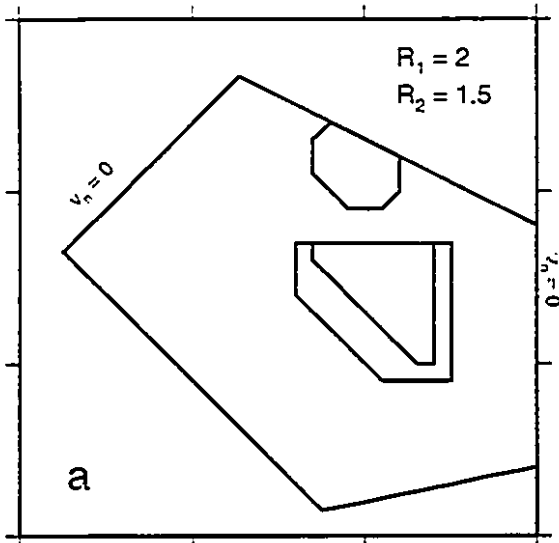
Figure 3.16 Crustal thickness distributions at $t = 15$ m.y. for heterogeneous models. All the parameters are as same as those in Figure 3.15. Contours are in units of 1 km.



vertical strain rate and crustal thickness of three heterogeneous experiments with $n = 3$, $Ar = 3$ and $R = 2, 5$. A comparison of these figures with those of a corresponding homogeneous model (Figures 3.9 and 3.11) indicates that in addition to the area of intense thickening in the southern boundary, vertical deformation is significantly increased in the region between the two inclusions, while there is much less thickening inside the inclusions. Maximum crustal thickening in front of the southern boundary for $R = 5$ reaches up to 75% and for $R = 2$ to 68%, the thickening of the homogeneous model never exceeds 60%. In the region between the inclusions, the total thickening is now 15% more than that of a homogeneous model. In the innermost parts of the inclusions, the initial thickness, even after 15 m.y. of deformation, is retained (in cases of highly nonlinear materials or very stiff inclusions, the inclusions may even experience some slight crustal thinning). In the one-inclusion models (Figure 3.16c and 3.16d), the second region of intense vertical deformation to the northeast of the inclusion, is still noticeable. The intense thickening in this region, is partly due to the discrete nature of the finite elements at the corner of the inclusion. The development of crustal thickening beyond the central Iran inclusion is because of two factors: 1) the transmission of horizontal stresses by the rigid inclusion to the northern parts and 2) the compression of material in the narrow region in between the inclusions, or in the case of one-inclusion models, between central Iran and the northern boundary. The presence of lateral heterogeneities (especially the Caspian block) also affects the crustal thickness gradient in the western side of the mesh. The direction of the gradient, changes from northwest-southeast, to southwest-northeast.

In order to reduce the steep slopes of crustal thickness in the areas surrounding the central Iran inclusion, which is not supported by observed topography, a transitional rheology structure has been considered. A zone of intermediate viscosity has been placed in between central Iran and the neighbouring regions. For the case of $R = 5$, the

Figure 3.17 Time development of the crustal thickness in a heterogeneous model with boundary condition set 1, $n = 3$, $Ar = 3$, and an intermediate rheology between the central Iran inclusion and its surroundings. The initial geometry of the model is depicted in (a), where $R_2 = 1.5$ refers to the rheology contrast between the intermediate zone and the medium. Crustal thickness is shown in times; (b) 5 m.y., (c) 10 m.y., (d) 15 m.y.



viscosity of this zone is assumed to be half of that of the inclusion. Figure 3.17 shows the configuration of this model and the resulting crustal thickness. Although the slopes are somewhat smoother and the area of less thickening has expanded by this modification, the maximum crustal thickness is increased both in the south and north of central Iran, mostly due to the fact that the area of the weakest lithosphere is diminished, and horizontal deformation becomes more restricted. Nevertheless the patterns of topography resulted from this crustal thickness distribution are closer to reality, than those from the other models.

The effect of Argand number on the crustal thickness is studied through the profiles of thickness along the line AA' in Figure 3.1b. The profiles are shown in Figure 3.18. As A_r increases, thickening in regions both in front and behind the central Iran depression decrease, while the depression itself is shortened and undergoes a slightly more thickening. The areas near the boundaries of the depression show greater rate of thickening, since these parts are the site of maximum compression against the rigid inclusion. In the north, maximum compression gradually moves towards the northern boundary as time proceeds, and so does the area of maximum thickened crust.

The patterns of shear strain rate are also strongly affected by the heterogeneities (Figure 3.19). Zones of strong shearing begin to develop, as a result of extrusion of material from regions between southern boundary and central Iran, and central Iran and the Caspian block (see Figure 3.14), whereas shearing is reduced inside the central Iran inclusion, due to its rigid body deformation. In comparison to a homogeneous model, shearing near the southern boundary in heterogeneous models ($R = 5$) is raised by 50%.

Stress fields and style of faulting

The effects of the power law exponent and Argand number on the stress fields,

Figure 3.18 Profiles of crustal thickness for heterogeneous models, along the line AA' in Figure 3.1b, at time intervals of 3 m.y. A rheology contrast of 5 is chosen for the central Iran inclusion. The slight increase in the crustal thickness, in the south of the (left in the profiles) inclusion is due to the intermediate rheology in this part ($R_2 = 2.5$).

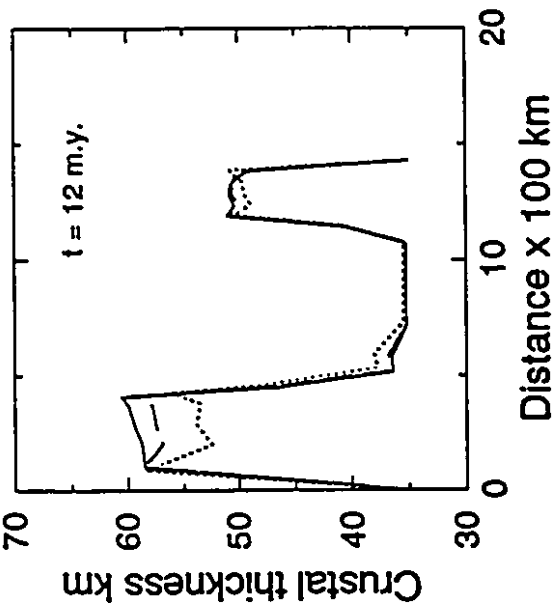
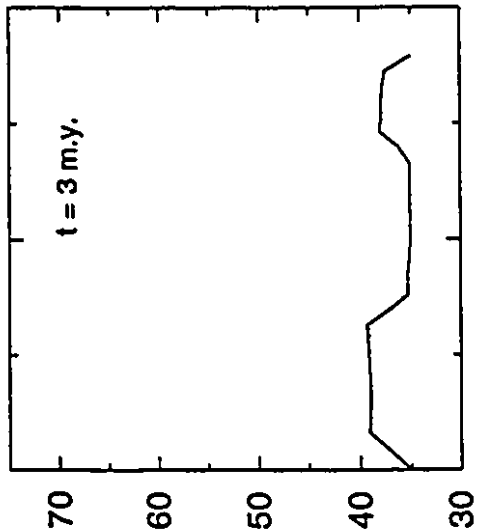
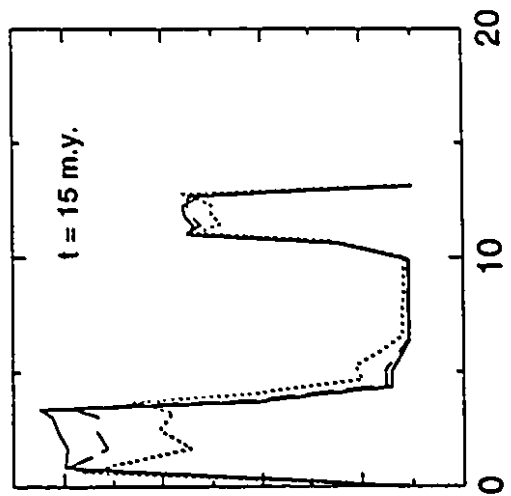
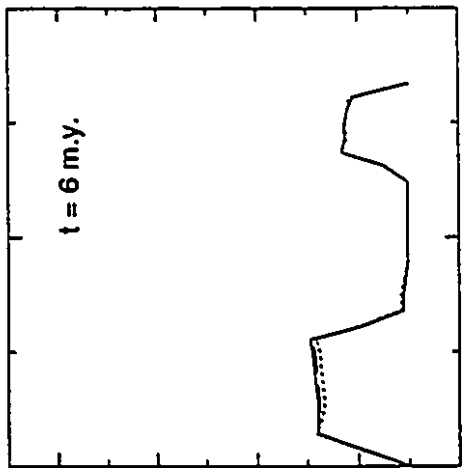
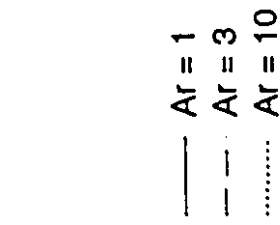
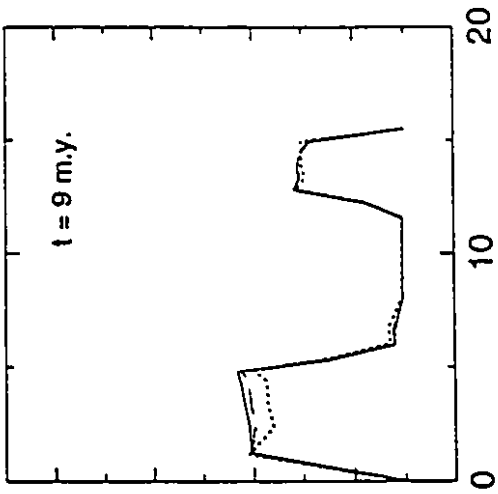
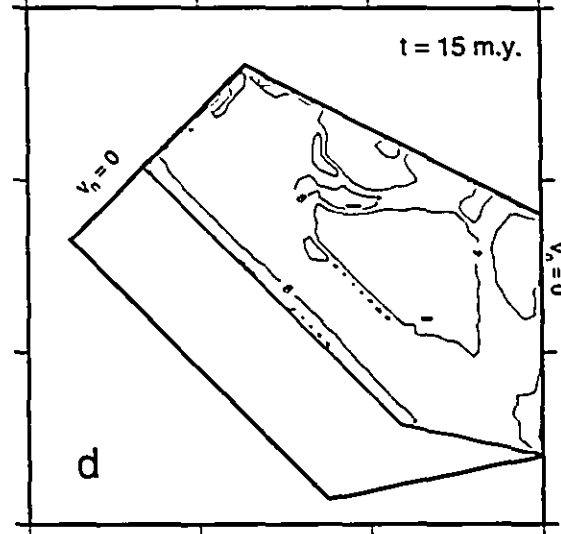
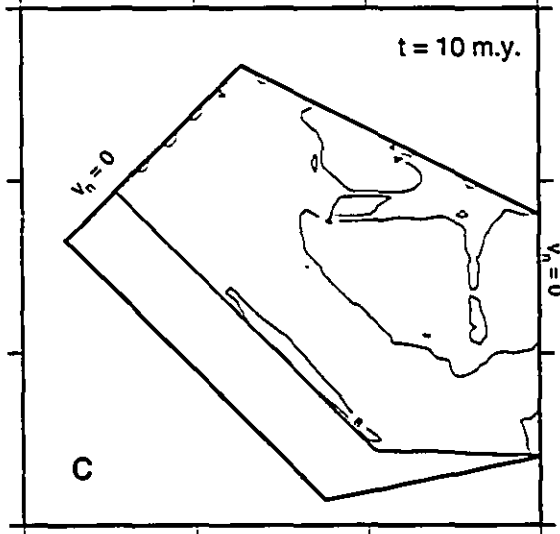
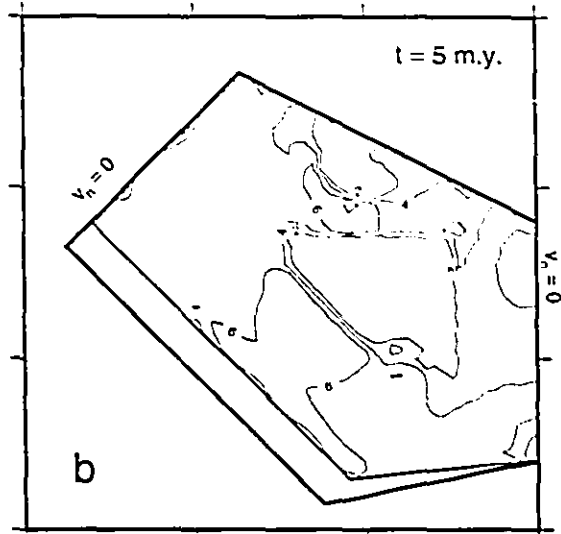
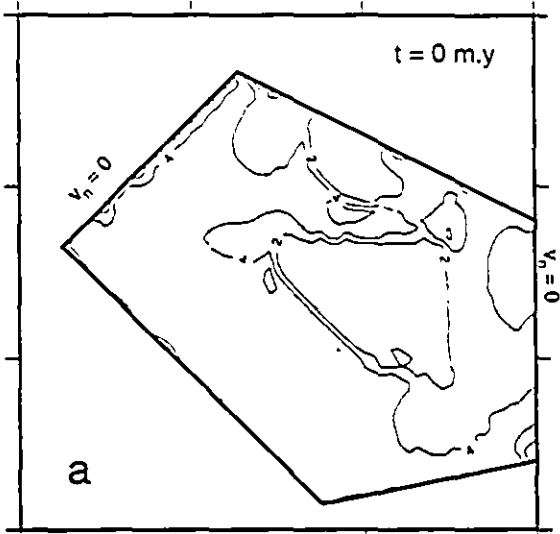


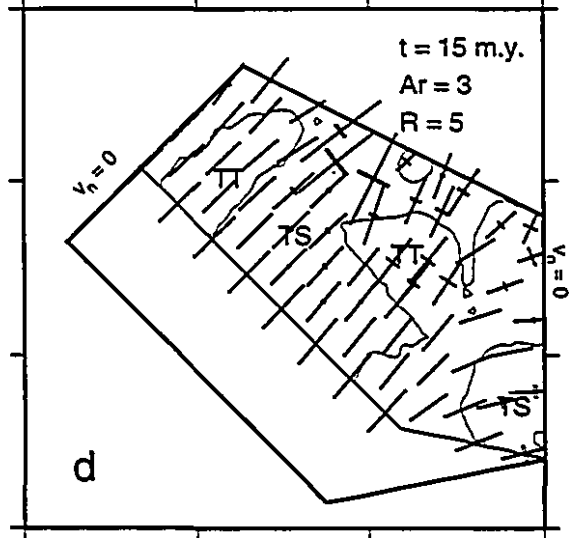
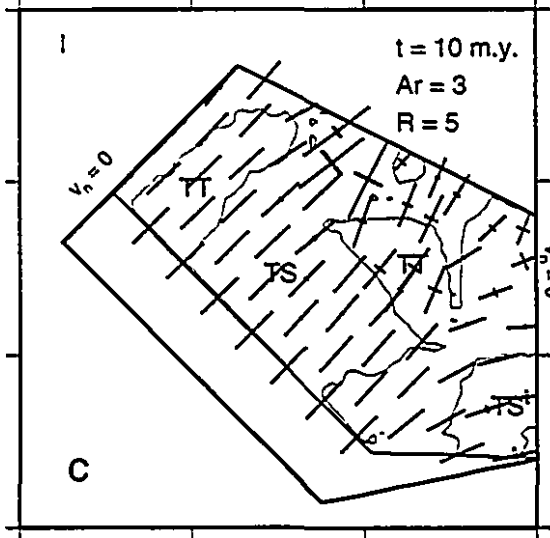
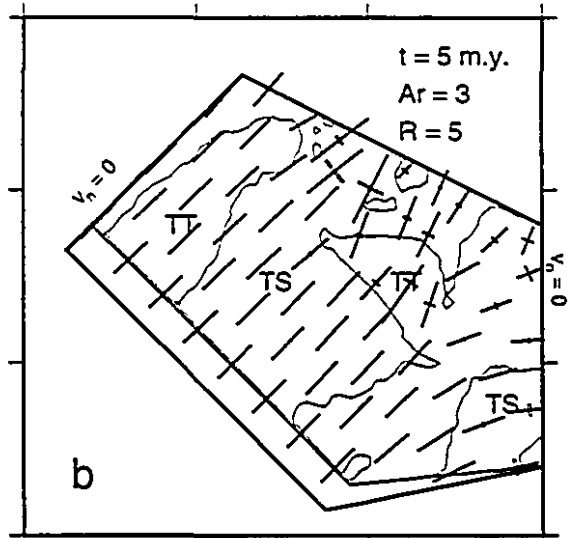
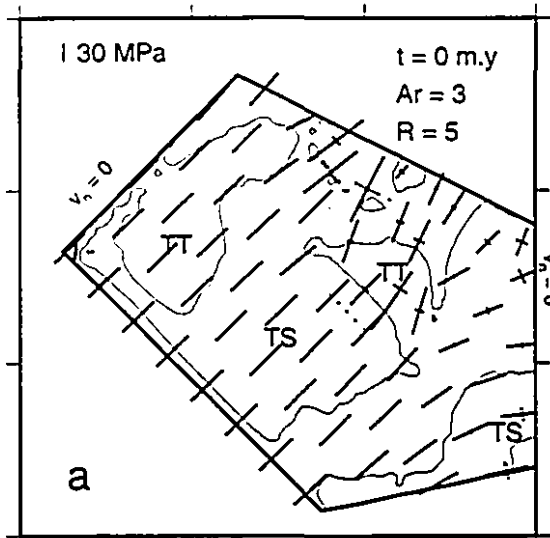
Figure 3.19 Maximum shear strain in a heterogeneous model with boundary condition set 1, $n = 3$, $Ar = 3$ and $R = 2$, at times: (a) $t = 0$, (b) $t = 5$ m.y., (c) $t = 10$ m.y., (d) $t = 15$ m.y. Contours are in units of $10^{-16}s^{-1}$.

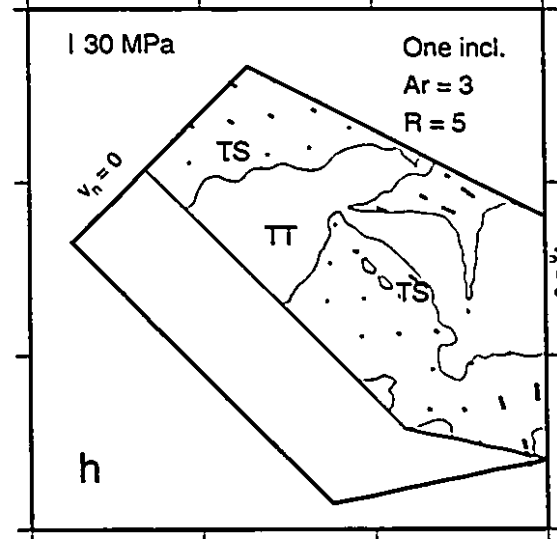
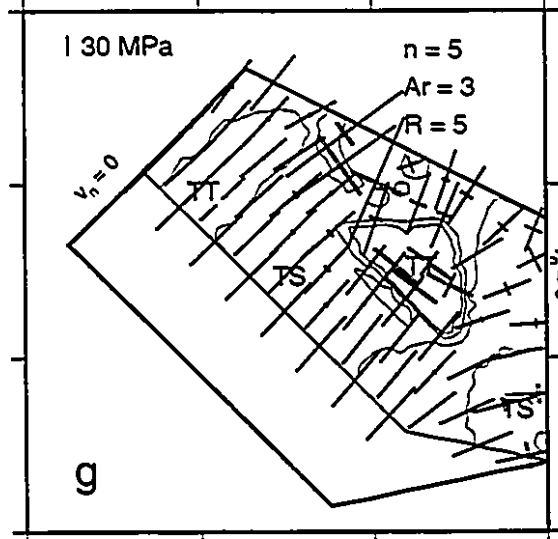
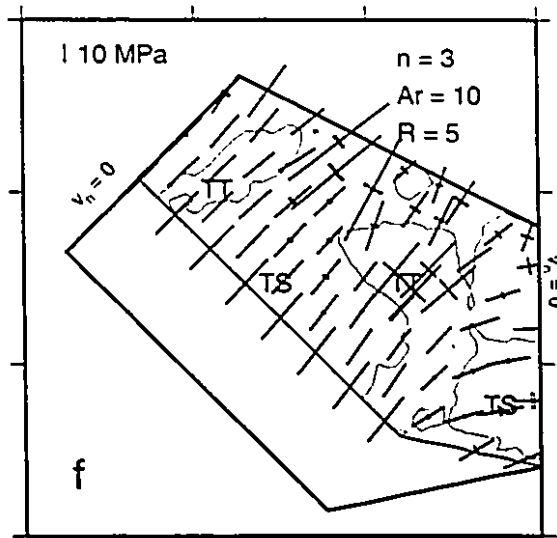
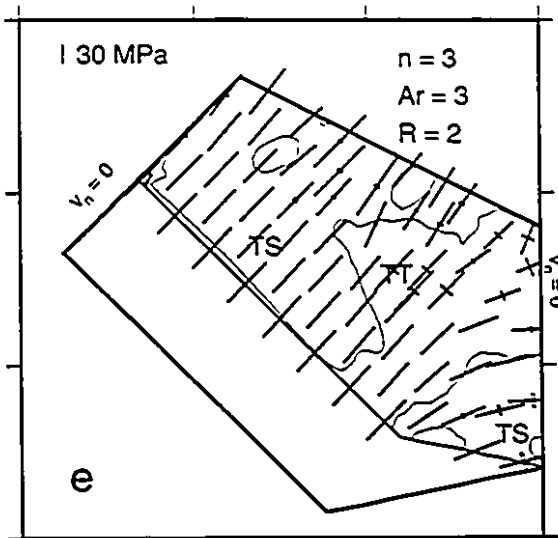


are similar to those in the homogeneous models. However the heterogeneities bring about several significant changes to the stress patterns which result in different styles of faulting other than those of the homogeneous models (Figure 3.20). These changes could be described in terms of three major effects: 1) The magnitudes of stresses are increased inside the inclusions and in their immediate vicinity. For example, for a model with $n = 3$, $Ar = 3$ and $R = 5$, the maximum stress at $t = 15$ m.y. is about twice that of a corresponding homogeneous model, and is located in the Caspian inclusion rather than in front of the southern boundary. 2) There is some rotation of the principal stress axes near the inclusions, which is resulted from the changes in the gradient of velocity field, induced by the presence of the inclusions. 3) The velocity gradient also affects the styles of the principal stresses (especially the minor principal stress) throughout the mesh. Figure 3.20 shows that, tensional stress in the direction of minor principal axis, is increased in the surroundings of the rigid inclusions, which in an otherwise homogeneous plate would be the site of essentially uniaxial compression (Figure 3.12).

The flow fields, ultimately affect the style of surface faulting. The comparison of contour lines separating regions with different styles of faulting, in Figures 3.20 and 3.12, reveals major differences between the heterogeneous and homogeneous models. In the homogeneous models, the predominant style of faulting in the west is thrust faulting plus minor strike-slip (style TS) and it remains so for all times. In the heterogeneous models, however, thrust faulting on both principal planes (style TT) dominates the western part of the mesh, but the extend of the area under the style TT decreases slightly as time proceeds. The increase in strike-slip faulting in the western parts at the final stages of deformation, is more tangible when the viscosity contrast between the inclusions and the mesh, or the Argand number is increased. The dominance of style TT in the west could be attributed to the fact that the rigid

Figure 3.20 Plots of principal horizontal deviatoric stress axes and contours of styles of faulting for heterogeneous models. **(a)-(d)** the time variations of the stress field for a model with boundary condition set 1, $n = 3$, $Ar = 3$ and $R = 5$, **(a)** $t = 0$, **(b)** $t = 5$ m.y., **(c)** $t = 10$ m.y., **(d)** $t = 15$ m.y. **(e)-(h)** stress fields at $t = 15$ m.y. for models with boundary condition set 1 and different parameters; **(e)** $n = 3$, $Ar = 3$, $R = 2$, **(f)** $n = 3$, $Ar = 10$, $R = 5$, **(g)** $n = 5$, $Ar = 3$, $R = 5$, **(h)** one-inclusion model with $n = 3$, $Ar = 3$, $R = 2$. All the symbols on the plots are as same as those in Figure 3.12.



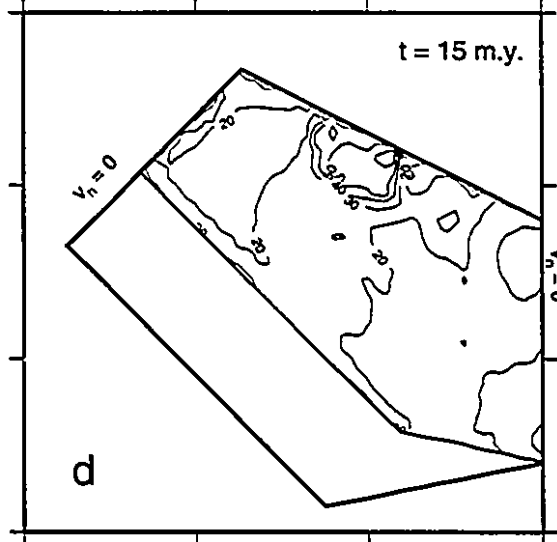
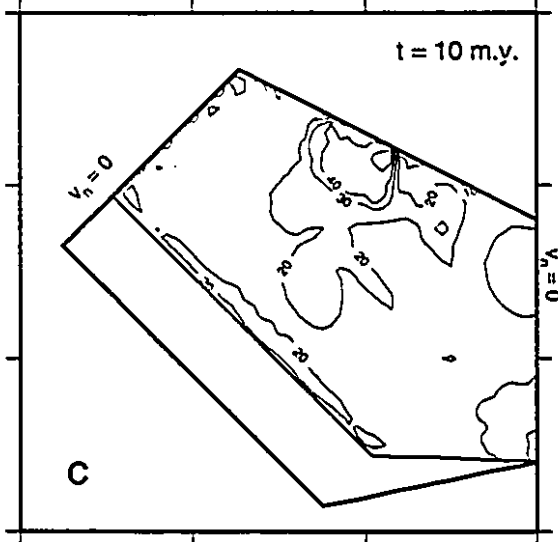
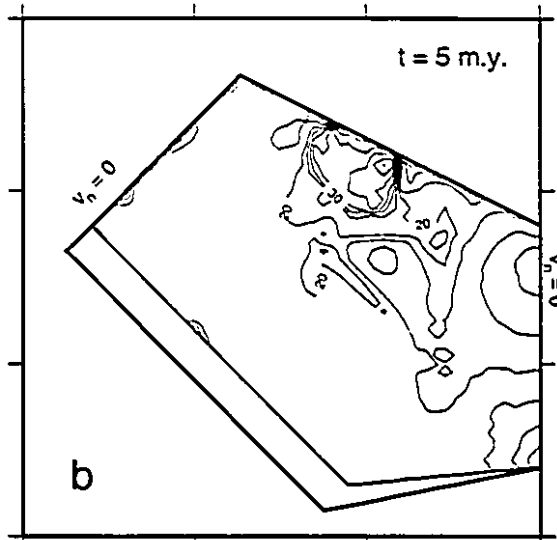
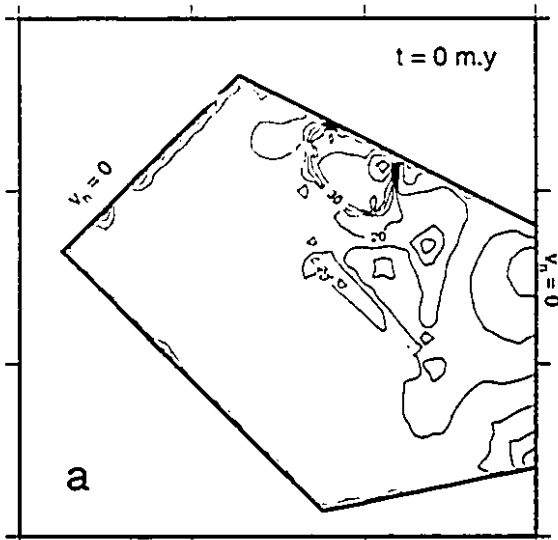


inclusions act as some barriers, confining the flow to the western regions and preventing the material to move towards the east. Indeed, the examination of the velocity fields shows that there is less eastward component of velocity in heterogeneous models than it is in a homogeneous one. This observation is affirmed if one of the inclusions (i.e. the Caspian inclusion) is removed (Figure 3.20h).

In the southern, central and northeastern regions, thrusting is the principal form of faulting in the homogeneous models. However, in the heterogeneous models, the regions surrounding the inclusions undergo some strike-slip faulting (style TS) and thrust faulting is concentrated inside the inclusions. The proportion of strike-slip motion in the south of the Caspian block is so high, that at early stages of deformation style ST (strike-slip faulting plus minor thrusting) develops in that region. The better development of a strike-slip zone to the east of the central Iran inclusion in models with larger rheological contrast, is due to the fact that the rigid body rotation of a stronger inclusion causes more slip along its boundary, and therefore the stress patterns become less uniform inside and outside the inclusion.

The enhancement of strike-slip motion in the heterogeneous models is also visible in the plots of maximum shear stress. Figure 3.21 shows that strong shear zones develop around the inclusions as the convergence proceeds. The growth of shear zones in the region between the two inclusions, and in the southwest of the central Iran inclusion is attributed to the lateral extrusion of material away from the zone of intense thickening. In the east of central Iran, the shearing is the result of rotation of the rigid inclusion. The rheology contrast also affects the intensity of the shearing, the greater the ratio R , the greater the shear stress becomes.

Figure 3.21 Time development of the maximum shear stress in a heterogeneous model with boundary condition set 1, $n = 3$, $A_r = 3$ and $R = 2$, at (a) $t = 0$, (b) $t = 5$ m.y., (c) $t = 10$ m.y., (d) $t = 15$ m.y. Contours are in units of 1 MPa.



Chapter 4

Discussion and conclusions

4.1 Comparison of results with tectonic observations in Iran

In this chapter attempts are made to compare the results of numerical experiments derived in the previous chapter, with the observations of topography, crustal structure, fault plane solutions and rates of deformation, calculated from seismic and gravity studies in the Iranian Plateau. It should be mentioned that the numerical results of the models presented here, are the outcome of numerous simplifications on the physical properties and geometry of the lithosphere. For example, the effect of vertical variations in the lithosphere (rheology, temperature profiles etc) on the deformation has been ignored, and lateral heterogeneities are kept at the simplest level. The role of previous phases of orogeny and the pre-Miocene crustal structure of Iran are neglected. Erosion and faulting in the upper crust and friction at the base of the lithosphere are not accounted for, and the resolution of the finite element grid is such that, the resolution of the results is not better than 70 km. Therefore these results do not simulate the fine details of tectonic characteristics of Iran. However, there is a reasonable agreement between the calculations and observations in the scales of hundreds of kilometers, and the discussion will be confined to comparisons in such large scales, and to point out the influence of different parameters on the deformational processes.

4.1.1 Crustal thickness and topography

Although the knowledge of crustal thickness distribution in the Iranian plateau is not comprehensive, the few investigations carried out so far, have resulted in more or less parallel information. The study of phase velocity dispersion of surface waves and P-wave velocity data in Iran (Asudeh 1982) shows that, the crust in southwestern Iran has a thickness of about 43 km, and thickens by about 10 km in the north-northeast direction across the Zagros mountains. A gravity modelling by Snyder & Barazangi (1986) supports the results of other seismic studies (e.g. Asudeh 1982) that the Moho dips about 1° to the northeast beneath the folded belt of Zagros, and increases in dip to 5° near the main Zagros thrust (MZT); the depth of the Moho increases from 40 km in the southwestern edge of the Zagros, to 58-65 km beneath the MZT. Seismic refraction studies (Geise et al. 1983) estimate the crustal thickness in the Zagros to be around 55-60 km. The results of all these investigations are suggestive of presence of a northeastward thickening crust in western and southern Iran, and a thickness of 65 km is an upper limit. Table 4.1 shows the average crustal thickness in the region of the mesh corresponding to the Zagros mountains, and the maximum crustal thickness at the northeastern border of the Zagros for homogeneous and heterogeneous models with different values of parameters n and A_r . This table and the crustal thickness plots in Figures 3.12 and 3.16, and the observations mentioned above reveal that all the homogeneous models fail to reproduce an acceptable crustal structure in the Zagros mountains. The average crustal thickness in the homogeneous models is 51-53 km, which is about 5 km less than the estimated thickness. Furthermore, these models predict that the thickness of the crust is decreased in the northeast direction, rather than being increased. Heterogeneous models, on the other hand, result in crustal structures that are closer to observations, both in average thickness and the gradient of thickening.

Table 4.1 Calculated crustal thicknesses in the Zagros region. The average thickness in the Zagros are in the third column. The fourth column presents the thickness of the crust on the border of the Zagros and central Iran.

n	Argand Number	crustal thickness in the Zagros (km)	
		average	NE border

Homogeneous models

1	1	51.5	52
3	1	53	52.5
3	3	52	52
3	10	50	51
5	1	54	53
5	10	52	51
10	1	56	53

Heterogeneous models

1	3	55	55
3	1	58	60
3	3	59	60
3	10	53	53
5	1	62	63
5	3	59	60
10	1	63	65

The average thickness in the Zagros mountains predicted by heterogeneous models is 53-63 km, and in most of the models, the crust thickens toward northeast. Table 4.1 implies that, the parameter range best capable of reproducing the observed crustal thickness distribution in the Zagros is, n between 3 and 5, and Argand number between 1 and 3. Newtonian materials or very weak lithosphere ($Ar \sim 10$) are unlikely to produce the sufficient crustal thickness beneath the Zagros mountains, and strongly power law materials ($n > 5$) in heterogeneous models result in thicknesses which exceed the observations. As for the parameter R , rheology contrasts greater than 2 result in extensive crustal thickening in the regions of intense compression.

To the north of central Iran in the region of northern ranges of Iran, crustal thickness is estimated to be around 46 km (Asudeh 1982). The thicknesses predicted by both homogeneous and heterogeneous models in this region, fall in the range of 47-53 km, with those of heterogeneous models of slightly greater values. In central Iran however the thicknesses calculated from the heterogeneous models, are considerably less than those inferred from the observations. The thickness of the crust in most of the models even when rheology contrast is not too large, does not exceed 40 km. This suggests that the contrast between the rigidities of central Iran and the deforming belts could be of much less value than is used in the numerical experiments. It should be mentioned that the final evolution of the crust is subject to many uncertainties in the initial assumptions of the problem, for example uncertainty in the initial thickness, or uncertainty in the time period and rate of convergence. Any modification in these parameters, may produce significant differences in the crustal thicknesses.

The change in the topography is related to the change in crustal thickness by;

$$(e - e_0) = (S - S_0)(1 - \rho_c / \rho_m) \quad 4.1$$

where e , S , e_0 , and S_0 are the final and initial surface topography and crustal thickness,

and ρ_c and ρ_m are the crustal and mantle densities, respectively. A crust of thickness of 35 km is assumed to produce zero elevation. With this assumption and the density values given in chapter 3, the corresponding topography map for various heterogeneous models is obtained from equation 4.1. The results of calculations and a topography map of Iran are shown in Figures 4.1. Most of the heterogeneous models with two inclusions are capable of reproducing the surface elevation distribution in the Iranian plateau similar to the observed topography. The regions of highest elevation in the plateau include the central and southern parts of the Zagros, and the central part of the Alborz ranges, located to the southwest and north of central Iran, respectively. The effect of the two rigid inclusions on the topography distribution of the models, is clearly evident from the presence of two distinct elevated regions around the inclusions. The models have also been successful in predicting the low relief topography in central Iran, and the less elevated Kopeh Dagh mountains and the eastern ranges. The choice of boundary conditions especially in the western side, significantly alters the topography patterns.

Although there are many similarities between the results of the experiments and the patterns of observed topography, the amount of surface elevation predicted by most of the models is somewhat greater than the observed. For models with strong lithosphere (e.g. $n = 5$, $Ar = 1$) the average topography in the region of highest elevation in the southern part of the mesh is as much as 1 km more than the average elevation in the Zagros mountains. The average topography is still 500 m above the average elevation in western Iran when the lithosphere is very weak (e.g. models with $n = 3$, $Ar > 10$). Again, it should be emphasized that the initial assumptions and the choices of physical parameters, can significantly change the results of the calculations. For example, with the densities adopted, a difference in crustal thickness of 9.4 km can produce a surface elevation of 1 km. Thus if an initial crustal thickness of 30 km had

Figure 4.1 Plots of surface elevation at $t = 15$ m.y., (a) surface elevation map of Iran estimated over $0.5^\circ \times 0.5^\circ$ elements. (b) topography map for a homogeneous model with boundary condition set 1, $n = 3$, $Ar = 3$. (c)-(f) topography map for heterogeneous models with boundary condition set 1. (c) $n = 3$, $Ar = 1$, $R = 5$. (d) $n = 3$, $Ar = 3$, $R = 5$. (e) $n = 5$, $Ar = 1$, $R = 5$. (f) $n = 5$, $Ar = 3$, $R = 5$. Contours are in units of 1 km.

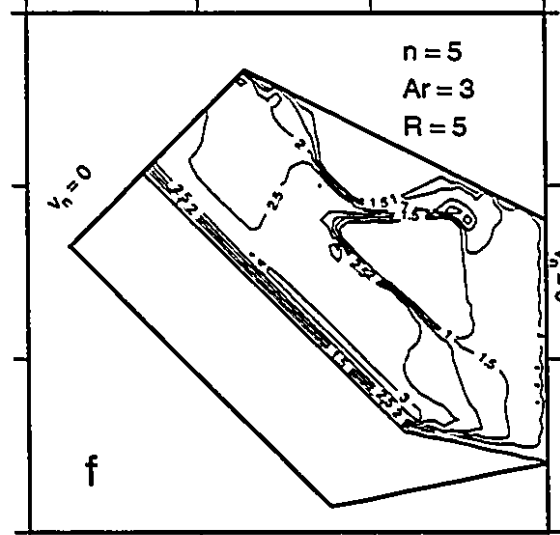
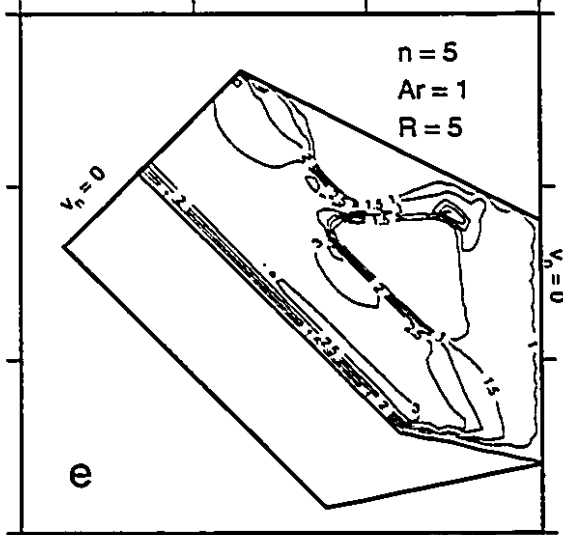
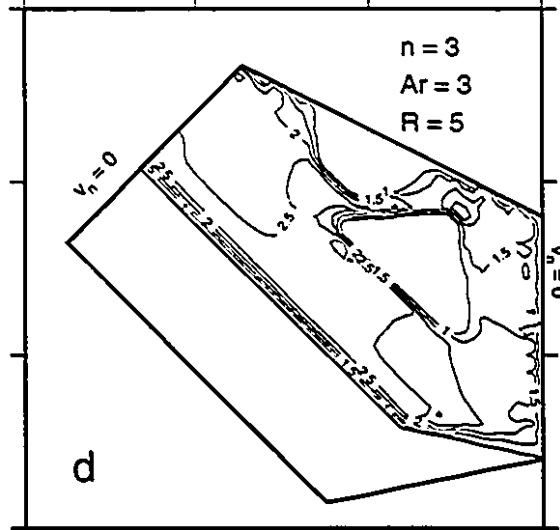
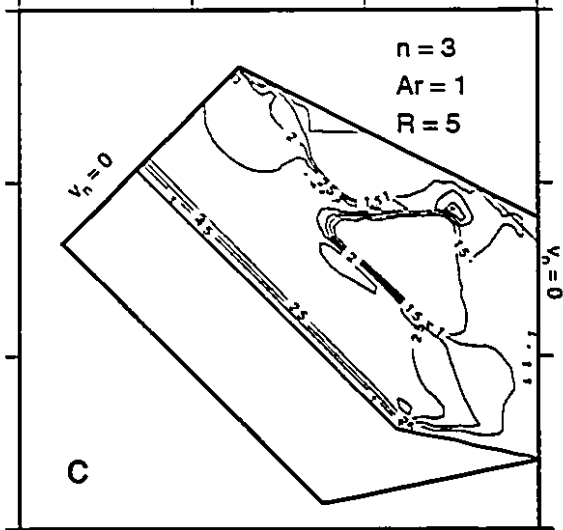
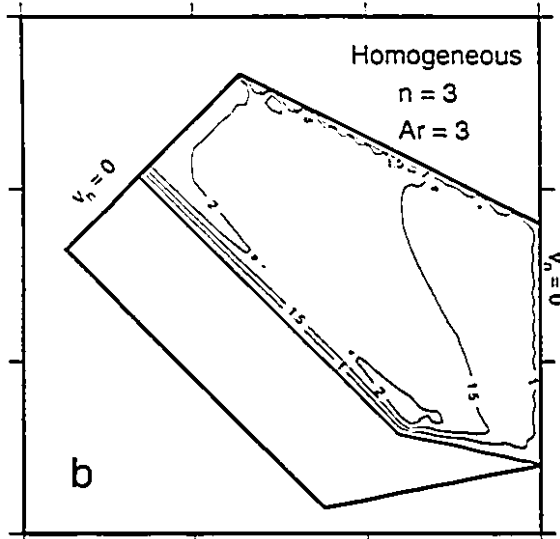
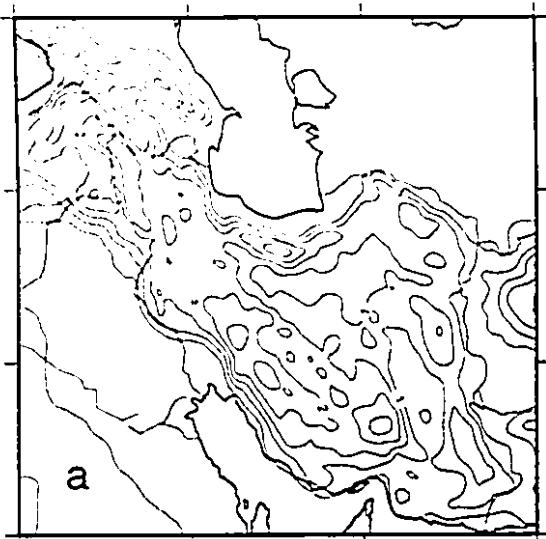
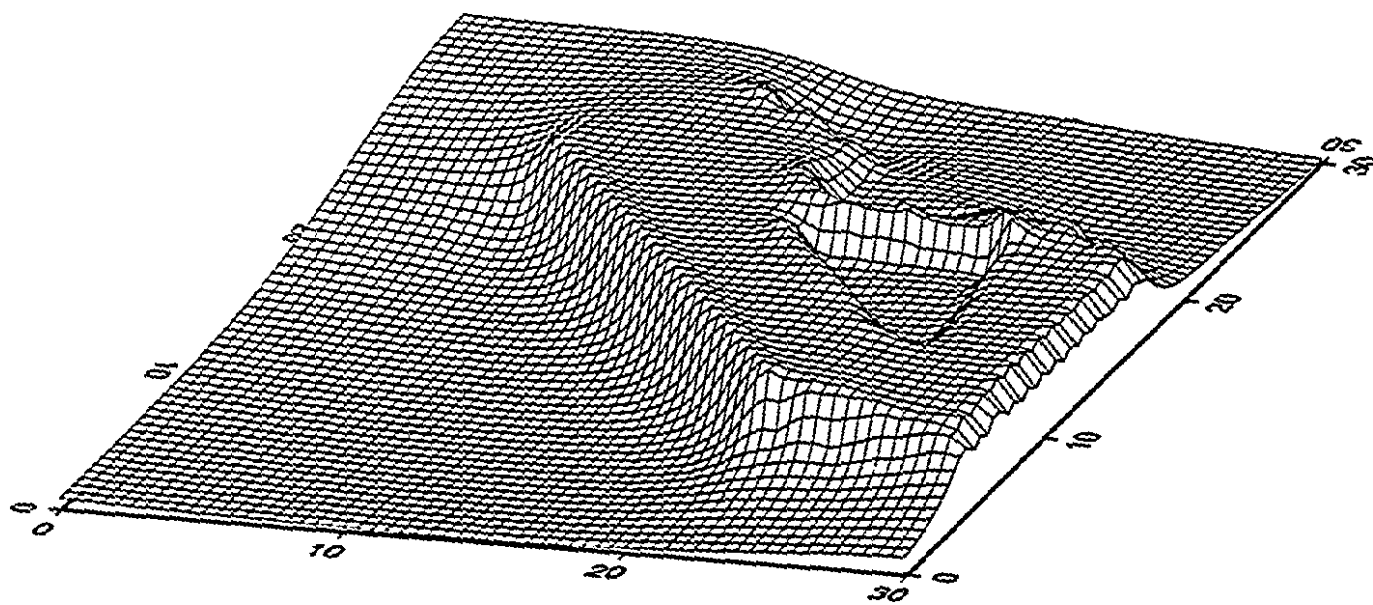


Figure 4.2 A three dimensional topography map of heterogeneous model with boundary condition set 1, $n = 3$, $Ar = 3$ and $R = 5$.



been used, the average elevation in the models would have been 530 m less than that in the present models.

4.1.2 Strain rates and vertical deformation

In this section the calculated horizontal and vertical strain rates, along with the rate of crustal thickening and the rate of uplift of the surface, are compared with the observed strain rates in Iran and the Caucasus. Jackson & McKenzie (1988) examined the relation between seismic moment rate tensors in the region of distributed deformation in the Mediterranean and the Middle East, and calculated the strain rate tensor and overall velocities for the region. They divided the region into several sub-regions (e.g. Zagros, northeastern Iran, Caucasus, etc). In each sub-region, the summed seismic moment rate tensor was calculated from 70 year seismicity data, and compared with the moment rate tensor obtained from slip directions and relative velocity magnitudes predicted by global plate motions. Jackson & McKenzie suggested that in the Zagros and Caucasus sub-regions seismic deformation can account for only 10-20 percent of the total motion, whereas in northeastern Iran most of the deformation (more than 50%) in the upper crust is accommodated seismically. In table 4.2a the strain rates calculated by Jackson & McKenzie (1988) from seismic moment rate tensors (referred to, as the matrix, M by the authors) in three sub-regions, the Zagros mountains, northeastern Iran (including the Alborz, Koppeh Dagh and eastern Iran), and the Caucasus and eastern Turkey, are listed. Also presented in the table, are the strain rates calculated from the moment rate tensor, predicted from plate motions (matrix N) by Jackson & McKenzie. The latter values of strain rates are calculated, to show, what the range of the strain rates would be, if all of the deformation were taken up aseismically.

In Figure 4.3 the horizontal components of the strain rate field for the final time

Table 4.2 Seismic and overall deformation in Iran and the Caucasus (taken from Jackson & McKenzie 1988). (a) In the first column, the magnitudes of the horizontal normal components of the seismic moment rate tensor, \dot{M} for each region are given. The horizontal normal components of the strain rate, calculated from \dot{M} , are given in column 2. In columns 3 and 4, the components of the matrix \dot{N} and the corresponding calculated strain rate are listed, respectively. The moment rates are in units of 10^{25} dyn cm^2s^{-1} , and the strain rates are in units of 10^{-16}s^{-1} . (b) The uplift rates (v_u) and crustal thickening rates (v_c) in units of mmy^{-1} , calculated from the vertical component of the matrix \dot{M} , at different areas of the deforming zone.

(a)

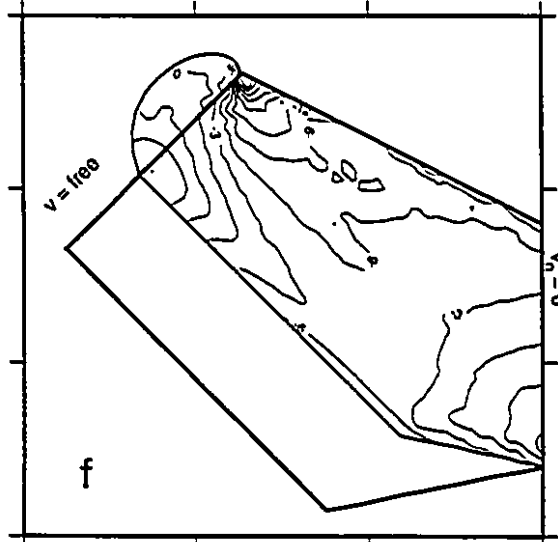
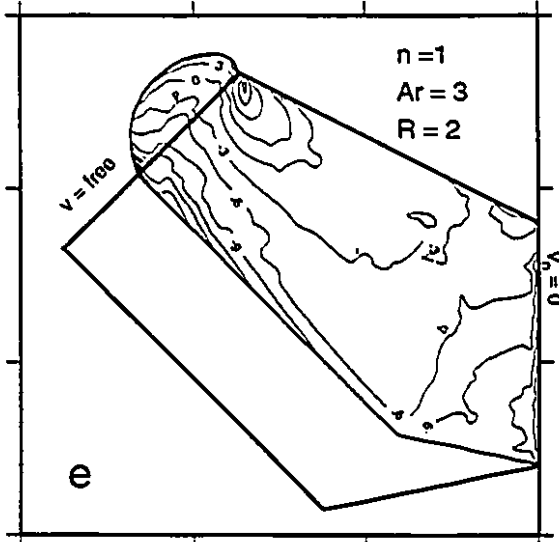
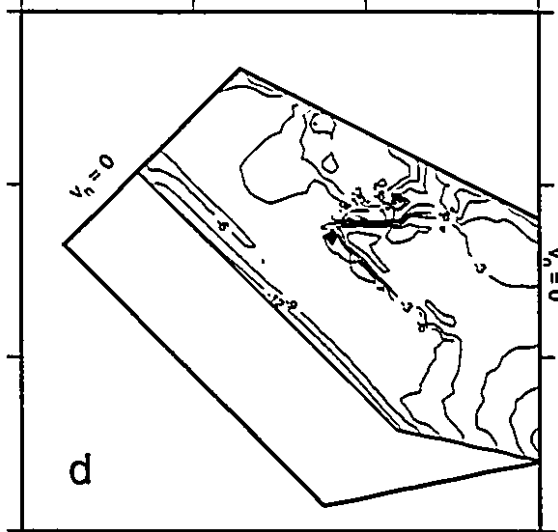
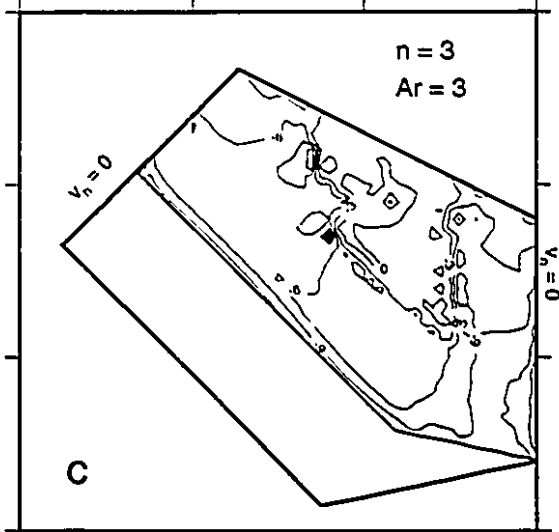
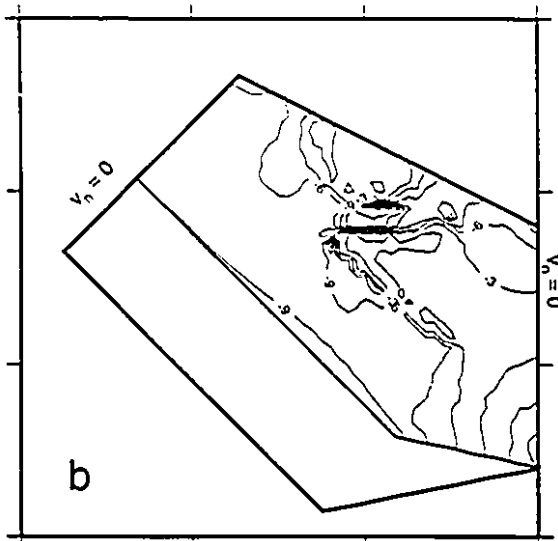
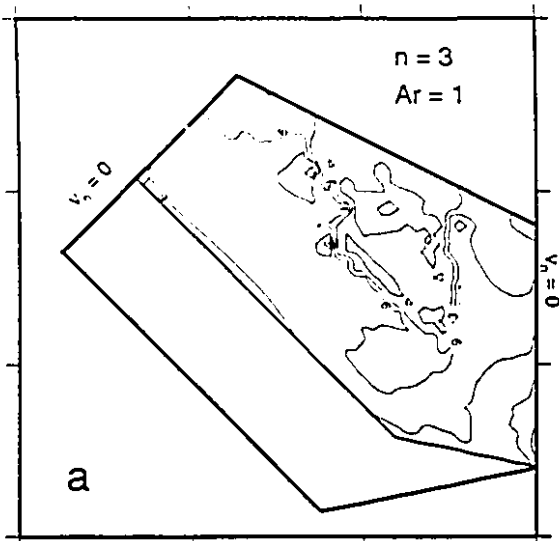
	\hat{M}	$\hat{\epsilon}$	\hat{N}	$\hat{\epsilon}$
Whole Zagros				
xx	1.40	2.50	-6.75	-12.5
yy	-3.61	-6.50	-29.79	-54.0
Central Zagros				
xx	-0.07	-0.13	-5.29	-9.50
yy	-0.90	-1.60	-12.29	-22.2
Northeast Iran				
xx	-1.81	-1.93	-3.82	-4.10
yy	-5.80	-6.20	-9.01	-9.62
Eastern Turkey and the Caucasus				
xx	1.54	1.0	0.00	0.00
yy	-1.67	-0.90	-16.20	-11.90

(b)

	Central Zagros	NE Iran	Caucasus and E Turkey
v_c	0.21	1.01	< 0.27
v_c	0.04	0.17	< 0.05

step of some of the models are plotted. The time step is of order of 100-300 thousand years, and the strain rates are assumed to be constant over the time step. Although it is difficult to relate the short term seismic deformation to deformation over geological time spans, comparison of the figures in table 4.2a with the plots of Figure 4.3, provides several valuable points: First of all, the moment rate tensors and the strain rates calculated from both seismicity data and plate motions, show an overall compression and thickening throughout the Iranian plateau, a feature that is consistently arrived at, by the stresses and strain rates obtained from the numerical models. Second, the magnitudes of the strain rates derived from the models are in reasonable agreement with those calculated from the moment rate tensor N , and, as Shoja-Taheri & Niazi (1981), Ambraseys & Melville (1982), Jackson & McKenzie (1988) and Ekström & England (1989) concluded there is in fact a shortage of seismic deformation in the Zagros and the Caucasus. The typical values of $\dot{\epsilon}_{yy}$ and $\dot{\epsilon}_{xx}$ in the regions of extensive deformation, for most of the models are about, $5-10 \times 10^{-16} \text{ s}^{-1}$, which fall in the range of strain rates calculated from the tensor N , and far greater than those calculated from seismic moment rates. It can be seen that, strain rates in the Zagros, obtained from the tensor N have greater values than those calculated from the models. This could be due to the fact that the width of the seismogenic layer in the Zagros, chosen by Jackson & McKenzie (1988), is considerably less (200 km) than the width of the region of deformation in front of the southern boundary of the numerical models (400 km). Still the strain rates from the models are at least an order of magnitude greater than the observed seismic strain rates in the Zagros mountains. Also noticeable is that the values of the seismic strain rates in the Caucasus and eastern Turkey are suggestive of crustal thinning. This is because the shortening in the Caucasus and normal faulting in eastern Turkey are considered together. The strain rate field of a model with free boundary in the west (Figure 4.3e-f) clearly shows that the sideways motion of material

Figure 4.3 Horizontal components of strain rate ($\dot{\epsilon}_{xx}$ and $\dot{\epsilon}_{yy}$) at $t = 15$ m.y. for different models. (a)-(b) $\dot{\epsilon}_{xx}$ and $\dot{\epsilon}_{yy}$ respectively, for a heterogeneous model with boundary condition set 1, $n = 3$, $Ar = 1$ and $R = 5$. (c)-(d) $\dot{\epsilon}_{xx}$ and $\dot{\epsilon}_{yy}$ respectively, for a heterogeneous model with boundary condition set 1, $n = 3$, $Ar = 3$ and $R = 5$. (e)-(f) $\dot{\epsilon}_{xx}$ and $\dot{\epsilon}_{yy}$ respectively, for a heterogeneous model with boundary condition set 3, Newtonian material, $Ar = 3$ and $R = 2$. Contours are in units of $10^{-16}s^{-1}$.



normal to the direction of thickening, could result in thrust faulting with strike-slip motion in the Caucasus, and crustal extension further in the south.

The moment rate tensors can also be used to determine the present day vertical strain rates and velocities in the crust. Table 4.2b shows the thickening rate of the crust (taken to be 40 km) and the corresponding rate of surface uplift calculated by Jackson & McKenzie (1988). The rate of surface uplift is obtained from:

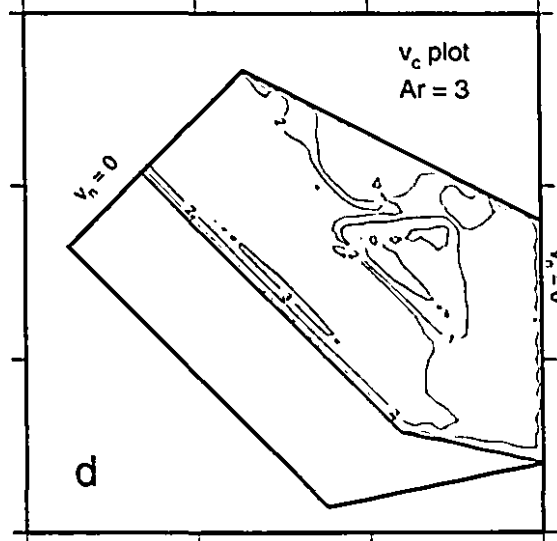
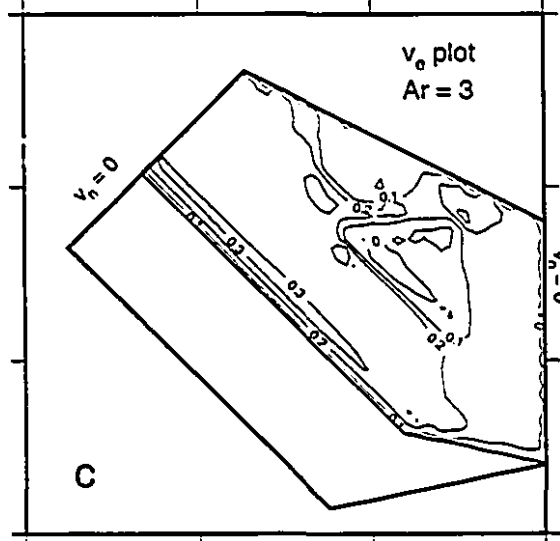
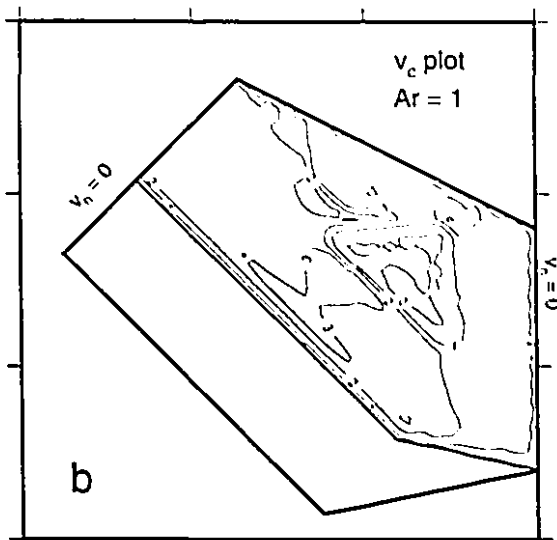
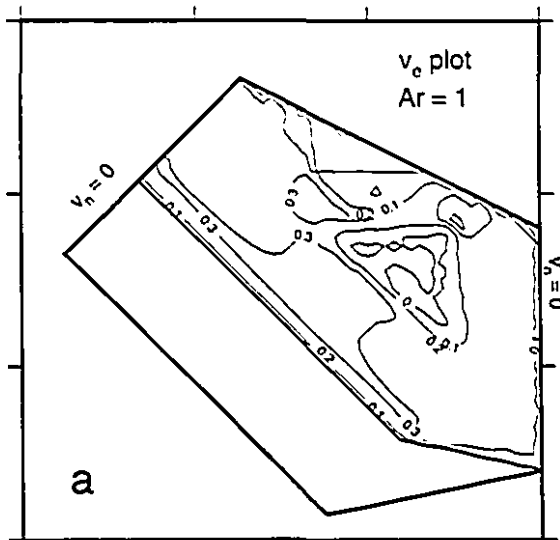
$$v_e = (1 - \rho_c / \rho_m) v_c \quad 4.2$$

where v_e and v_c are the rates of surface uplift and crustal thickening, respectively. In Figure 4.4 the distribution of v_e and v_c for some of the heterogeneous models are illustrated. The average rate for crustal thickening in the models is about 2 $\text{mm} \cdot \text{y}^{-1}$, and for that of surface elevation, around 0.2 $\text{mm} \cdot \text{y}^{-1}$. Again, the results show that in the Zagros and Caucasus seismic deformation can not produce more than 10% of the thickening and surface uplift, while there is no serious discrepancy between the seismic observations and numerical modelling in northeastern Iran. Increasing the crustal thickness to 55 km (which is observed in most of the numerical models), and adopting a smaller crustal density, will increase the vertical thickening in the seismic calculations at most by a factor of 2.5, which is still not satisfactory. However, the numerical results are not perfectly in accord with geological measurements. The rate of Holocene uplift in the strait of Hormoz is measured, 1.8-6.6 $\text{mm} \cdot \text{y}^{-1}$ (Vita-Finzi, 1982), and the estimated average uplift rate in the Zagros since the early Pliocene is about 1 $\text{mm} \cdot \text{y}^{-1}$ (Falcon 1974). These rates are four times greater than those shown in Figure 4.4.

4.1.3 Tectonic styles and fault plane solutions

As it was discussed before, although the continuum approach adopted in this

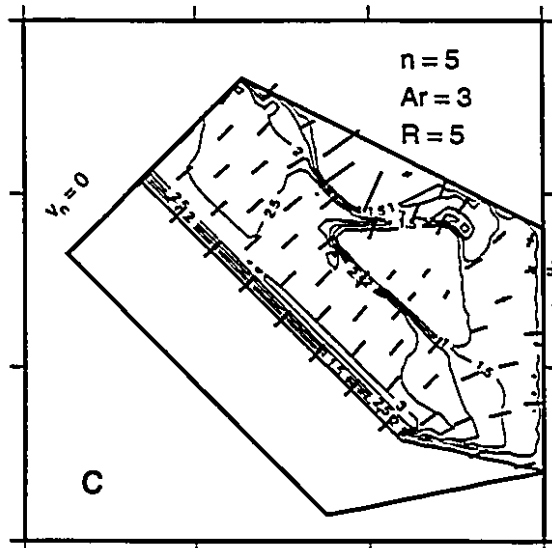
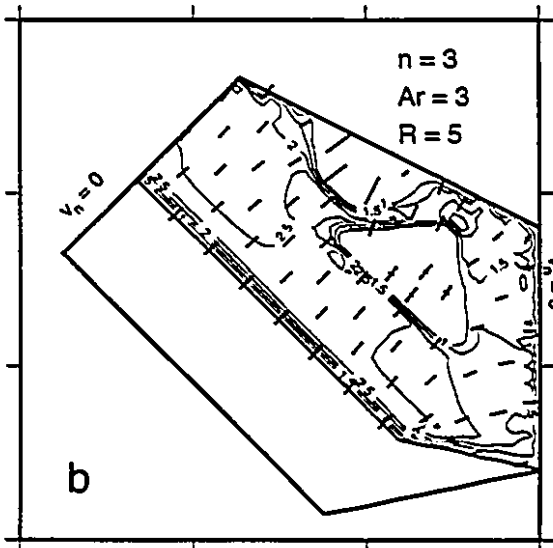
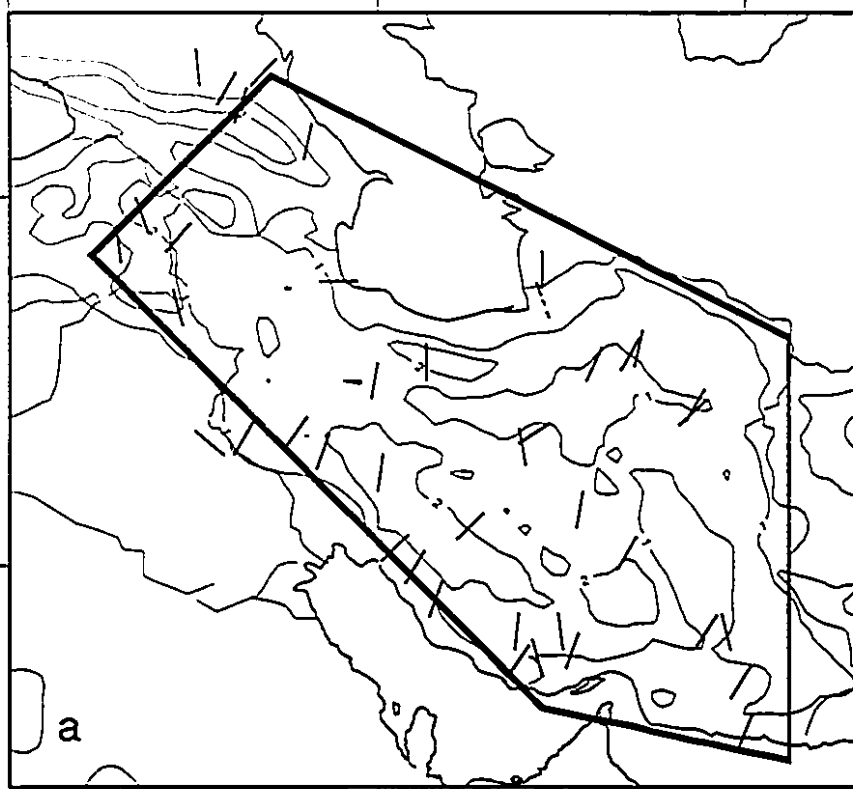
Figure 4.4 uplift rate (v_c) and crustal thickening rate (v_d) at $t = 15$ m.y. for heterogeneous models with boundary condition set 1. (a)-(b) $n = 3$, $Ar = 1$, $R = 5$. (c)-(d) $n = 3$, $Ar = 3$, $R = 5$. Contours are in units of 1 mmy^{-1} .



study, does not account for discontinuities in the crust, there are many parallel features between the deformation of the viscous lithospheric material, and that of the overlying brittle crust. Comparison of the stress fields calculated from the models with the P axes obtained from earthquake data shows some of these similarities. Figure 4.5 shows the direction of the horizontal projection of the P axes of some of the earthquakes in the period of 1970-1981 (Jackson & McKenzie 1984), on a topographic map. Also shown are the distribution of the principal horizontal stresses at $t = 15$ m.y., superimposed on the contours of topography for two heterogeneous models with $n = 3$, $A_r = 1$, $R = 2$ and $n = 5$, $A_r = 3$, $R = 2$. There is a general correspondence between the orientations of the P axes, and the directions of the steepest gradient of topography. The same feature is seen in the numerical models, the principal compressive stress axes are in general aligned in the direction of gradient of topography, and in most regions (the Zagros, Caucasus, Alborz and Kopeh Dagh) their orientations agree to within 20° with those of the P axes. The major disagreement between the calculations and observations occur in the Makran region in southeastern Iran, where the trends of the P axes are considerably towards the north, whereas the numerical models yield eastward compression. This is most likely due to the boundary condition assumed in the southeastern part of the models, which predict more eastward gradients of motion in eastern Iran.

The credibility of the results of the numerical models, can also be examined through the qualitative comparison of the style of faulting derived in the previous chapter, with the available earthquake focal mechanisms. In Figure 1.2 a seismicity map of Iran and the region between the Caspian and Black seas is shown, which includes the fault plane solutions of some of the large earthquakes in the region, as well as the direction of motion on the major fault lines. The principal features of this map was discussed in more detail in chapter 1. As mentioned the Iranian plateau is the site

Figure 4.5 (a) Comparison of the orientations of the horizontal projection of the P-axes of some of the large earthquakes in Iran, during the time interval of 1970-1981 (taken from Jackson & McKenzie 1984), and the surface elevation. The final boundaries of the numerical models is shown on the map. (b)-(c) the principal compressional axes superimposed on the topography plots for two of the heterogeneous models with boundary condition set 1, $A_r = 3$, $R = 5$; (b) $n = 3$, (c) $n = 5$.



of dominant shortening and thickening. Strike-slip motion is subordinate to thrust faulting, and takes place to some extent in the northwest Zagros, eastern Alborz, northern Caucasus and to the east and north of central Iran. The style of faulting in Figure 3.20 reveals major characteristics of the Iranian tectonics. In the central and southern Zagros style TS (thrusting in the northeast direction with minor strike-slip parallel to the strike) for all values of n , A_r and R , is the dominant form of deformation, and the fault plane solutions in this region support this conclusion. In the northwestern Zagros however, the style of faulting is more dependent on the choice of lithospheric strength. Decrease in the viscosity of the medium (i.e. increase in A_r), causes the weaker material to move more easily away from the impinging zone in the west. Therefore, it appears that greater Argand numbers can better explain the strike-slip motions in northwestern Iran and the Caucasus. Also, smaller rigidity contrast between the inclusions and the deforming zones allows for more sideways motion in the western part of the region.

In the region between the Caspian block and central Iran, and to the northeast and east of central Iran, the fault plane solutions show thrust faulting with some strike-slip motion. Thrust faulting takes place on the planes striking northwest-southeast, and strike-slip motion happens on two sets of faults, the first set runs from east to west and has left lateral sense of motion, and the second set is right lateral faults stretching in the north-south direction. These features can be traced in the models. Figure 3.20 shows that while the motion inside the rigid mass of central Iran is taken up by pure thrust faulting, the stress concentrations on its edges arising from rigidity contrasts, lead to appreciable extensions along its boundaries. Consequently, narrow zones of strike-slip motion develop in the east and north of central Iran. The strike-slip motion is more profound in the region between the rigid inclusions, since the stress concentration around the Caspian block contributes to the total strike-slip motion. However the

seismicity data do not show significant amount of strike-slip motion in the Alborz, and this could be suggestive of less compression in northern Iran than that calculated by the models. The strike-slip motion in eastern Iran is greatly affected by the viscosity of the deforming zones and the rigidity of central Iran and the Caspian. For moderate rigidity contrasts of $R = 2$, the strike-slip zone may not develop at all, unless the medium is too weak. Argand numbers greater than 3 and rheology contrasts greater than 2, produce results which are in better agreement with the surface faulting in eastern Iran. It is also noticeable that the presence of a rigid central Iran also affects the strike-slip faulting in the central Zagros. The intense compression between the Arabian shield and central Iran drives the material away from the zone of thickening, in the direction of the strike of shortening. This process is enhanced by larger rheology contrasts, and is best seen when $n = 5$.

4.2 Conclusions

The thin viscous sheet model used in this study, can provide reasonable explanations for many of the tectonic processes involved in the Iranian plateau. The results of the numerical experiments imply that, indeed the deformation of Iran is primarily controlled by the northward convergence of Arabia. Perhaps it is one of the main achievements of this study, to show that the deformation of northern Iran, is the direct result of convergence in the south, and central Iran has a considerable capability in transmitting the deformation from the south to the north. The role of buoyancy forces arising from crustal thickness contrasts is shown to be of importance. However, the effect of buoyancy forces especially in the last stages of the deformation may not be as profound as that in central Asia, suggested by many authors (e.g. England & McKenzie 1982, England & Houseman 1986, Vilotte et al. 1986). The distribution of

instantaneous rate of thickening, shows that the area of maximum vertical deformation even when the lithosphere is too weak, always remains close to the boundary of the Arabian Shield, in the Zagros, and there is no indication of northward shift of this zone into central and northern parts of Iran. This indicates that the Zagros, is still the region of maximum rate of uplift in Iran.

The scales of deformation predicted by the models are in accord with the actual crustal (topography) distribution in Iran. The models show that regardless of the values of the rheological parameters, the extent of the deformation quickly reaches the northern parts of Iran, and crustal thickening takes place over the entire plateau. This indicates that the geometrical configuration of the plateau, has a great influence on the amount of crustal shortening in the north, and perhaps overshadows the effect of rheology.

In the formulation of the thin viscous sheet model, the vertically averaged rheology is presented in the form of two non-dimensional parameters, n and Ar . The numerical models show that for some range of parameters the results of calculations could better approximate the observed crustal deformation. It appears that, while for the homogeneous models highly nonlinear materials ($n \sim 10$) can produce crustal thicknesses that are close to the thickness of the crust in the Zagros, in the heterogeneous cases smaller nonlinearities such as $n = 3$ or $n = 5$ can produce the same amount of crustal thickness. In general, nonlinear materials with $n = 3$ to 10 and Argand number between 1 to less than 10, are preferred.

For the range of parameters selected above, the shear stress sustained by the medium for most heterogeneous models is of the order of 5 MPa for $n = 3$, $Ar = 10$, to 20 MPa for $n = 3$, $Ar = 3$, to 100 MPa for $n = 5$, $Ar = 1$. The typical vertical strain rate is about $5-15 \times 10^{-16} s^{-1}$, and vertical rate of crustal uplift is around 2.5 mmy^{-1} .

The orientations of the principal compressive stress axes calculated from the models are in good agreement with the observed present day axes of compression in

Iran. The models are also successful in describing the tectonic styles in different regions of the plateau. The overall shortening and thickening along the northwest-southeast trending reverse faults are clearly observed, and the absence of any normal faulting in the models is in fair agreement with the observations. Also the development of the shear zones in eastern and northeastern Iran and the low relief topography in central Iran, is explained through the effects of lateral heterogeneities in the strength of the lithosphere.

4.3 Future work

The study of the deformation in Iran can be improved, by applying more sophisticated mechanical formulations. Two dimensional modelling does not account for the vertical variations in stress and material properties, or the kinematic detachment at the base of the crust (Bird 1989). Three dimensional models can provide means to incorporate these features in the calculations. The discussions in the previous chapters showed that more accuracy is achievable, by adding more complexity to the structure of the lithosphere. Therefore by applying more realistic geometries and boundary conditions, more viable results can be obtained. Furthermore, the thermal evolution of the lithosphere as the deformation proceeds, can be evaluated by solving the heat transfer equation. The thermal states can have substantial effects on the rheology of the deeper parts of the crust and the uppermost mantle.

Appendix

Numerical solutions of the equations

The coupled equations (2.18) and (2.20), are solved numerically, using a finite element technique. In the following, after a brief description of the finite element method, the numerical formulation of both equations is presented.

A.1 The finite element method, a general background

The prime conception of the finite element method is to replace a set of differential equations with an equivalent, but approximated, set of algebraic equations, where the unknown variables are evaluated at some specific points. There are several distinct steps which are to be pursued (see Hughes, 1987 for details):

1. The first step is to establish a weak or variational form of the problem, which converts a differential equation to an integral equation. Two sets of functions are characterized in the weak form. The first set called the trial solutions, is to satisfy the velocity boundary conditions. The derivatives of the trial solutions must be square integrable. The second set called the weighting functions, possesses all the properties of the trial solutions except that they vanish on the part of the boundary where the velocity is prescribed. The weak form obtained by multiplying the weighting functions to both sides of the differential equation, and integrating all the terms over the domain, using the divergence theorem to reduce the order of the derivatives of velocity under

the integrals.

2. The second step is to obtain an approximate solution to the weak statement. This process involves discretization of the domain of the problem and constructing finite dimensional approximation for the trial and weighting functions. The resulting equation is known as the "Galerkin approximation" which is an example of the so called weighted residual methods.

3. The next step is to subdivide the region of the analysis into a finite number of appropriately shaped elements, each with a number of nodes. Some or all of the nodes are interconnected to those of the neighbouring elements. The physical variables of the problem (e.g. velocity) are determined at the nodes.

4. The solution to the Galerkin problem is sought by approximating the weighting and trial functions in the elemental level. This is done by some interpolation functions which are smooth in the interior and continuous across the boundaries of the elements, insuring that the integrals are well defined. The interpolation functions are usually simple polynomials, expressed in terms of the value of the variables at the nodes. The polynomial presentation of the weighting function w_i is of the form;

$$w_i = \sum_{A=1}^{N_{node}} N_A v_{iA}, \quad \text{A.1}$$

where N_{node} is the number of nodes in each element, N_A is the polynomial called the shape function which is only position dependent, v_{iA} is the velocity at node A, and the subscript i stands for the ith component of the Cartesian coordinate system. The elemental matrix is constructed by substituting the polynomials in the Galerkin formula. The size of the matrix is $N_{ndof} \times N_{node}$, where N_{ndof} is the degree of freedom of the physical variables at the nodes (e.g. equal to 2 for two dimensional flow problems).

6. The integration is carried out numerically, the Gaussian integration rules are

often used to fulfil this task.

7. Once the elemental matrices are obtained, they have to be assembled to the global matrix. The numbering of the elements should be carried out in a proper way in order to achieve the maximum saving in the computation.

8. The last step is to solve the global matrix for the physical parameters.

A.1.1 Finite element formulation of the force balance equation

Equation (2.18) allows us to make use of a constitutive relation of the form:

$$\sigma_{\alpha\beta} = \eta u_{k,k} \delta_{\alpha\beta} + \eta u_{(\alpha,\beta)} \quad \alpha, \beta = 1, 2, \quad \text{A.2}$$

with effective viscosity and the strain rate tensor as:

$$\eta = \dot{\epsilon}^{(1/n-1)}, \quad \dot{\epsilon}_{\alpha\beta} = u_{(\alpha,\beta)} = \frac{1}{2} \left(\frac{\partial u_\alpha}{\partial x_\beta} + \frac{\partial u_\beta}{\partial x_\alpha} \right), \quad \text{A.3}$$

respectively. Equation (2.18) then can be written in a simpler form:

$$\frac{\partial \sigma_{\alpha\beta}}{\partial x_\beta} = A r s \frac{\partial s}{\partial x_\alpha}, \quad \alpha, \beta = 1, 2 \quad \text{A.4}$$

The weak statement is formulated by multiplying each component of equation (A.4) by components of the weighting function w , and integrating both sides over the domain:

$$\int_{\Omega} w_x \left(\frac{\partial \sigma_{xx}}{\partial x} + \frac{\partial \sigma_{xy}}{\partial y} \right) d\Omega = \int_{\Omega} w_x A r s \frac{\partial s}{\partial x}, \quad \text{A.5}$$

$$\int_{\Omega} w_y \left(\frac{\partial \sigma_{yx}}{\partial x} + \frac{\partial \sigma_{yy}}{\partial y} \right) d\Omega = \int_{\Omega} w_y A r s \frac{\partial s}{\partial y}.$$

Using the divergence theorem to reduce the order of differentiation on the velocity functions yields:

$$\int_{\Omega} \left(\frac{\partial w_x}{\partial x} \sigma_{xx} + \frac{\partial w_x}{\partial y} \sigma_{xy} \right) d\Omega - \int_{\Gamma_h} w_x (\sigma_{xx} n_x + \sigma_{xy} n_y) d\Gamma = - \int_{\Omega} w_x A r s \frac{\partial s}{\partial x} d\Omega, \quad \text{A.6}$$

$$\int_{\Omega} \left(\frac{\partial w_y}{\partial x} \sigma_{yx} + \frac{\partial w_y}{\partial y} \sigma_{yy} \right) d\Omega - \int_{\Gamma_h} w_y (\sigma_{yx} n_x + \sigma_{yy} n_y) d\Gamma = - \int_{\Omega} w_y A r s \frac{\partial s}{\partial y} d\Omega,$$

in which \mathbf{n} is the unit vector normal to the boundary. Substituting for stress from formula (A.2) and discretizing the velocity function as:

$$\begin{aligned} u^h &= v^h + g^h && \in \Omega \\ u^h &= 0 + g^h && \in \Gamma_h \end{aligned} \quad \text{A.7}$$

the x and y components of the Galerkin statement of the problem become:

$$\begin{aligned} &4 \int_{\Omega} \eta \frac{\partial w_x}{\partial x} \frac{\partial v_x}{\partial x} d\Omega + \int_{\Omega} \eta \frac{\partial w_x}{\partial y} \left(\frac{\partial v_x}{\partial y} + \frac{\partial v_y}{\partial x} \right) d\Omega + 2 \int_{\Omega} \eta \frac{\partial w_x}{\partial x} \frac{\partial v_y}{\partial y} d\Omega \\ &= 2 \int_{\Gamma_h} w_x h_x d\Gamma - \int_{\Omega} w_x A r \frac{\partial s^2}{\partial x} d\Omega - 4 \int_{\Omega} \eta \frac{\partial w_x}{\partial x} \frac{\partial g_x}{\partial x} d\Omega \\ &- \int_{\Omega} \eta \frac{\partial w_x}{\partial y} \left(\frac{\partial g_x}{\partial y} + \frac{\partial g_y}{\partial x} \right) d\Omega - 2 \int_{\Omega} \eta \frac{\partial w_x}{\partial x} \frac{\partial g_y}{\partial y} d\Omega, \end{aligned}$$

A.8

$$\begin{aligned} &4 \int_{\Omega} \eta \frac{\partial w_y}{\partial y} \frac{\partial v_y}{\partial y} d\Omega + \int_{\Omega} \eta \frac{\partial w_y}{\partial x} \left(\frac{\partial v_y}{\partial x} + \frac{\partial v_x}{\partial y} \right) d\Omega + 2 \int_{\Omega} \eta \frac{\partial w_y}{\partial y} \frac{\partial v_x}{\partial x} d\Omega \\ &= 2 \int_{\Gamma_h} w_y h_y d\Gamma - \int_{\Omega} w_y A r \frac{\partial s^2}{\partial y} d\Omega - 4 \int_{\Omega} \eta \frac{\partial w_y}{\partial y} \frac{\partial g_y}{\partial y} d\Omega \\ &- \int_{\Omega} \eta \frac{\partial w_y}{\partial x} \left(\frac{\partial g_y}{\partial x} + \frac{\partial g_x}{\partial y} \right) d\Omega - 2 \int_{\Omega} \eta \frac{\partial w_y}{\partial y} \frac{\partial g_x}{\partial x} d\Omega. \end{aligned}$$

The superscript h in formula (A.7) (dropped in equation (A.8) for convenience) refers to the characteristic length of the discretized domain. In equation (A.8) g_i is the i th component of a given function satisfying the velocity boundary condition, and h_x and h_y are components of the prescribed traction at the boundary.

A.1.2 Finite element formulation of the continuity equation

The Lagrangian description of the equation of continuity is as:

$$\frac{Ds}{Dt} = -s \nabla \cdot \mathbf{u} . \quad \text{A.9}$$

The technique of solving this problem is to calculate the unknown function s at time t^{n+1} , from the known values of s and \mathbf{u} at time t^n . The weak form of equation (A.9) is:

$$\int_{\Omega} w \dot{s} d\Omega = - \int_{\Omega} w s \nabla \cdot \mathbf{u} d\Omega , \quad \text{A.10}$$

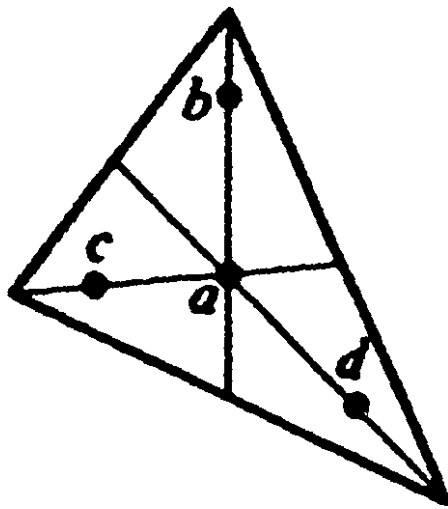
where \dot{s} is the Lagrangian time derivative of s , and w is the set of crustal thickness weighting functions. w , s and \mathbf{u} are represented through the interpolating functions and are known at time t^n . The equation is solved for the time derivative of the crustal thickness at the nodal points, using the same techniques discussed in the previous section. Once \dot{s} is calculated, the crustal thickness at time t^{n+1} is obtained by:

$$\dot{s} = \frac{s^{n+1} - s^n}{\Delta t} . \quad \text{A.11}$$

A.2 Computer programming techniques

The solution domain in Figure 3.1b is divided into 1616 triangular elements, and w , \mathbf{u} , \mathbf{g} and s functions are approximated by bilinear polynomials. All the finite integrals are calculated by Gaussian quadrature rule with four integration points inside the elements (Figure A.1). The accuracy of the results was ascertained by running the computer program with a coarser mesh, and also using interpolating functions of higher orders. In the models involving nonlinearities in the rheology, the velocity field is solved iteratively. A simple iteration scheme is used, where the entries of the global

Figure A.1 A sketch of a triangular element with four integration points.



matrix at each iteration step are calculated from the velocities at the previous step. For a model with $n = 3$, about 8 to 10 iterations were required.

The total time of the deformation is divided to relatively small steps. For the size of time steps, the criterion given by Houseman & England (1986) was used, where the maximum strain in any element at each time step should not exceed 10%, i.e.:

$$\Delta t \left(\left| \frac{\partial u_x}{\partial x} \right| + \left| \frac{\partial u_y}{\partial y} \right| \right)_{max} \leq 10\% . \quad \text{A.12}$$

At each time step, the equation of motion is solved for the velocity field, while crustal thickness is kept unchanged. Once the velocity field is determined, the grid is updated, and the crustal thickness is calculated for the new configuration using the continuity equation. The matrix in the left hand side of equation (A.10) is converted into a lumped mass matrix in order to reduce the computer storage requirements. The structure of the FORTRAN program developed in this study, has been adopted from a finite element code called DLEARN, written by Hughes (1987) for structural mechanics problems. The computer program is given in the following pages.

```

c
c   *** THIN VISCIOUS SHEET MODEL ***
c
c
c   common /bpoint/ mfirst,mlast,mtot,iprec
c   common a(1000000)
c
c   mfirst = 1
c   mtot = 1000000
c   mlast = mtot
c   iprec = 2
c
c   open(8,file='thin.dat')
c   open(9,file='thin.out')
c   open(7,file='thin.vel')
c   open(10,file='thin.crst')
c   open(11,file='thin.xy')
c   open(12,file='thin.plotv')
c   open(13,file='thin.enc')
c
c   call flow
c
c   close(8)
c   close(9)
c   close(7)
c   close(10)
c   close(11)
c   close(12)
c   close(13)
c
c   end
c
c-----
c
c   subroutine flow
c
c... ndof = no. of degrees of freedom   numnp = no. of nodes
c... nsd = no. of dimensions           numel = no. of elements
c...
c... character*4 title,ciaq
c
c   common /bpoint/ mfirst,mlast,mtot,iprec
c   common /colhtc/ neq,neqs
c   common /info / iexec,iptin,nsd,ndof,numnp,nlvect,nlvecs
c   common /spoint/ mpd,mpg,mpx,mps,mpid,mpf,mpdiag,mpngrp,
c   |           mpalhs,mpbrhs,mptim,mpdpre,mpdigs,
c   |           mpalss,mpbrss,mpids,mpeps,mpsdot
c   common /titlec/ title(20)
c   common a(1)
c
c   data ciaq/'*end'/
c
c... input phase
c
c   100 continue
c   read (8,1000) title
c   if (title(1) .eq. ciaq) return
c   read (8,2000) iexec,iptin,nsd,ndof,numnp,nlvect,nlvecs
c   write(9,3000) title,iexec,iptin
c   write(9,4000) nsd,numnp,ndof,nlvect
c
c... initialization phase
c

```

```

      call statin (neq,neqs)
c
c... input initial crustal thicknesses
c
      call crust (a(mps),numnp,iprtin)
c
c... input element data
c
      call elemnt ('input ___',a(mpngpr))
c
c... allocate memory for global equation system
c
      call eqset (neq,neqs,numnp,nalhs,nalss)
c
c... solution phase
c
      if (iexec .eq. 1) call driver (neq,neqs,nalhs)
c
c... print memory pointer dictionary
c
      call prtdc
c
      go to 100
c
1000 format(20a4)
2000 format(10i5)
3000 format('1',20a4//
1' EXECUTION CONTROL INFORMATION '//5x.
1' EXECUTION CODE ..... (IEXEC ) = ',i5//5x.
1' EQ. 0, DATA CHECK           ', /5x.
1' EQ. 1, EXECUTION             ', //5x.
1' INPUT DATA PRINT CODE ..... (IPRTIN) = ',i5//5x.
1' EQ. 0, PRINT NODAL AND ELEMENT INPUT DATA ', /5x.
1' EQ. 1, DO NOT PRINT NODAL AND ELEMENT INPUT DATA ', /5x)
4000 format(5x.
1' NUMBER OF SPACE DIMENSIONS ..... (NSD ) = ',i5//5x.
1' NUMBER OF NODAL POINTS ..... (NUMNP ) = ',i5//5x.
1' NUMBER OF NODAL DEGREES OF FREEDOM .... (NDOF ) = ',i5//5x.
1' NUMBER OF LOAD VECTORS ..... (NLVECT) = ',i5//5x)
c
      end
-----
c
c      subroutine addlhs (alhs,elefsm,idiag,lm,nec)
c
c... program to add element stiffness matrix to global matrix
c
      implicit double precision (a-h,o-z)
      dimension alhs(1),elefsm(nec,1),idiag(1),lm(1)
c
      do 200 j=1,nec
      k = lm(j)
      if (k .gt. 0) then
      do 100 i=1,j
      m = lm(i)
      if (m .gt. 0) then
      if (k .ge. m) then
      l = idiag(k) - k + m
      else
      l = idiag(m) - m + k
      endif
      alhs(l) = alhs(l) + elefsm(i,j)
      endif
      enddo
      enddo

```

```

100 continue
endif
200 continue
c
return
end
-----
c
subroutine adlhrs (alhss,eles,lms,nen)
c
implicit double precision (a-h,o-z)
dimension alhss(1),eles(1),lms(1)
c
do 100 i = 1,nen
k = lms(i)
if(k .gt. 0) alhss(k) = alhss(k) + eles(i)
100 continue
c
return
end
-----
c
subroutine addrhs (brhs,elresf,lm,nec)
c
c... program to add element residual force vector to r.h.s vector
c
implicit double precision (a-h,o-z)
dimension brhs(1),elresf(1),lm(1)
c
do 100 j = 1,nec
k = lm(j)
if (k .gt. 0) brhs(k) = brhs(k) + elresf(j)
100 continue
c
return
end
-----
c
subroutine adrhss (brhss,elrhs,lm,nen)
c
c... program to add element residual force vector to r.h.s vector
c
implicit double precision (a-h,o-z)
dimension brhss(1),elrhs(1),lm(1)
c
do 100 j=1,nen
k = lm(j)
if (k .gt. 0) brhss(k) = brhss(k) + elrhs(j)
100 continue
c
return
end
-----
c
subroutine adtime (time)
c
c... program to calculate total elapsed time
c
implicit double precision (a-h,o-z)
dimension time (1)
c
time(2) = time(2) + time(1)
write(*,1000) 2.5*time(2)

```

```

c
  return
1000 format('elapsed time ',17.4,' Ma')
end
-----
c
  subroutine back (a,b,idiag,neq)
c
c... program to perform forward reduction and back substitution
c
  implicit double precision (a-h,o-z)
  dimension a(1),b(1),idiag(1)
c
c... forward reduction
c
  jj = 0
  do 100 j=1,neq
  jjlast = jj
  jj = idiag(j)
  jcolht = jj - jjlast
  if (jcolht .gt. 1)
  b(j) = b(j) - cprod(a(jjlast+1),b(j-jcolht+1),jcolht-1)
100 continue
c
c... diagonal scaling
c
  do 200 j=1,neq
  a(j) = a(idiag(j))
  if (a(j) .ne. 0.0) b(j) = b(j)/a(j)
200 continue
c
c... back substitution
c
  if (neq .eq. 1) return
  jjnext = idiag(neq)
  do 400 j=neq,2,-1
  jj = jjnext
  jjnext = idiag(j-1)
  jcolht = jj - jjnext
  if (jcolht .gt. 1) then
  bj = b(j)
  istory = j - jcolht + 1
  jtemp = jjnext - istory + 1
  do 300 i=istory,j-1
  b(i) = b(i) -a(jtemp+i)*bj
300 continue
  endif
400 continue
c
  return
end
-----
c
  subroutine bond (id,ids,ndof,numnp,neq,neqs,iprtin)
c
c... program to read and generate boundary condition data and
c... establish equation numbers
c
c... n = number of first node in sequence
c... ne = number of last node in sequence
c... ng = generation increment
c... ib(ndof,n) = d.o.f ndof boundary code for node n, 1 = specified
c... velocity, 0 = unspecified velocity

```

```

c
dimension id(ndof,1),ids(1,ib(3))
logical pflag
c
call iclear (id,ndof*numnp)
call iclear (ids,numnp)
c
100 continue
read(8,1000) n,ne,ng,(ib(i), i=1,ndof)
if (n .eq. 0) go to 50
if (ng .eq. 0) then
ne = n
ng = 1
else
ne = ne - mod(ne-n,ng)
end if
c
do 200 i = n,ne,ng
call imove (id(1,i),ib,ndof)
200 continue
go to 100
c
c... read s boundary condition data
c
50 continue
read(8,1000) n,ne,ng,ib(1)
if (n .eq. 0) go to 70
if (ng .eq. 0) then
ne = n
ng = 1
else
ne = ne - mod(ne-n,ng)
end if
c
do 250 i = n,ne,ng
call imove (ids(i),ib,1)
250 continue
go to 50
c
70 if (iptin .eq. 0) then
nn = 0
do 400 n = 1,numnp
pflag = .false.
c
do 300 i = 1,ndof
if (id(i,n) .ne. 0) pflag = .true.
300 continue
c
if (pflag) then
nn = nn + 1
if (mod(nn,50) .eq. 1) write(9,2000) (i,i=1,ndof)
write(9,3000) n,(id(i,n),i=1,ndof)
endif
400 continue
endif
c
c... establish equation numbers
c
neq = 0
do 600 n = 1,numnp
do 500 i = 1,ndof
if (id(i,n) .eq. 0) then
neq = neq + 1

```

```

        idf(i,n) = neq
        else
        idf(i,n) = 0
        endif
500 continue
600 continue
c
        neqs = 0
        do 650 n = 1,numnp
        if (ids(n) .eq. 0) then
        neqs = neqs + 1
        ids(n) = neqs
        else
        ids(n) = 0
        endif
650 continue
c
        return
1000 format(6i5)
2000 format('1', ' NODAL BOUNDARY CONDITION
           IC O D E S '///5x, ' NODE NO.',3x,6(6x,'Dof',i1:)//)
3000 format(6x,i5,5x,6(5x,i5))
c
        end
-----
c
        subroutine btdb (stiff,b,db,nec,nrowb,nstr)
c
c... program to multiply B(T)*DB, taking account of symmetry
c... and accumulate into element stiffness matrix
c
        implicit double precision (a-h,o-z)
        dimension stiff(nec,1),b(nrowb,1),db(nrowb,1)
c
        do 200 j=1,nec
        do 100 i=1,nec
        stiff(i,j) = stiff(i,j) + coldot(b(1,i),db(1,j),nstr)
100 continue
200 continue
c
        return
        end
-----
c
        subroutine clear (a,m)
c
c... program to clear a floating point array
c
        implicit double precision (a-h,o-z)
        dimension a(1)
c
        do 100 i=1,m
        a(i) = 0.0
100 continue
c
        return
        end
-----
c
        function coldot (a,b,n)
c
c... program to compute dot product of vectors stored column-wise
c

```

```

        implicit double precision (a-h,o-z)
        dimension a(1),b(1)
c
        coldot = 0.0
        do 100 i=1,n
            coldot = coldot + a(i)*b(i)
100 continue
c
        return
        end
c-----
c
        subroutine colht (idiag,lm,ned,nen,numel)
c
c... program to compute column heights in global left hand side matrix
c
        dimension idiag(1),lm(ned,nen,1)
        common /colhtc/ neq,neqs
c
        do 500 k=1,numel
            min = neq
            do 200 j=1,nen
                do 100 i=1,ned
                    num = lm(i,j,k)
                    if (num .gt. 0) min = min0(min,num)
100 continue
200 continue
                do 400 j=1,nen
                    do 300 i=1,ned
                        num = lm(i,j,k)
                        if (num .gt. 0) then
                            m = num - min
                            if (m .gt. idiag(num)) idiag(num) = m
                        endif
300 continue
400 continue
500 continue
c
            return
            end
c-----
c
        subroutine compar (d,dpre,flg,ndof,numnp)
c
c... program to calculate '(d - dpre)/d'
c
        implicit double precision (a-h,o-z)
        dimension d(ndof,1),dpre(ndof,1)
        logical flg
c
        flg = .true.
        p = 0.0
        do 200 j = 1,numnp
            do 100 i = 1,ndof
                if (dpre(i,j) .eq. 0.) go to 100
                relerr = abs((d(i,j) - dpre(i,j))/d(i,j))
                if (relerr .gt. p) p = relerr
100 continue
200 continue
            if (relerr .lt. .01) flg = .false.
c
        return
        end

```

```

-----
c
c  subroutine compbc (id,ids,d,eps,g,f,ndof,numnp,nlvect,nlvees)
c
c... program to compute velocity boundary conditions
c
c  implicit double precision (a-h,o-z)
c  dimension id(ndof,1),ids(1),d(ndof,1),g(ndof,1),eps(1),
c  1      f(ndof,numnp,1)
c
c  ntot = nlvect + nlvees
c  do 400 i = 1,ndof
c  do 300 j = 1,numnp
c  k = id(i,j)
c  if (k .gt. 0) go to 200
c  val = 0.0
c  do 100 lv = 1,nlvect
c  val = val + f(i,j,lv)
c 100 continue
c  d(i,j) = val
c  g(i,j) = val
c 200 continue
c 300 continue
c 400 continue
c
c  do 500 j = 1,numnp
c  k = ids(j)
c  if (k .gt. 0) go to 600
c  val = 0.0
c  do 700 lv = nlvect + 1,ntot
c  val = val + f(1,j,lv)
c 700 continue
c  eps(j) = val
c 600 continue
c 500 continue
c
c  return
c  end
-----
c
c  subroutine crust(s,numnp,iprtin)
c
c... program to store initial crustal thicknesses
c
c  implicit double precision (a-h,o-z)
c  dimension s(1)
c
c  do 100 i = 1,numnp
c  s(i) = .35
c 100 continue
c
c  if(iprtin .eq. 0) write(9,1000) s(1)*100.
c
c  return
c 1000 format(//, ' INITIAL CRUSTAL THICKNESS = ',f6.2,' Km')
c  end
-----
c
c  subroutine detnry (name,ndim1,ndim2,ndim3,mpoint,ipr,mlast)
c
c... program to store pointer information in dictionary
c
c  dimension name(2)

```

```

common ia(1)
c
mlast = mlast - 7
ia(mlast+1) = name(1)
ia(mlast+2) = name(2)
ia(mlast+3) = mpoint
ia(mlast+4) = ndim1
ia(mlast+5) = ndim2
ia(mlast+6) = ndim3
ia(mlast+7) = ipr
c
return
end
c-----
c
subroutine dettim (time,flim)
c
c... program to compare the total time with elapsed time
c
implicit double precision (a-h,o-z)
dimension time(1)
logical flim
c
flim = .true.
if (time(2) .ge. time(3)) flim = .false.
c
return
end
c-----
c
subroutine diag (idiag,neq,n)
c
c... program to compute diagonal addresses of left hand side matrix
c
dimension idiag(1)
c
n = 1
idiag(1) = 1
if (neq .eq. 1) return
do 100 i = 2,neq
idiag(i) = idiag(i-1) + 1
100 continue
n = idiag(neq)
c
return
end
c-----
c
subroutine driver(neq,neqs,nalhs)
c
c... solution driver program
c
logical flg,flim
character*1 ans
common /info / iexec,iprtin,nsd,ndof,numnp,nlvec,nlvecs
common /spoint/ mpd,mpg,mpx,mps,mpid,mpf,mpdiag,mpngrp,
1 mpalhs,mpbrhs,mptim,mpdpre,mpdigs,
1 mpalss,mpbrss,mpids,mpeps,mpsdot
common a(1)
ians = 2
c
c
c-----

```



```

      call iterup (a(mpid),a(mpd),a(mpbrs),ndof,numnp)
c
      if (ians .eq. 1) then
      print*,iter,'th iteration completed'
      iter = iter + 1
c
c... compare the velocities with the previous ones
c
      call compar (a(mpd),a(mpdpre),flg,ndof,numnp)
      if (.not. flg) go to 101
      end if
c
      if (ians .eq. 1) go to 100
c
c .....
c
c          EQUATION OF CONTINUITY
c
c... determine the time interval
c
      101 continue
c
      call elemnt ('det_time',a(mpngrp))
c
c... update the grid
c
      call update (a(mpx),a(mpd),a(mptim),nsd,ndof,numnp)
c
c... add the last time interval to the total time
c
      call adtime (a(mptim))
c
c... solve the continuity equation
c
      call clear (a(mpalss),neqs)
      call clear (a(mpbrss),neqs)
      call elemnt ('solv_con',a(mpngrp))
      call solves (a(mpalss),a(mpbrss),a(mpeps),neqs)
      call expo (a(mps),a(mpids),a(mpbrss),a(mpsdot),a(mptim),numnp)
c
      print*, '          ',.itime,'th time step completed'
c
c... decide wether to stop the time stepping or not
c
      call dettim (a(mptim),flim)
      if (.not. flim) go to 300
      itime = itime + 1
      go to 200
c
c... write crustal thickness and velocity data
c
      300 continue
      call printc (a(mps),numnp)
      call printv (a(mpd),a(mptim),ndof,numnp)
c
      return
      end
c-----
c
c      subroutine clear (npar)
c
c... program to read element control card
c

```

```

dimension npar(1)
c
read(8,1000) (npar(i), i = 1,3)
write(9,2000)
c
return
1000 format(16i5)
2000 format('1'///' E L E M E N T   D A T A   '///)
end
-----
c
subroutine elemnt (task,ngrp)
c
c... program to calculate element task number
c
character*8 task,eltask(6)
dimension ngrp(1)
c
common /info / iexec,iprtin,nsd,ndof,numnp,nlvect,nlvees
common ia(1)
data ntask,eltask/5,'input___','form_lhs','form_rhs',
1 'det_time','solv_con'/
c
do 100 i=1,ntask
if (task .eq. eltask(i)) itask = i
100 continue
c
if (itask .eq. 1) then
mpnpar = mpoint('npar' ,16,0,0,1)
ngrp(1) = mpnpar
call elcard (ia(mpnpar))
else
mpnpar = ngrp(1)
endif
call elmlib (mpnpar,itask)
c
return
end
-----
c
subroutine elmlib (mpnpar,itask)
c
c... program to call element routines
c
common a(1)
c
call quade (itask,a(mpnpar),a(mpnpar+16))
c
return
end
-----
c
subroutine eqset (neq,neqs,numnp,nalhs,nalss)
c
c... program to allocate storage for global equation system
c
character*4 title
common /bpoint/ mfirst,mlast,mtot,iprec
common /spoint/ mpd,mpg,mpx,mps,mpid,mpf,mpdiag,mpngrp,
1 mpalle,mpbrhs,mptim,mpdpre,mpdigs,
1 mpalss,mpbrss,mpids,mpeps,mpedot
common /title/ title(20)
common a(1)

```

```

c
c... determine addresses of diagonals in left hand side matrix
c
  call diag (a(mpdia),neq,nalhs)
  mpalhs = mpoint('alhs' ,nalhs,0,0,iprec)
  mpbrhs = mpoint('brhs' ,neq ,0,0,iprec)
  mpalss = mpoint('alhss' ,neqs,0,0,iprec)
  mpbrss = mpoint('brhss' ,neqs,0,0,iprec)
  meanbw = nalhs/neq
  nwords = mtot - mlast + mfirst - 1
c
c... write equation system data
c
  write(9,1000) title,neq,nalhs,meanbw,nwords
c
  return
1000 format('1',20a4///
1' EQUATION SYSTEM DATA          ', //5x,
1' NUMBER OF EQUATIONS ..... (NEQ ) = ', //5x,
1' NUMBER OF TERMS IN LEFT HAND SIDE MATRIX (NALHS ) ', //5x,
1' MEAN HALF BANDWIDTH ..... (MEANBW) = ', //5x,
1' TOTAL LENGTH OF BLANK COMMON REQUIRED . (NWORDS) = ', //5x,
end
c-----
c
c  subroutine expo (s,ids,brss,sdot,time,numnp)
c
c... program to calculate s from ds/dt (eps) at nodes
c
  implicit double precision (a-h,o-z)
  dimension s(1),ids(1),sdot(1),brss(1),time(1)
c
  do 100 i = 1,numnp
    k = ids(i)
    if (k .gt. 0) sdot(i) = brss(k)
  100 continue
c
  do 200 i = 1,numnp
    s(i) = time(1)*sdot(i) + s(i)
  200 continue
c
  return
  end
c-----
c
c  subroutine factor (a,idiag,neq)
c
c... program to perform Crout factorization on a,  $A = U(T)*D*U$ 
c
  implicit double precision (a-h,o-z)
  dimension a(1),idiag(1)
c
  jj = 0
  do 300 j=1,neq
    jjlast = jj
    jj = idiag(j)
    jcolht = jj - jjlast
c
    if (jcolht .gt. 2) then
c
c... for column j and i .le. j-1, replace a(i,j) with d(i,i)*u(i,j)
c
      istart = j - jcolht + 2

```

```

      m1 = i + 1
      n = jlast + 2
      n = ndat(i-start+1)
      do 100 i = start,m1
      nlast = n
      n = idiat(i)
      jcolht = n - nlast
      jlength = i - i-start + 1
      length = min0(jcolht+1,jlength)
      if (length .gt. 0)
      l a(i) = a(i) + coldot(a(i-length),a(i-length),length)
      ij = ij + 1
100 continue
      endif
c
      if (jcolht .ge. 2) then
c
c... form column j and i .ie. j-1, replace a(i,j) with u(i,j)
c
      jtemp = j - ij
      do 200 ij = jlast + 1, ij - 1
      ii = idiat(jtemp+ij)
      if (a(ii) .ne. 0.0) then
      temp = a(ij)
      a(ij) = temp*a(ii)
      a(ii) = temp*a(ij)
      endif
200 continue
      endif
300 continue
c
      return
      end
-----
c
c
c... subroutine formlm (id,ids,ien,lm,lms,ndof,ned,nen,numel)
c
c... program to form the elemental 'LM' array
c... lm(ned,nen,1) = location matrix
c
c
c... dimension id(ndof,1), ien(nen,1), lm(ned,nen,1),ids(1),
c... l lms(nen,1)
c
c
c... do 300 k=1,numel
c... do 200 j=1,nen
c... node = ien(j,k)
c... lms(j,k) = ids(node)
c... do 100 i=1,ndof
c... lm(i,j,k) = id(i,node)
100 continue
200 continue
300 continue
c
      return
      end
-----
c
c
c... subroutine frmien(jen,nen,numel)
c
c... program to construct 'IEN' array
c
c... ien(nen,numel) = element nodes array
c... numel = number of elements

```

```

c
  implicit double precision (a-h,o-z)
  dimension ien(nen,1)
c
  do 100 i = 1,numel
    read (15,1000) k,(ien(j,i), j = 1,nen)
  100 continue
  return
c
  1000 format(4i5)
  end
-----
c
c
  subroutine genel (ien,mat,nen,numel,numat)
c
c... program to generate element nodes and material numbers
c... ien(nen,numel) = element node numbers
c... mat(numel) = element material numbers
c
  dimension ien(nen,1),mat(1)
c
  call frmien (ien,nen,numel)
c
  do 100 n=1,numel
    mat(n) = 1
  100 continue
  if (numat .eq. 1) return
c
  200 continue
  read(8,1000) nfirst,nlast,matnum:
  if(nfirst .eq. 0) return
c
  do 300 j = nfirst,nlast
    mat(j) = matnum
  300 continue
  go to 200
c
  1000 format(3i5)
  end
-----
c
c
  subroutine genfl (a,nra)
c
c... program to read and generate floating point nodal data
c... a      = input array
c... nra    = number of rows in a
c... n      = node number
c... numgp  = number of generation points
c... ninc(i) = number of increments for direction i
c... inc(i) = increment for direction i
c
  implicit double precision (a-h,o-z)
  dimension a(nra,1),temp(6,20),ninc(2),inc(2),sh(20)
c
  read(8,*) n,numgp,(temp(i,1), i=1,nra)
  if (n .eq. 0) return
c
  call move (a(1,n),temp,nra)
c
  if (numgp .ne. 0) then
    do 100 j = 2,numgp
      read(8,*) m,mgen,(temp(i,j), i=1,nra)
      if (mgen .ne. 0) call move (temp(1,j),a(1,m),nra)
    100 continue
  end if

```

```

100 continue
c
  read(8,2000) (ninc(i),inc(i), i = 1,2)
c
c... iopt = 1, generation along a line
c          2, generation along a surface
c
  iopt = 2
  if (ninc(2) .eq. 0) iopt = 1
c
  dr = 0.0
  ds = 0.0
c
  if (ninc(1) .ne. 0) dr = 2.0/ninc(1)
  if (ninc(2) .ne. 0) ds = 2.0/ninc(2)
c
  ii = ninc(1) + 1
  jj = ninc(2) + 1
c
  ni = a
  nj = n
c
  s = -1.0
  do 300 j = 1, jj
  r = -1.0
  do 200 i = 1, ii
  call gensh (r,s,sh,numgp,iopt)
  call multab (temp,sh,a(1,ni),6,20,nra,numgp,nra,1,1)
  ni = ni + inc(1)
  r = r + dr
200 continue
  nj = nj + inc(2)
  ni = nj
  s = s + ds
300 continue
c
  endif
  return
c
1000 format(2i5,6f10.0)
2000 format(16i5)
c
  end
-----
c
c
  subroutine gensh (r,s,sh,numgp,iopt)
c
c... program to call shape function routine for isoparametric
c... generation
c
  implicit double precision (a-h,o-z)
  dimension sh(1)
c
  go to (100,200),iopt
c
  100 call gensh1 (r,s,sh,numgp)
  return
  200 call gensh2 (r,s,sh,numgp)
  return
c
  end
-----
c

```

```

subroutine gensh1 (r,sh,n)
c
c... program to compute 1D shape functions for isoparametric
c... generation
c
implicit double precision (a-h,o-z)
dimension sh(1)
c
sh(2) = 0.5*r
sh(1) = 0.5 - sh(2)
sh(2) = 0.5 + sh(2)
  (n .eq. 3) then
sh(3) = 1.0 - r**2
sh(1) = sh(1) - 0.5*sh(3)
sh(2) = sh(2) - 0.5*sh(3)
endif
c
return
end
-----
c
subroutine gensh2 (r,s,sh,n)
c
c... program to compute 2D shape functions for isoparametric
c... generation
c
implicit double precision (a-h,o-z)
dimension sh(1)
c
r2 = 0.5*r
r1 = 0.5 - r2
r2 = 0.5 + r2
s2 = 0.5*s
s1 = 0.5 - s2
s2 = 0.5 + s2
sh(1) = r1*s1
sh(2) = r2*s1
sh(3) = r2*s2
sh(4) = r1*s2
if (n .eq. 4) return
c
r3 = 1.0 - r**2
s3 = 1.0 - s**2
sh(5) = r3*s1
sh(6) = s3*r2
sh(7) = r3*s2
sh(8) = s3*r1
sh(1) = sh(1) - 0.5*(sh(5) + sh(8))
sh(2) = sh(2) - 0.5*(sh(6) + sh(5))
sh(3) = sh(3) - 0.5*(sh(7) + sh(6))
sh(4) = sh(4) - 0.5*(sh(8) + sh(7))
c
return
end
-----
c
subroutine grid (x,nsd,numnp,iprtin)
c
c... program to construct a rectangular grid
c
c... nsd = number of space dimensions
c... numnp = number of nodes in the grid
c... x(nsd,numnp) = nodal coordinate array

```

```

c
  implicit double precision (a-h,o-z)
  dimension x(nsd,1)
c
c... read grid parameters
c
  do 100 i = 1,numnp
    read(11,*) k,x(1,i),x(2,i)
  100 continue
c
  if (iprtin .eq. 1) return
  do 200 n = 1,numnp
    if (mod(n,50) .eq. 1) write(9,3000) (i, i = 1,nsd)
    write(9,4000) n,(x(i,n), i = 1,nsd)
  200 continue
c
  return
1000 format(2f10.5)
2000 format(i5,f10.4,f10.4)
3000 format('1,' NODAL COORDINATE DATA '//5x,
  1' NODE NO.',2(13x,' x',i1,';')//)
4000 format(6x,i5,6x,2(f15.3,1x))
  end
-----
c
  subroutine iclear (ia,m)
c
c... program to clear an integer array
c
  dimension ia(1)
c
  do 100 i=1,m
    ia(i) = 0
  100 continue
c
  return
  end
-----
c
  subroutine imove (ia,ib,n)
c
c... program to move an integer array
c
  dimension ia(1),ib(1)
c
  do 100 i=1,n
    ia(i) = ib(i)
  100 continue
c
  return
  end
-----
c
  subroutine intial (d,id,ndof,numnp)
c
c... program to input initial velocities
c
  implicit double precision (a-h,o-z)
  dimension d(ndof,1),id(ndof,1)
c
c... read the initial value
c
  print*, 'Input "Guess", the initial velocity'

```

```

      read(*,*) guess
c
      del = 0.
      do 200 j = 1,numnp
      do 100 i = 1,ndof
      if (id(i,j) .ne. 0) d(i,j) = guess + del
      del = del + .00001
      100 continue
      200 continue
c
      return
      end
c-----
c
      subroutine input (f,ndof,numnp,j,nlvect,nlvees,iprtin)
c
c... program to read, generate and write nodal input data
c... f(ndof,numnp,nlvect) = prescribed forces/ kinematic data, j = 0
c...      = initial velocities, j = 1
c
      implicit double precision (a-h,o-z)
      logical lzero
      dimension f(ndof,numnp,1)
c
      ntot = nlvect + nlvees
      call clear (f,ntot*numnp*ndof)
c
      do 100 nlv=1,nlvect
      call genf (f(1,1,nlv),ndof)
      call ztest (f(1,1,nlv),ndof*numnp,lzero)
c
      100 continue
c
      do 200 nlv = nlvect + 1,ntot
      call genf (f(1,1,nlv),1)
      200 continue
c
      return
      end
c-----
c
      subroutine iterup (id,d,brhs,ndof,numnp)
c
c... program to move the nodal velocities to 'D' array
c
      implicit double precision (a-h,o-z)
      dimension id(ndof,1),d(ndof,1),brhs(1)
c
      do 200 i=1,ndof
      do 100 j=1,numnp
      k = id(i,j)
      if (k .gt. 0) d(i,j) = brhs(k)
      100 continue
      200 continue
c
      return
      end
c-----
c
      subroutine local (ien,x,nl,nen,nrowx,nrowxl)
c
c... program to localize a global array
c

```

```

        implicit double precision (a-h,o-z)
        dimension ien(1),x(nrowx,1),xl(nrowxl,1)
c
        do 200 j = 1,nen
            node = ien(j)
            do 100 i = 1,nrowx:l
                x(i,j) = x(i,node)
            100 continue
        200 continue
c
        return
        end
-----
c
        subroutine local1 (ien,x,xl,nen)
c
c... program to localize a global array
c
        implicit double precision (a-h,o-z)
        dimension ien(1),x(1),xl(1)
c
        do 100 j = 1,nen
            node = ien(j)
            xl(j) = x(node)
        100 continue
c
        return
        end
-----
c
        subroutine matadd (a,b,c,ma,mb,mc,m,n,iopt)
c
c... program to add rectangular matrices
c
        implicit double precision (a-h,o-z)
        dimension a(ma,1),b(mb,1),c(mc,1)
c
        go to (1000,2000,3000),iopt
c
c... iopt = 1, add entire matrices
c
        1000 do 1200 j=1,n
            do 1100 i=1,m
                c(i,j) = a(i,j) + b(i,j)
            1100 continue
        1200 continue
        return
c
c... iopt = 2, add lower triangular and diagonal matrices
c
        2000 do 2200 j=1,n
            do 2100 i=j,m
                c(i,j) = a(i,j) + b(i,j)
            2100 continue
        2200 continue
        return
c
c... iopt = 3, add upper triangular and diagonal elements
c
        3000 do 3200 j=1,n
            do 3100 i=1,j
                c(i,j) = a(i,j) + b(i,j)
            3100 continue

```

```

3200 continue
    return
c
    end
c-----
c
    subroutine move (a,b,n)
c
c... program to move a floating point array
c
    implicit double precision (a-h,o-z)
    dimension a(1),b(1)
c
    do 100 i=1,n
    a(i) = b(i)
100 continue
c
    return
    end
c-----
c
    function mpoint (name,ndim1,ndim2,ndim3,ipr)
c
c... program to calculate storage pointer
c
    dimension name(2)
    common /bpoint/ mfirst,mlast,mtot,iprec
c
    mpoint = mfirst
    if (iprec .eq. 2 .and. mod(mpoint,2) .eq. 0) mpoint = mpoint + 1
    call detnry (name,ndim1,ndim2,ndim3,mpoint,ipr,mlast)
    mfirst = mpoint + ndim1*max0(1,ndim2)*max0(1,ndim3)*ipr
    if (mfirst .ge. mlast) call serror (name,mfirst-mlast)
c
    return
    end
c-----
c
    subroutine multab (a,b,c,ma,mb,mc,l,m,n,iopt)
c
c... program to multiply two matrices
c... l = range of dot-product index
c... m = number of active rows in C
c... n = number of active columns in C
c
    implicit double precision (a-h,o-z)
    dimension a(ma,l),b(mb,l),c(mc,l)
c
    go to (1000,2000,3000,4000),iopt
c
c... iopt = 1    c = a*b
c
1000 do 1200 i=1,m
    do 1100 j=1,n
    c(i,j) = rcdot(a(i,l),b(l,j),ma,l)
1100 continue
1200 continue
    return
c
c... iopt = 2    c = a(t)*b
c
2000 do 2200 i=1,m
    do 2100 j=1,n

```

```

      c(i,j) = coldot(a(1,i),b(1,j),1)
2100 continue
2200 continue
      return
c
c... iopt = 3      c = a*b(t)
c
3000 do 3200 i = 1,m
      do 3100 j = 1,n
        c(i,j) = rowdot(a(i,1),b(j,1),ma,mb,1)
3100 continue
3200 continue
      return
c
c... iopt = 4      c = a(t)*b(t)
c
4000 do 4200 i = 1,m
      do 4100 j = 1,n
        c(i,j) = redot(b(j,1),a(1,i),mb,1)
4100 continue
4200 continue
c
      return
end
-----
c
c      subroutine prin1 (s,p)
c
c... program to calculate principal values
c
c      implicit double precision (a-h,o-z)
c      dimension s(1),p(1)
c
c      x = 0.5*(s(1) + s(2))
c      y = 0.5*(s(1) - s(2))
c      r = sqrt(y**2 + s(3)**2)
c      p(1) = x + r
c      p(2) = x - r
c
c      return
c      end
-----
c
c      subroutine printe(s,numnp)
c
c... program to print crustal thicknesses
c
c      implicit double precision (a-h,o-z)
c      dimension s(1)
c
c      do 100 n=1,numnp
c      if (mod(n,50) .eq. 1) write(9,1000)
c      write(9,2000) n,s(n)*100.
100 continue
c
c      return
1000 format('1'/' CRUSTAL THICKNESSES'//
1' NODE NO. THICKNESS'//5x)
2000 format(1x,i5.4x,f17.8)
c      end
-----
c
c      subroutine printv(a,time,ndof,numnp)

```

```

c
c... program to print crustal thicknesses
c
c   implicit double precision (a-h,o-z)
c   dimension a(ndof,1),time(2)
c
c   t = time(2)*2.5
c   write (9,1000) t
c   do 100 n=1,numnp
c     if (mod(n,50) .eq. 1) write(9,2000)
c     write(9,3000) n,(a(i,n), i = 1,ndof)
c   100 continue
c
c   return
c   1000 format('1'// 'TIME : ',f5.2,' MILLION YEARS')
c   2000 format('/' VELOCITIES'//
c     1' NODE NO.      DOF1      DOF2'//)
c   3000 format(1x,i5.5x,2(15.8,2x))
c   end
-----
c
c   subroutine prt1el (mat,ien,nen,numel)
c
c... program to print data for element with "nen" nodes
c
c   dimension mat(1),ien(nen,1)
c
c   do 100 n=1,numel
c     if (mod(n,50) .eq. 1) write(9,1000) (i, i=1,nen)
c     write (9,2000) n,mat(n),(ien(i,n), i=1,nen)
c   100 continue
c
c   return
c   1000 format('1'//
c     1' ELEMENT DATA '//5x,
c
c     1' ELEMENT MATERIAL',6(' NODE ',i1,':2x),/5x,
c     1' NUMBER NUMBER'//)
c   2000 format(6x,i5.7(5x,i5))
c   end
-----
c
c   subroutine prop2d (ar,numat)
c
c... program to read, write and store material properties
c
c   implicit double precision (a-h,o-z)
c   dimension ar(1)
c
c   do 100 n=1,numat
c     if (mod(n,50) .eq. 1) write(9,1000) numat
c
c... read & write viscosities
c
c   read(8,*) m,ar(m)
c   write(9,3000) m,ar(m)
c   100 continue
c
c   return
c   1000 format('1'// ' MATERIAL SET DATA      '//5x,
c     1'   NUMBER OF MATERIAL SETS . . . . . (NUMAT) = ',i5
c     1///.7x,'SET'.5x,'ARGAND NUMBER'//)
c   3000 format(5x,i5.5x,1pe10.4)

```

```

end
-----
c
c  subroutine prtac
c... program to print memory pointer dictionary
c
c  common/hpoint/mfirst,mlast,mtot,iprec
c  common ia(1)
c
c  n  (mtot - mlast)/7
c  j  mtot + 1
c
c  do 100 i 1,n
c  il(mod(i,50) .eq. 1) write (9,1000)
c  j  j - 7
c
c  call prtde1(i,ia(j),ia(j+2),ia(j+3),ia(j+4),ia(j+5),ia(j+6))
100 continue
c
c  return
1000 format('1'//
'1' DYNAMIC STORAGE ALLOCATION', ' INFORMATION'//
112X,'ARRAY NO.', 5X, 'ARRAY' , 8X, 'ADDRESS' ,6X, 'DIM1' ,6X,
1'DIM2' ,6X,'DIM3',6X,'PREC.' //)
end
-----
c
c  subroutine prtde1 (i,iname,iadd,ndim1,ndim2,ndim3,ipr)
c... program to print memory pointer information for an array
c
c  dimension iname(2)
c  save neg
c  data nelpar,lefths/'npar', 'alhs'/
c  if (i .eq. 1) neg = 1
c  if (iname(1) .eq. nelpar) then
c  write(9,1000) neg
c  neg = neg + 1
c  endif
c  if (iname(1) .eq. lefths) write(9,2000)
c  write(9,3000) i,iname,iadd,ndim1,ndim2,ndim3,ipr
c
c  return
1000 format(/14X,'*****',7X,'BEGIN ELEMENT GROUP NUMBER',i5/' ')
2000 format(/14X,'*****',7X,'END ELEMENT GROUP DATA'/' ')
3000 format(14X,i5,7X,2a4,1X,6i10)
end
-----
c
c  subroutine prs2d (xint,stress,strain,nn,nnntot,nel,lint)
c... program to print stress and strain rates
c
c  implicit double precision (a-h,o-z)
c  dimension xint(2),stress(3),strain(3)
c
c  nn = nn + 1
c  if (mod(nn,nnntot) .eq. 1) write(9,1000)
c  write(9,2000) nel,lint,xint,stress,strain
c
c  return
1000 format('1'//

```

```

1* ELEMENT STRESSES & STRAIN RATES
1*
1* ELEMENT INT. PT.      N1      N2      1,5X,
1* STRESS  STRESS  STRESS  1, 1, 1,5X,
1* NUMBER  NUMBER
1*      11      22      12      1,49X,
1* ST. RATE ST. RATE ST. RATE 1,49X,
1*      11      22      12*)
2000 format(/2X,i5.6X,i2.8X,2(1X,1pe11.4),5X,3(1pe12.4) 52X,3(1pe12.4))
end

```

```

c-----
c
c  subroutine qdeb (shg,b,nrowsh,nrowb,nen)
c
c... program to set up the strain rate velocity matrix "b"
c
c  implicit double precision (a-h,o-z)
c  dimension shg(nrowsh,1),b(nrowb,1)
c
c  do 100 j=1,nen
c    j2 = 2*j
c    j2m1 = j2 - 1
c    b(1,j2m1) = shg(1,j)
c    b(1,j2) = 0.0
c    b(2,j2m1) = 0.0
c    b(2,j2) = shg(2,j)
c    b(3,j2m1) = shg(2,j)
c    b(3,j2) = shg(1,j)
c  100 continue
c
c  return
c  end
c-----
c
c  subroutine qdebod (w,det,shg,sl,elresf,work,constm,nen,nint,ned,
c 1      nrowsh,nel)
c
c... program to form body forces
c
c  implicit double precision (a-h,o-z)
c  dimension w(1),det(1),shg(nrowsh,nen,1),elresf(1),sl(1),
c 1      work(1)
c
c... loop over integration points
c
c  do 300 l = 1,nint
c    temp = constm*w(l)*det(l)
c    call multab (shg(1,1,l),sl,work,nrowsh,nen,nrowsh,nen,nrowsh,1,1)
c    work(1) = 0.
c    work(2) = 0.
c    work(3) = 0.
c    do 50 j = 1,nen
c      work(1) = work(1) + shg(1,j,l)*sl(j)
c      work(2) = work(2) + shg(2,j,l)*sl(j)
c      work(3) = work(3) + shg(3,j,l)*sl(j)
c    50 continue
c
c  do 200 j = 1,nen
c    do 100 i = 1,ned
c      ip = ned*(j - 1) + i
c      elresf(ip) = elresf(ip) + temp*work(i)*work(3)*shg(nrowsh,j,l)
c
c  100 continue
c  200 continue
c  300 continue

```

```

200 continue
300 continue
e
  return
end
-----
e
  subroutine qdek(w,det,shg,b,dl,strain,dmat,db,stiff,const,
  l          exp,nen,nint,nesd,nrowsh,nrowb,nstr,nec,nel)
e
e... program to set up the local stiffness matrix
e
e... stiff{nec,nec} local stiffness matrix
e
  implicit double precision (a-h,o-z)
  dimension det(1),w(1),shg(nrowsh,nen,1),b(nrowb,1),dl(1),
  l          dmat(nrowb,1),db(nrowb,1),stiff{nec,1},strain(1)
e
e... loop on integration points
e
  do 100 l=1,nint
    temp = const*w(l)*det(l)
e
e... set up strain rate - velocity matrix 'B'
e
  call qdeb (shg(1,1,1),b,nrowsh,nrowb,nen)
e
e... calculate strain rates at the integration points
e
  call multab (b,dl,strain,nrowb,nec,nstr,nec,nstr,1,1)
e
e... set up the constitutive matrix
e
  call setupd (dmat,strain,temp,nrowb,exp)
e
e... multiply D*B
e
  call multab (dmat,b,db,nrowb,nrowb,nrowb,nstr,nstr,nec,1)
e
e... multiply B(T)*DB, taking account of symmetry and put in stiff
e
  call htdb (stiff,b,db,nec,nrowb,nstr)
100 continue
e
  return
end
-----
e
  subroutine qdekd (w,det,shg,b,gl,strain,dmat,stress,work,
  l          elresf,dl,db,stiff,const,exp,
  l          nen,nint,nrowsh,nesd,nrowb,nec,nstr)
e
e... program to form internal force (-K*D)
e
  implicit double precision (a-h,o-z)
  dimension w(1),det(1),shg(nrowsh,nen,1),b(nrowb,1),gl(1),
  l          strain(1),stress(1),work(1),elresf(1),dl(1),
  l          db(nrowb,1),stiff{nec,1)
e
e... loop on integration points
e
  do 100 l=1,nint
    temp = -const*w(l)*det(l)

```

```

c
c... set up strain rate - velocity matrix 'B'
c
c    call qdeb (shg(1,1,1),b,nrowsh,nrowb,nen)
c
c... calculate strain rates at the integration points
c
c    call multab (b,d1,strain,nrowb,nec,nstr,nec,nstr,1,1)
c
c... set up the constitutive matrix
c
c    call setupd (dmat,strain,temp,nrowb,exp)
c
c... multiply D*B
c
c    call multab (dmat,b,db,nrowb,nrowb,nrowb,nstr,nstr,nec,1)
c
c... multiply B(T)*DB, taking account of symmetry and put in stiff
c
c    call btdb (stiff,b,db,nec,nrowb,nstr)
100 continue
c    call multab(stiff,gl,elresf,nec,nec,nec,nec,nec,1,1)
c
c    return
c    end
-----
c
c    subroutine qdersf (ielno,iside,press,shear,nsurf)
c
c... program to read write and store surface force data
c
c    implicit double precision (a-h,o-z)
c    dimension ielno(1),iside(1),press(3,1),shear(3,1)
c
c    do 100 n=1,nsurf
c      if(mod(n,50) .eq. 1) write(9,1000) nsurf
c      read(8,2000) ielno(n),iside(n),press(1,n),press(2,n),press(3,n),
c      1 shear(1,n),shear(2,n),shear(3,n)
c      write(9,3000) ielno(n),iside(n),press(1,n),press(2,n),press(3,n),
c      1 shear(1,n),shear(2,n),shear(3,n)
100 continue
c
c    return
1000 format('1',
1' ELEMENT SURFACE FORCES DATA '//5x,
1' NUMBER OF SURFACE FORCE CARDS .....(NSURF) = ',i5///
15x,' ELEMENT SIDE ',3(' PRESSURE '),
13(' SHEAR ')/
15x,3(' NUMBER '),3(' NODE I NODE J NODE K ')/)
2000 format(2i5,6f10.0)
3000 format(6x,i5,5x,i2,2x,6(1x,e12.4))
c    end
-----
c
c    subroutine qdeshg (xl,det,shl,shg,nint,nen,nel)
c
c... program to calculate global derivatives of shape functions and
c... Jacobian determinants
c
c... xl(j,i) = global coordinates
c... det(i) = Jacobian determinant
c... shg(1,i,1) = global 'x' derivative of shape functions
c... shg(2,i,1) = global 'y' derivative of shape functions

```

```

c shf(3,i,l) = global shape function
c xs(i,l) = jacobian matrix
c nint = number of integration points
e
implicit double precision (a-h,o-z)
dimension shf(3,nen,1),shg(3,nen,1),xs(2,2),det(1),xl(2,1)
c
call move (shg,shl,3*nen*nint)
do 600 l = 1,nint
do 400 j = 1,2
do 300 i = 1,2
xs(i,j) = rowdott(shg(i,1),xl(j,1),3,2,nen)
300 continue
400 continue
c
det(l) = xs(1,1)*xs(2,2) - xs(1,2)*xs(2,1)
c
if (det(l) .le. 0.0) then
write(*,1000) nel
stop
endif
c
do 500 j = 1,2
do 450 i = 1,2
xs(i,j) = xs(i,j)/det(l)
450 continue
500 continue
c
do 550 i = 1,nen
temp = xs(2,2)*shg(1,i,l) - xs(1,2)*shg(2,i,l)
shg(2,i,l) = -xs(2,1)*shg(1,i,l) + xs(1,1)*shg(2,i,l)
shg(1,i,l) = temp
550 continue
600 continue
c
return
1000 format('SHG, NON-POSITIVE DETERMINANT IN ELEMENT NUMBER ',i5)
end
-----
c
subroutine qdeshl (shl,w,nen,nint)
c
c... program to calculate integration - rule weights, shape functions
c... and local derivatives for six-node triangular element
c
c... rs = local element coordinates
c... shl(1,i,l) = local 'xi' derivative of shape function
c... shl(2,i,l) = local 'eta' derivative of shape function
c... shl(3,i,l) = local shape function
c... w(l) = integration - rule weight
c... i = local node number
c... l = integration node number
c... nint = number of integration points ( eq. to 3)
c
implicit double precision (a-h,e-z)
dimension shl(3,nen,1),w(1),ra(4),sa(4)
c
data ra/-.5,.5,.5,-.5/,sa/-.5,-.5,.5,.5/
g = 2./sqrt(3.)
w(1) = 1.
w(2) = 1.
w(3) = 1.
w(4) = 1.

```

```

c
do 200 l = 1, nint
r = g*ra(l)
s = g*sa(l)
c
do 100 i = 1, 3
tempr = .5 + ra(i)*r
temps = .5 + sa(i)*s
shl(1,i,1) = ra(i)*temps
shl(2,i,1) = tempr*sa(i)
shl(3,i,1) = tempr*temps
c
100 continue
tempr = .5 + ra(4)*r
temps = .5 + sa(4)*s
shl(1,3,1) = shl(1,3,1) + ra(4)*temps
shl(2,3,1) = shl(2,3,1) + tempr*sa(4)
shl(3,3,1) = shl(3,3,1) + tempr*temps
c
200 continue
c
return
end
-----
c
subroutine qdcsuf (ielno,ien,x,xl,inside,press,shear,elresf,
1          brhs,lm,nsurf,nen,nsd,nesd,ned,nee)
c
c... program to compute consistant surface loads.
c... three-point guassian quadrature is employed
c
implicit double precision (a-h,o-z)
dimension z(2),work(2),ielno(1),ien(nen,1),x(nsd,1),
1          xl(nsd,1),inside(1),press(3,1),shear(3,1),
1          elresf(ned,1),brhs(1),lm(ned,nen,1)
c
z(1) = -1.0/sqrt(3.0)
z(2) = -z(1)
c
do 300 l=1,nsurf
nel = ielno(l)
call local (ien(1,nel),x,xl,nen,nsd,nesd)
call clear (elresf,nee)
i = inside(l)
k = i + 1
if (k .eq. 5) k = 1
j = i + 4
dx = xl(1,k) - xl(1,i)
dy = xl(2,k) - xl(2,i)
c
do 200 m=1,2
shi = 0.5*z(m)*(z(m) - 1.0)
shk = 0.5*z(m)*(z(m) + 1.0)
shj = 1.0 - z(m)*z(m)
p = (shi*press(1,1) + shk*press(3,1) + shj*press(2,1))
s = (shi*shear(1,1) + shk*shear(3,1) + shj*shear(2,1))
c
work(1) = 0.5*(-p*dy + s*dx)
work(2) = 0.5*( p*dx - s*dy)
c
do 100 n=1,2
elresf(n,i) = elresf(n,i) + shi*work(n)
elresf(n,k) = elresf(n,k) + shk*work(n)

```

```

      elres(i(n,i)) = elres(i(n,i)) + shj*work(n)
100 continue
200 continue
c
      call addrhs (brhs,elres,lm(1,1,nel),nee)
c
300 continue
c
      return
      end
c-----
c
      subroutine qdet1 (shl ,w ,wm ,ar ,ien ,
1          mat ,id ,lm ,idiag ,ielno ,
1          iside ,press ,shear ,
1          ids ,lms ,
1          numel ,numat ,nsurf ,nint ,nrowsh ,
1          nrowb ,nen ,ndof ,ned ,iprtin)
c
c... program to read generate and write data for nine-node element
c
      implicit double precision (a-h,o-z)
      dimension shl(nrowsh,nen,1),w(1),wm(1),ar(1),
1          ien(nen,1),mat(1),id(ndof,1),lm(ned,nen,1),idiag(1),
1          ielno(1),iside(1),press(3,1),shear(3,1),
1          ids(1),lms(nen,1)
c
      write(9,1000) numel,numat,nsurf
      call qdeshl (shl,w,nen,nint)
c
      call prop2d (ar,numat)
c
      call genel (ien,mat,nen,numel,numat)
c
      if (iprtin .eq. 0) call prntel (mat,ien,nen,numel)
c
      call formlm (id,ids,ien,lm,lms,ndof,ned,nen,numel)
c
      call colht (idiag,lm,ned,nen,numel)
c
      if (nsurf .gt. 0) call qdersf (ielno,iside,press,shear,nsurf)
c
      return
1000 format(///' N I N E _ N O D E ',
1' R E C T A N G U L A R   E L E M E N T S',          //5x,
1' N U M B E R   O F   E L E M E N T S   . . . . . (NUMEL) = ',i5//5x,
1' N U M B E R   O F   E L E M E N T   M A T E R I A L   S E T S   . . . (NUMAT) = ',i5//5x,
1' N U M B E R   O F   S U R F A C E   F O R C E   C A R D S   . . . . (NSURF) = ',i5//)
      end
c-----
c
      subroutine qdet2 (eleflm,ien ,x ,xl ,d ,dl ,
1          det ,shl ,shg ,w ,b ,
1          strain,dmat ,db ,alhs ,idiag ,lm ,
1          argand,mat ,tim ,
1          numel ,neesq ,nen ,nsd ,nesd ,nint ,
1          nrowsh,ndof ,ned ,nrowb ,nstr ,nee)
c
c... program to calculate stiffness matrix for the six node triangular
c... element and assemble into global left_hand_side matrix
c
      implicit double precision (a-h,o-z)
      dimension eleflm(nee,1),ien(nen,1),x(nsd,1),xl(nesd,1),

```

```

1      dett(1),shl(nrowsh,nen,1),shg(nrowsh,nen,1),w(1),
1      b(nrowb,1),d(ndof,1),dl(ned,1),strain(1),
1      dmat(nrowb,1),db(nrowb,1),alhs(1),idiag(1),
1      lm(ned,nen,1),argand(1),mat(1),tim(1)
c
exp = tim(8)
do 100 nel = 1,numel
c
call clear (eleffm,neesq)
call local (ien(1,nel),x,xl,nen,nsd,nesd)
call local (ien(1,nel),d,dl,nen,ndof,ned)
c
c... form stiffness matrix
c
call qdeshg (xl,det,shl,shg,nint,nen,nel)
c
m = mat(nel)
const = argand(m)
call qdek (w,det,shg,b,dl,strain,dmat,db,eleffm,const,exp,
1      nen,nint,nesd,nrowsh,nrowb,nstr,nec,nel)
c
c... assemble element stiffness matrix into global stiffness matrix
c
call addlhs (alhs,eleffm,idiag,lm(1,1,nel),nec)
c
100 continue
c
return
end
c
-----
c
subroutine qdet3 (ien ,g ,gl ,elresf,x ,
1      xl ,det ,shl ,shg ,w ,b ,
1      strain,dmat ,stress,work ,brhs ,lm ,
1      ielno ,iside ,press ,shear ,mat ,s ,
1      sl ,argand,dl ,db ,eleffm,d ,
1      tim ,
1      numel ,ned ,nen ,ndof ,nec ,nesd ,
1      nsd ,nint ,nrowsh,nrowb ,nstr ,nsurf )
c
c... program to calculate residual force vector and assemble into
c... r.h.s vector
c
implicit double precision (a-h,o-z)
logical zerod
dimension ien(nen,1),gl(ned,1),elresf(1),x(nsd,1),
1      xl(nesd,1),det(1),shl(nrowsh,nen,1),shg(nrowsh,nen,1),
1      work(1),w(1),b(nrowb,1),strain(1),s(1),sl(1),argand(1),
1      stress(1),brhs(1),lm(ned,nen,1),dmat(nrowb,1),mat(1),
1      ielno(1),iside(1),press(3,1),shear(3,1),g(ndof,1),tim(1),
1      d(ndof,1),dl(ned,1),db(nrowb,1),eleffm(nec,1)
c
exp = tim(8)
do 100 nel= 1,numel
call local (ien(1,nel),g,gl,nen,ndof,ned)
call clear (elresf,nec)
call clear (eleffm,nec*nec)
call local (ien(1,nel),x,xl,nen,nsd,nesd)
call local (ien(1,nel),d,dl,nen,ned,ndof)
call local1 (ien(1,nel),s,sl,nen)
call qdeshg (xl,det,shl,shg,nint,nen,nel)
call ztest (gl,nec,zerod)
c

```

```

c. form internal force
c
  if (.not. zero) then
    m = mat(nel)
    const argand(m)
    call qdckd (w,det,shg,b,gl,strain,dmat,stress,work,elresf,dl,db,
1          elelfm,const,exp,nen,nint,nrowsh,nesd,nrowb,nec,nstr)
    endif
c
c... form body force
c
  call qdebod (w,det,shg,sl,elresf,work,constm,nen,nint,ned,
1          nrowsh,nel)
c
c... assemble to the r.h.s. vector
c
  call addrhs (brhs,elresf,lm(1,1,nel),nec)
100 continue
c
c... form surface force
c
  if (nsurf .gt. 0)
1call qdesuf (ielno,ien,x,xl,side,press,shcar,elresf,brhs,
1          lm,nsurf,nen,nsd,nesd,ned,nec)
c
  return
  end
c-----
c
  subroutine qdet4 (ien ,d ,dl ,shl ,shg ,b ,
1          strain,x ,xl ,time ,det ,
1          numel ,nen ,ndof ,ned ,nrowsh,nrowb ,
1          nec ,nstr ,nsd ,nesd ,nint)
c
c... program to determine the time interval
c
  implicit double precision (a-h,o-z)
  dimension ien(nen,1),d(ndof,1),dl(ned,1),
1          shl(nrowsh,nen,1),shg(nrowsh,nen,1),b(nrowb,1),
1          x(nsd,1),xl(nesd,1),strain(1),time(1),det(1)
  data det/0.075/
c
  st1 = 0.0
  st2 = 0.0
c
c... find the max [abs(du/dx) + abs(dv/dy)] in the grid
c
  do 200 nel = 1,numel
    call local (ien(1,nel),d,dl,nen,ndof,ned)
    call local (ien(1,nel),x,xl,nen,nsd,nesd)
    call qdeshg (xl,det,shl,shg,nint,nen,nel)
c
  do 100 l = 1,nen
c
  call qdeb (shg(1,1,1),b,nrowsh,nrowb,nen)
  call multab (b,dl,strain,nrowb,nec,nstr,nec,nstr,1,1)
  if (abs(strain(1)) .gt. st1) st1 = abs(strain(1))
  if (abs(strain(2)) .gt. st2) st2 = abs(strain(2))
100 continue
c
200 continue
c
  st = st1 + st2

```

```

c
c... criterion for time interval for time step itime
c
time(1) = def:st
if (time(1) .lt. 0.04) time(1) = 0.04
if (time(1) .gt. .4) time(1) = .4
if (time(1) .gt. time(3) - time(2)) time(1) = time(3) - time(2)
write(*,1000) time(1)
c
return
1000 format(/,'time interval ',f7.4,' Ma')
end
-----
c
subroutine qdet5 (eles ,ien ,x ,xl ,d ,
1 dl ,s ,sl ,det ,shl ,shg ,
1 w ,time ,b ,strain,alhss ,
1 lms ,elrhs ,brhss ,eps ,eps1 ,
1 numel ,nen ,nsd ,nesd ,ndof ,ned ,
1 nint ,nrowsh,nrowb ,nec ,nstr )
c
c... program to solve the time dependent equation with lumped mass
c... matrix
c
implicit double precision (a-h,o-z)
dimension eles(1),ien(nen,1),x(nsd,1),work(10),work1(10),
1 xl(nesd,1),d(ndof,1),dl(ned,1),s(1),sl(1),det(1),
1 shl(nrowsh,nen,1),shg(nrowsh,nen,1),w(1),time(1),
1 b(nrowb,1),strain(1),alhss(1),lms(nen,1),
1 elrhs(1),brhss(1),eps(1),eps1(1)
c
do 400 nel = 1,numel
call clear (eles,nen)
call clear (elrhs,nen)
call clear (work,nen)
call clear (work1,nen)
call local (ien(1,nel),x,xl,nen,nsd,nesd)
call local (ien(1,nel),d,d,1,nen,ndof,ned)
call local1 (ien(1,nel),s,sl,nen)
call local1 (ien(1,nel),eps,eps1,nen)
c
c... form the 'N' and 'a' matrices
c
call qdeshg (xl,det,shl,shg,nint,nen,nel)
c
dsum = 0.
totmas = 0.
divv = 0.
c
do 200 l = 1,nint
c
c... calculate divergence of velocity at integration points
c
call qdcb (shg(1,1,1),b,nrowsh,nrowb,nen)
call multab (b,d,1,strain,nrowb,nec,nstr,nec,nstr,1,1)
divv = strain(1) + strain(2)
ss = 0.
do 50 j = 1,nen
ss = ss + shg(3,j,1)*sl(j)
50 continue
c
temp1 = w(1)*dc(3)
totmas = totmas + temp1

```

```

c
  do 100 j = 1, nen
    temp2 = temp1*shg(nrowsh,j,l)**2
    dsum = dsum + temp2
    work(j) = work(j) + temp2
    elrhs(j) = elrhs(j) - temp1*shg(nrowsh,j,l)*divv*ss
  100 continue
  200 continue
c
c... scale diagonal
c
  temp1 = totmas/dsum
c
  do 300 j = 1, nen
    eles(j) = temp1*work(j)
  300 continue
c
c... add the the global mass matrix and r.h.s vector
c
  call adlhss (alhss,eles,lms(1,nel),nen)
  call adrhss (brhss,elrhs,lms(1,nel),nen)
c
  400 continue
c
  return
  end
-----
c
  subroutine quade (itask,npar,mp)
c
c... program to set storage and call tasks for the nine-node element
c
  dimension npar(1),mp(1)
c
  common /bpoint/ nfirst,mlast,mtot,iprec
  common /info / iexec,iprtin,nsd,ndof,numnp,nlvect,nlvecs
  common /spoint/ mpd,mpg,mpx,mps,mpid,mpl,mpdiag,mpngrp,
1      mpalhs,mpbrhs,mptim,mpdpre,mpdigs,
1      mpalss,mpbrss,mpids,mpeps,mpsdot
  common a(1)
c
  mw = 1
  mdet = 2
  mshl = 3
  mshg = 4
  mar = 5
  mien = 6
  mmat = 7
  mlm = 8
  mielno = 9
  miside = 10
  mpress = 11
  mshear = 12
  melefm = 13
  mxl = 14
  mwork = 15
  mb = 16
  midmno = 17
  mdb = 18
  melres = 19
  mdl = 20
  mstrn = 21
  mstrs = 22

```

```

msl      = 23
mgl      = 24
mpwr     = 25
misd     = 26
meles    = 27
mlms     = 28
melrhs   = 29
mwm      = 30
mepsl    = 31
mpstrm   = 32
mpstrs   = 33
c
numel = npar(1)
numat = npar(2)
nsurf = npar(3)
c
c... set element parameters
c
nen = 3
ned = 2
nec = nen*ned
nesd = 2
nrowsh = 3
necsq = nec*nec
nrowb = 3
nstr = 3
nint = 4
c
if (itask .eq. 1) then
c
c... set memory pointers
c... the mp array is started after the npar array
c... beginning at location mpnpar + 16
c
junk      = mpoint('mp      `33      .0      .0      .1)
c
mp(mw      ) = mpoint('w      `nint      .0      .0      .iprec)
mp(mwm     ) = mpoint('wm     `nen      .0      .0      .iprec)
mp(mdet    ) = mpoint('det    `nint      .0      .0      .iprec)
mp(mshl    ) = mpoint('shl    `nrowsh  .nen      .nint      .iprec)
mp(mshg    ) = mpoint('shg    `nrowsh  .nen      .nint      .iprec)
mp(mar     ) = mpoint('argand `numat   .0      .0      .iprec)
mp(mien    ) = mpoint('ien    `nen      .numel   .0      .1)
mp(mmat    ) = mpoint('mat    `numel   .0      .0      .1)
mp(mlm     ) = mpoint('lm     `ned      .nen      .numel   .1)
mp(mlms    ) = mpoint('lms    `nen      .numel   .0      .1)
mp(mielno  ) = mpoint('ielno  `nsurf   .0      .0      .1)
mp(miside  ) = mpoint('iside  `nsurf   .0      .0      .1)
mp(mpress  ) = mpoint('press  `3       .nsurf  .0      .iprec)
mp(mshear  ) = mpoint('shear  `3       .nsurf  .0      .iprec)
c
mp(melefm  ) = mpoint('elefm  `nec      .nec      .0      .iprec)
mp(meles   ) = mpoint('eles   `nen      .0      .0      .iprec)
mp(mx1    ) = mpoint('x1     `nesd    .nen      .0      .iprec)
mp(mwork   ) = mpoint('work   `18      .0      .0      .iprec)
mp(mb      ) = mpoint('b      `nrowb   .nec      .0      .iprec)
mp(mdmat   ) = mpoint('dmat   `nrowb   .nrowb   .0      .iprec)
mp(mdb     ) = mpoint('db     `nrowb   .nec      .0      .iprec)
mp(melres  ) = mpoint('elresf `nec      .0      .0      .iprec)
mp(melrhs  ) = mpoint('elrhs  `nen      .0      .0      .iprec)
mp(mdl     ) = mpoint('dl     `ned      .nen      .0      .iprec)
mp(mstrm   ) = mpoint('strm   `nrowb   .0      .0      .iprec)
mp(mstrs   ) = mpoint('strs   `nrowb   .0      .0      .iprec)

```

```

mp(mpstrn)  mpoint('pstrn' ,nrowb ,0 ,0 ,iprec)
mp(mpstrs)  mpoint('pstrs' ,nrowb ,0 ,0 ,iprec)

mp(msl )   mpoint('sl' ,nen ,0 ,0 ,iprec)
mp(meps)   mpoint('eps' ,nen ,0 ,0 ,iprec)
mp(mgl )   mpoint('gl' ,ned ,nen ,0 ,iprec)
mp(mplr )   mpoint('plr' ,nen ,0 ,0 ,iprec)
mp(misd )   mpoint('isd' ,numel ,0 ,0 ,1)

c
endif
c
c... task calls
c
if (itask .gt. 5) return
go to (100,200,300,400,500),itask
c
100 continue
c
c... input element data ('input___')
c
call qdet1 (a(mp(mshl )),a(mp(mw )),a(mp(mwm )),
1 a(mp(mar )),a(mp(mien )),a(mp(mmat )),
1 a(mp(id )),a(mp(mlm )),a(mp(diag )),
1 a(mp(mielno)),a(mp(miside)),a(mp(mpress)),
1 a(mp(mshear)),
1 a(mp(mids )),a(mp(mlms )),
1 numel ,numat ,nsurf ,nint ,nrowsh,nrowb ,
1 nen ,ndof ,ned ,iptin)
return
c
200 continue
c
c... form element stiffness matrix and assemble into global
c... left hand side matrix ('form_lhs')
c
call qdet2 (a(mp(melefm)),a(mp(mien )),a(mp(x )),
1 a(mp(mx1 )),a(mp(d )),a(mp(mdl )),
1 a(mp(mdet )),a(mp(mshl )),
1 a(mp(mshg )),a(mp(mw )),a(mp(mb )),
1 a(mp(mstrn )),a(mp(mdmat )),a(mp(mdb )),
1 a(mp(alhs )),a(mp(diag )),a(mp(mlm )),
1 a(mp(mar )),a(mp(mmat )),a(mp(tim )),
1 numel ,neesq ,nen ,nsd ,nesd ,nint ,
1 nrowsh,ndof ,ned ,nrowb ,nstr ,nee )
return
c
300 continue
c
c... form element residual force vector and assemble into
c... global right hand side vector
c
call qdet3 (a(mp(mien )),a(mp(g )),a(mp(mgl )),
1 a(mp(melres)),a(mp(x )),a(mp(mx1 )),
1 a(mp(mdet )),a(mp(mshl )),a(mp(mshg )),
1 a(mp(mw )),a(mp(mb )),a(mp(mstrn )),
1 a(mp(mdmat )),a(mp(mstrs )),a(mp(mwork )),
1 a(mp(brhs )),a(mp(mlm )),a(mp(mielno)),
1 a(mp(miside)),a(mp(mpress)),a(mp(mshear)),
1 a(mp(mmat )),a(mp(s )),a(mp(msl )),
1 a(mp(mar )),a(mp(mdl )),a(mp(mdb )),
1 a(mp(melefm)),a(mp(d )),
1 a(mp(tim )),
1 numel ,ned ,nen ,ndof ,nee ,nesd ,

```

```

1      nsd ,nint ,nrowsh,nrowb ,nstr ,nsurf)
      return
c
c... 400 continue
c
c... determine the time interval
c
      call qdet4 (a(mp(mien )),a(mp(d   )),a(mp(mdl  )),
1      a(mp(mshl )),a(mp(mshg )),a(mp(mb   )),
1      a(mp(mstrn )),a(mp(x   )),a(mp(mxl  )),
1      a(mptim  ),a(mp(mdet  )),
1      numel ,nen ,ndof ,ned ,nrowsh,nrowb ,
1      nec ,nstr ,nsd ,nesd ,nint)
      return
c
c... 500 continue
c
c... solve the time dependent equation
c
      call qdet5 (a(mp(meles )),a(mp(mien )),
1      a(mp(x   )),a(mp(mxl  )),a(mp(d   )),
1      a(mp(mdl  )),a(mp(s   )),a(mp(msl  )),
1      a(mp(mdet  )),a(mp(mshl )),a(mp(mshg )),
1      a(mp(mw   )),a(mptim  ),a(mp(mb   )),
1      a(mp(mstrn )),a(mp(alss  )),
1      a(mp(mlms  )),a(mp(melrth)),a(mp(brss  )),
1      a(mpeps  ),a(mp(mepsl )),
1      numel ,nen ,nsd ,nesd ,ndof ,ned ,
1      nint ,nrowsh,nrowb ,nec ,nstr )
c
      return
      end
-----
c
c      function redot(a,b,ma,n)
c
c... program to compute the dot-product of a vector stored row-wise
c... with a vector stored column-wise
c
      implicit double precision (a-h,o-z)
      dimension a(ma,1),b(1)
c
      redot = 0.0
      do 100 i=1,n
      redot = redot + a(1,i)*b(i)
100 continue
c
      return
      end
-----
c
c      subroutine rdtme (time)
c
c... program to read total time
c
      implicit double precision (a-h,o-z)
      dimension time(1)
c
      print*, 'Enter the total time of the problem, (million years)'
      read (*,*) totime
      time(3) = totime*0.4
c
      return

```

```

c
c-----
c
c   function rowdot (a,b,ma,mb,n)
c
c... program to compute the dot product of vectors stored row-wise
c
c   implicit double precision (a-h,o-z)
c   dimension a(ma,1),b(mb,1)
c
c   rowdot = 0.0
c   do 100 i = 1,n
c     rowdot = rowdot + a(1,i)*b(1,i)
c 100 continue
c
c   return
c   end
c-----
c
c   subroutine serror (name,i)
c
c... program to print error message if available storage is exceeded
c
c   dimension name(2)
c
c   call prtde
c   write(9,1000) i,name
c   stop
c
c 1000 format (1x,5('*'),'STORAGE EXCEEDED BY ',i10,
c           1' WORDS IN ATTEMPTING TO STORE ARRAY',2~4)
c   end
c-----
c
c   subroutine setupd (dmat,strain,const,nrowb,exp)
c
c... program to calculate the D matrix
c
c   implicit double precision (a-h,o-z)
c   dimension dmat(nrowb,1),strain(1)
c
c   p = 0.5*(1.0/exp + 1.0)
c   strain(3) = 0.5*strain(3)
c   etha = 2.0*(strain(1)**2 + strain(2)**2 + strain(3)**2 + strain(1)
c           1*strain(2))
c   etha = etha**p
c   etha = etha*const
c
c   dmat(1,1) = 4.0*etha
c   dmat(1,2) = 2.0*etha
c   dmat(1,3) = 0.0
c   dmat(2,1) = 2.0*etha
c   dmat(2,2) = 4.0*etha
c   dmat(2,3) = 0.0
c   dmat(3,1) = 0.0
c   dmat(3,2) = 0.0
c   dmat(3,3) = 1.0*etha
c
c   return
c   end
c-----
c
c   subroutine smult (a,b,c,mb,mc,m,n,iopt)

```

```

c
c... program to perform scalar multiplication of a matrix
c
  implicit double precision (a-h,o-z)
  dimension b(mb,1),c(mc,1)
c
  go to (1000,2000,3000) iopt
c
c... iopt = 1, multiply entire matrix
c
  1000 do 1200 j=1,n
    do 1100 i=1,m
      c(i,j) = a*b(i,j)
    1100 continue
  1200 continue
  return
c
c... iopt = 2, multiply lower triangle and diagonal elements
c
  2000 do 2200 j=1,n
    do 2100 i=j,m
      c(i,j) = a*b(i,j)
    2100 continue
  2200 continue
  return
c
c... iopt = 3, multiply upper triangle and diagonal elements
c
  3000 do 3200 j=1,n
    do 3100 i=1,j
      c(i,j) = a*b(i,j)
    3100 continue
  3200 continue
c
  return
  end
-----
c
c
  subroutine solves (alhss,brhss,eps,neqs)
c
c... program to solve the lumped 's' matrix
c
  implicit double precision (a-h,o-z)
  dimension alhss(1),brhss(1),eps(1)
c
  do 100 i = 1,neqs
    brhss(i) = (1./alhss(i))* brhss(i)
  100 continue
c
  return
  end
-----
c
c
  subroutine statin (neq,neqs)
c
c... program to set memory pointers for data arrays and call associated
c... input routines
c
  common /bpoint/ mfirst,mlast,mtoL,iprec
  common /info / iexec,iprtin,nsd,ndof,numnp,nlvecL,nlvecs
  common /spoint/ mpd,mpg,mpx,mps,mpid,mpf,mpdiag,mpngrp,
  1 mpalhs,mpbrhs,mptim,mpdpre,mpdigs,
  1 mpalss,mpbrss,mpids,mpeps,mpsdot

```



```
c
c... program to determine if any array contains only zero entries
c
  implicit double precision (a-h,o-z)
  dimension a(1)
  logical lzero
c
  lzero = .true.
  do 100 i = 1,n
  if(a(i) .ne. 0.0) then
  lzero = .false.
  return
  endif
100 continue
c
  return
  end
```

References

- Ambraseys, N. N. & Melville, C., 1982. *A History of Persian Earthquakes*, Cambridge University press, 219 pp.
- Arkani-Hamed, J. & Strangway, D. W., 1986. Magnetic susceptibility anomalies of lithosphere beneath eastern Europe and the Middle East, *Geophysics*, **51**, 1711-1723.
- Asudeh, I., 1982. Seismic structure of Iran from surface and body wave data, *Geophys. J. R. astr. Soc.*, **71**, 715-730.
- Basavaiah, N., Ragaram, M., Qureshy, M. N. & Rangzan, K., 1991. Geopotential studies over Iranian plateau, *Memoirs Geological Society of India*, **24**, 81-92.
- Berberian, M., 1976a. Contributions to the seismotectonics of Iran (part 2), *Rep. geol. Surv. Iran*, No. 39.
- Berberian, M., 1976b. Seismotectonic map of Iran, *Geol. Surv. Iran*.
- Berberian, M., 1981. Active faulting and tectonics of Iran, in *Zagros, Hindu Kush, Himalayas Geodynamic Evolution*, eds Gupta, H. K. & Delany, F. M., *Geodyn. Ser. Am. geophys. Un.*, **3**, 33-69.
- Berberian, M., 1983. The southern Caspian: a compressional depression floored by a trapped, modified oceanic crust, *Can. J. Earth Sci.*, **20**, 163-183.
- Berberian, M. & King, G., 1981. Towards a palaeogeography and tectonic evolution of Iran, *Can. J. Earth. Sci.*, **18**, 210-265.
- Bird, P., 1978. Finite element modeling of lithosphere deformation: the Zagros collision orogeny, *Tectonophys.*, **50**, 307-336.
- Bird, P. & Piper, K., 1980. Plane-stress finite-element models of tectonic flow in southern California, *Phys. Earth planet. Inter.*, **21**, 158-175.

- Bird, P., 1989. New finite element techniques for modeling deformation histories of continents with stratified temperature-dependent rheology. *J. geophys. Res.*, **94**, 3967-3990.
- Conrad, G., Montigny, R., Thuizat, R. & Westphal, M., 1981. Tertiary and Quaternary geodynamics of the southern Lut (Iran) as deduced from paleomagnetic, isotopic and structural data. *Tectonophys.*, **75**, T11-T17.
- DeMets, C., Gordon, R. G., Argus, D. F., Stein, S., 1990. Current plate motions. *Geophys. J. Int.*, **101**, 425-478.
- Ekström, G. & England, P., 1989. Seismic strain rates in regions of distributed continental deformation. *J. geophys. Res.*, **94**, 10231-10257.
- England, P. & Houseman, G., 1985. Role of lithospheric strength heterogeneities in the tectonics of Tibet and neighbouring regions. *Nature*, **315**, 297-301.
- England, P. & Houseman, G., 1986. Finite strain calculations of continental deformation 2. Comparison with the India-Asia collision zone. *J. geophys. Res.*, **91**, 3664-3676.
- England, P. & Jackson, J., 1989. Active deformation of the continents. *Ann. Rev. Earth Planet. Sci.*, **17**, 197-226.
- England, P. & McKenzie, D., 1982. A thin viscous sheet model for continental deformation. *Geophys. J. R. astr. Soc.*, **70**, 295-321.
- England, P. & McKenzie, D., 1983. Correction to: a thin viscous sheet model for continental deformation. *Geophys. J. R. astr. Soc.*, **73**, 523-532.
- Falcon, N. L., 1974. Southern Iran: Zagros mountains, in *Mesozoic-Cenozoic orogenic belts*, ed Spencer, A. M., *Geol. Soc. Lond., Spec. Publ.*, **4**, 193-211.
- Farhoudi, G. & Karig, D., 1977. Makran of Iran and Pakistan as an active arc system. *Geology*, **5**, 664-668.
- Geise, P., Makris, J., Akashe, B., Power, P., Letz, H. & Mostaanpour, M., 1983. Seismic crustal studies in southern Iran between the Central Iran and the Zagros belt. *Geodynamic project (Geotraverse) in Iran*. Report No. **51**, 71-89.

- Goetze, C., 1978. The mechanisms of creep in olivine. *Phil. Trans. R. Soc. Lond. A.*, **288**, 99-119.
- Houseman, G. & England, P., 1986. Finite strain calculations of continental deformation 1. Method and general results for convergent zones. *J. geophys. Res.*, **91**, 3651-3663.
- Hughes, T. J.R., 1987. The Finite Element Method, Linear Static and Dynamic Finite Element Analysis. *Printice-Hall, Inc.*, Englewood Cliffs, New Jersey.
- Jackson, J. A. & Fitch, T., 1981. Basement faulting and the focal depths of the larger earthquakes in the Zagros mountains (Iran). *Geophys. J. R. astr. Soc.*, **64**, 561-586.
- Jackson, J., Fitch, T. & McKenzie, D., 1981. Active thrusting and the evolution of the Zagros fold belt. in *Thrust and Nappe Tectonics*, eds McClay, K. & Price, N., *spec. Publ. geol. Soc. London*, **9**, 371-379. Blackwell Scientific Publications, Oxford.
- Jackson, J. & McKenzie, D., 1984. Active tectonics of the Alpine-Himalayan belt between western Turkey and Pakistan. *Geophys. J. R. astr. Soc.*, **77**, 185-264.
- Jackson, J. & McKenzie, D., 1988. The relationship between plate motions and seismic moment tensors, and the rates of active deformation in the Mediterranean and Middle east. *Geophys. J. R. astr. Soc.*, **93**, 45-73.
- Kadinsky-Cade, K., Barazangi, M., Oliver, J. & Isacks, B., 1981. Lateral variations of high-frequency seismic wave propagation at regional distances across the Turkish and Iranian plateaus. *J. geophys. Res.*, **86**, 9377-9396.
- Kadinsky-Cade, K. & Barazangi, M., 1982. Seismotectonics of southern Iran: the Oman line. *Tectonics*, **1**, 389-412.
- LePichon, X. L., 1968. Sea floor spreading and continental drift. *J. geophys. Res.*, **73**, 3661-3697.
- McKenzie, D., 1972. Active tectonics of the Mediterranean region. *Geophys. J. R. astr. Soc.*, **30**, 109-158.
- McKenzie, D. & Jackson, J., 1983. The relationship between strain rates, crustal thickening,

- palaeomagnetism, finite strain and fault movements within a deforming zone, *Earth planet. Sci. Lett.*, **65**, 182-202.
- Mohajer-Ashjai, A., Behzadi, H. & Berberian, M., 1975. Reflections on the rigidity of the Lut block and recent crustal deformation in eastern Iran, *Tectonophys.*, **25**, 281-301.
- Ni, J. & Barazangi, M., 1986. Seismotectonics of the Zagros continental collision zone and a comparison with the Himalayas, *J. geophys. Res.*, **91**, 8205-8218.
- Nowroozi, A. A., 1976. Seismotectonic provinces of Iran, *Bull. seis. Soc. Am.*, **66**, 1249-1276.
- Sengör, A. M. C. & Kidd, W. S. F., 1979. Post-collisional tectonics of the Turkish-Iranian plateau and a comparison with Tibet, *Tectonophys.*, **55**, 361-376.
- Shoja-Taheri, J. and Niazi, M., 1981. Seismicity of the Iranian plateau and bordering regions, *Bull. seis. Soc. Am.*, **71**, 477-489.
- Snyder, D. B. & Barazangi, M., 1986. Deep crustal structure and flexure of the Arabian plate beneath the Zagros collisional mountain belt as inferred from gravity observations, *Tectonics*, **5**, 361-373.
- Stöcklin, J., 1968. Structural history and tectonics of Iran - a review, *Bull. Am. Ass. Petrol. Geol.*, **52**, 1229-1258.
- Stöcklin, J., 1974. Possible ancient continental margins in Iran, in *The Geology of Continental Margins*, 873-887, eds Burk, C. A. & Drake, C. L., Springer-Verlag, New York.
- Takin, M., 1972. Iranian geology and continental drift in the Middle East, *Nature*, **235**, 147-150.
- Tapponnier, P. & Molnar, P., 1976. Slip-line field theory and large-scale continental tectonics, *Nature*, **264**, 319-324.
- Tchalenko, J. S., 1975. Seismicity and structure of the Kopet Dagh (Iran, USSR), *Phil. Trans. R. Soc.*, **278**, 1-25.
- Vilotte, J. P., Daignières, M. & Madariaga, R., 1982. Numerical modeling of intraplate deformation: simple mechanical models of continental collision, *J. geophys. Res.*, **87**,

10709-10728.

- Vilotte, J. P., Daignières, M., Madariaga, R. & Zienkiewicz, O. C., 1984. The role of a heterogeneous inclusion during continental collision, *Phys. Earth planet. Inter.*, **36**, 236-259.
- Vilotte, J. P., Madariaga, R., Daignières, M. & Zienkiewicz, O., 1986. Numerical study of continental collision: influence of buoyancy forces and an initial stiff inclusion, *Geophys. J. R. astr. Soc.*, **84**, 279-310.
- Vita-Finzi, C., 1982. Recent coastal deformation near the Strait of Hormoz, *Proc. R. Soc. A.*, **382**, 441-457.